January 2012

Series-Fed Aperture-Coupled Microstrip Antennas and Arrays

Bojana Zivanovic
University of South Florida, bzivanov@mail.usf.edu

Series-Fed Aperture-Coupled Microstrip Antennas and Arrays

by

Bojana Zivanovic

A dissertation submitted in partial fulfillment
of the requirements for the degree of
Doctor of Philosophy
Department of Electrical Engineering
College of Engineering
University of South Florida

Major Professor: Thomas M. Weller, Ph.D.
Arthur David Snider, Ph.D.
Kenneth Buckle, Ph.D.
Jeff Frolik, Ph.D.
Srinivas Katkoori, Ph.D.

Date of Approval:
November 13, 2012

Keywords: slot-coupled, patch antenna,
phased array, omni-directional, circular polarization

To my dearest pillars in life, my sister Jelena and Zivanovic and Jovanovic families

For your love, strength and wisdom.

ACKNOWLEDGMENTS

I am grateful to be surrounded by the individuals who have and continue to enrich my life both personally and professionally.

I am indebted for the privilege and the opportunity to be guided and advised by Dr. Tom Weller. I am enormously grateful for his outstanding insights and thoughtful advices regarding the work in this dissertation and other topics. His exceptional intellect, deep understanding of the subject matter and the talent to convey his knowledge with enthusiasm are truly inspiring.

I am thankful to my committee members Dr. A. David Snider, Dr. Kenneth Buckle, Dr. Srinivas Katkoori, and Dr. Jeff Frolik. I greatly appreciate recommendations and assistance of Dr. Kenneth Buckle during early days at the University of South Florida. Dr. A. David Snider's guidance during Master studies and his honest advice was instrumental at crucial times. I extremely appreciate a great care taken to review the work in this dissertation by Dr. Jeff Frolik and for an enjoyable collaboration on projects prior to work presented herein. I am thankful to Dr. Katkoori's assistance throughout the process of completing this work.

For his technical expertise and assistance, I am grateful to Mr. Carlos Costas and the financial support of Raytheon Company in St. Petersburg, FL. For continuous assistance and providing components, I would like to thank Modelithics, Inc.

I treasure the friendships with past WAMI members, Suzette Aguilar and Rebeka Davidova. Suzette Aguilar, I hold our enlightening conversations, problem-solving skills,

electromagnetic consultations, laughter, trips very dearly. Rebeka Davidova, thank you for your humility, honesty and true friendship. I most appreciate help from Dr. Sergio Melais and our humor-enriched antenna discussions. My sincerest regards to Scott Skidmore and Ebenezer Odu for their friendships and help in various aspects. I would like to convey my appreciation for the assistance from a great engineer Henrry La Rosa and an electromagnetic expert Ibrahim Nassar. I am in gratitude to Saurabh Gupta and Ahmad Gheetan for their fabrication assistance. Many days in WAMI's ENB 412 were brightened by insightful RF and microwave conversations with Dr. Saravana Natarajan, Dr. Srinath Balachandran, Alberto Rodriguez, Dr. Quenton Bonds, and Yohannes Samuel. I enjoyed counseling sessions and many great discussions shared with Sam Baylis. I would like to express my deepest admiration and gratitude to Dr. Stefan Stefanoski for all that he has thought me and the help he has selflessly provided.

Without your love and support, my family, I would not been able to persevere and reach this point. To my sister Jelena, I am forever grateful to have you in my life. Your kindness, humbleness and wisdom never cease to amaze me. I am in debt to my mother, Mirjana Zivanovic, and my father, Petar Zivanovic, who have shown me incredible strength. Your love and encouragement throughout the travels were my guiding light. My uncle, Zoran and aunt, Desanka, you have expressed your affection and support in so many ways. Finally, my nana, Dusanka and grandfather, Milorad, your will always remain in my dearest childhood memories and I will always remember your life lessons.

TABLE OF CONTENTS

LIST OF TABLES iii

LIST OF FIGURES iv

ABSTRACT x

CHAPTER 1: INTRODUCTION 1
1.1 Motivation 1
1.2 Existing Methods 3
1.3 Series-fed Microstrip Aperture-coupled Antennas and N-element Arrays 7
1.4 Contributions 9
1.5 Dissertation Overview 10

CHAPTER 2: PROPERTIES OF MICROSTRIP APERTURE-COUPLED ANTENNA AND ARRAYS 12
2.1 Introduction 12
2.2 Aperture-coupled Microstrip Patch Antenna 13
2.2.1 Linear Polarization 14
2.2.2 Circular Polarization 22
2.3 N-Element Linear Array Analysis 26
2.4 Omni-directional Array 32
2.5 Conclusion 36

CHAPTER 3: APERTURE-COUPLED MICROSTRIP ANTENNA SUB-ARRAYS 38
3.1 Introduction 38
3.2 Series-Fed Approach and Derivation of Network Representation 39
3.3 Four-Element Aperture-Coupled Antenna Sub-Array 46
3.3.1 Frequency Beam-Stability at Broadside 46
3.3.2 Dual Feed Constraints and Applications 47
3.4 Dual Feed Approach Results 48
3.5 Single-Fed Aperture-Coupled Microstrip Antenna Sub-Array 50
3.5.1 180-degree Equal Power Split Hybrid Rat-Race Coupler Design 51
3.5.2 Four Aperture-Coupled Antenna Sub-Array with a 180-degree Equal Power Split Hybrid Rat-Race Coupler 52
3.5.3 Six-Element Aperture-Coupled Antenna Sub-Array with a 180-degree Equal Power Split Hybrid Rat-Race Coupler 56

3.5.4 Impact of Increasing the Number of Antenna Elements 62
3.6 Conclusion 62

CHAPTER 4: HEXAGONAL CONFIGURATION OF SINGLE-FED FOUR-COUPLED ANTENNA SUB-ARRAYS 63
4.1 Introduction 63
4.2 Omni-Directional Array Pattern Synthesis 64
4.2.1 Omni-Directional Pattern Characteristics 66
4.2.2 The Effect of Using a Different Number of Sub-Arrays 76
4.2.3 Sectoral Radiation 77
4.2.4 Feed Phase-Differential between Individual Sub-Arrays 80
4.2.5 The Array Pattern Analysis 84
4.3 Conclusion 88

CHAPTER 5: CIRCULARLY POLARIZED SINGLE-FED Z-SLOT APERTURE-COUPLED ANTENNA AND ARRAYS 90
5.1 Introduction 90
5.2 Design of the Circularly Polarized Z-Slot Aperture-Coupled Antenna 91
5.3 Four-Element Circularly Polarized Z-Slot Aperture-Coupled Antenna Arrays 100
5.3.1 Meandered 180-degree Equal Power Split Hybrid Rat-Race Coupler Design 100
5.3.2 Four-Element Z-Slot Aperture-Coupled Meandered CP Array. 103
5.3.3 Four-Element Z-Slot Aperture-Coupled CP Array 109
5.3.4 Inductor and Capacitor Circuit Representations for Matching Networks of Four-Element CP Arrays 114
5.4 Conclusion 117

CHAPTER 6: SUMMARY AND RECOMMENDATIONS 118
6.1 Summary 118
6.2 Recommendations 120

REFERENCES 122

APPENDICES 128
Appendix A: Closed-Form Expressions for the Radiation Patterns of a Microstrip Antenna Based on a Two-Slot Model 129
Appendix B: Conditions for Circular Polarization and Single-Fed Circularly Polarized Microstrip Antennas 132
Appendix C: Pattern Parameters for Uniform Amplitude Broadside Arrays 138
Appendix D: Figure Reprint Permissions 140

ABOUT THE AUTHOR ..... END PAGE

LIST OF TABLES

Table 3.1 Single element characteristics. 42

Table 3.2 Matching network for 2-element approach. 45

Table 3.3 Matching networks for 3-element approach. 45

Table 3.4 Dual-fed array characteristics. 49

Table 3.5 Single-fed four-element array characteristics. 53

Table 3.6 Six-element sub-array characteristics. 58

Table 5.1 Single Z-slot aperture-coupled CP antenna characteristics. 94

Table 5.2 Z-slot characteristics. 94

Table 5.3 Z-slot aperture-coupled patch input matching network characteristics. 96

Table 5.4 Rat-Race coupler characteristics. 102

Table 5.5 Four-element meandered CP array characteristics. 104

Table 5.6 Four-element meandered CP array. 104

Table 5.7 Characteristics of the matching network for the meandered four element CP array. 105

Table 5.8 Four-element CP array characteristics. 109

Table 5.9 (a) Characteristics of the antenna element, (b) Characteristics of the Z-slot in the four-element CP array. 110

Table 5.10 Characteristics of the matching network for the four-element CP array. 110

Table 5.11 Characteristics of capacitor and inductor HFSS topologies. 116

Table C.1 Major pattern parameters for uniform linear broadside array. 140

LIST OF FIGURES

Figure 1.1 Overview of the proposed system [71] © [2012] IEEE. 2

Figure 1.2 (a) Biconical horn antenna with flare angles θ_a and θ_b [1] © [1988] IEEE. 4

Figure 1.3 (a) Patch antenna structure (top). 6

Figure 2.1 (a) Aperture-coupled microstrip antenna. 13

Figure 2.2 (a) Cavity model representation of the microstrip patch antenna. 14

Figure 2.3 (a) Cross-section of the E-field, voltage (V), current (I) and impedance (Z) distribution along the length of the aperture-coupled antenna without the effect of the aperture. 16

Figure 2.4 Cross-section of aperture-coupled antenna. 18

Figure 2.5 Circuit representation of the aperture-coupled antenna in [18] © [1991] IEEE. 19

Figure 2.6 Circular-polarized aperture-coupled antenna with coupler in [14] © [1989] IEEE. 23

Figure 2.7 Percent CPBW versus substrate thickness [47] © [1988] IEEE. 25

Figure 2.8 Single-fed circularly polarized aperture-coupled antennas from (a) [49] © [2003] IEEE, (b) [50] © [1996] IEEE, (c) [51] © [1998] IEEE. 26

Figure 2.9 Illustration of pattern multiplication. 28

Figure 2.10 The total radiated far-field resulting from N-element linear array referenced at x,y,z=0. 29

Figure 2.11 (a) Series-fed linearly polarized array topology from [55] © [1992] IEEE. 32

Figure 2.12 (a) Series-fed circularly polarized array architecture from [57] © [2010] IEEE. 32

Figure 2.13 An omni-directional pattern. 33

Figure 2.14 Directivity of an omni-directional antenna with respect to the elevation plane HPBW approximated by (2.20) from [59] © [1993] IEEE. 35

Figure 3.1 Schematic of a single sub-array. 39

Figure 3.2 (a) Single element layout. 41

Figure 3.3 Single element (microstrip antenna) model with open circuit stub appended on the right-hand side. 42

Figure 3.4 Single element Momentum results vs. the equivalent circuit model. 42

Figure 3.5 ADS schematic of two element model (A and B) and three element model (A, B without source termination, and C). 44

Figure 3.6 Impedances (reference Figure 3.5) for 2-element approach (B) and 3-element approach (A) (4.5 to 5.5 GHz). 45

Figure 3.7 Summation of E-fields resulting from two pairs of elements (Pair 1 a and b; Pair 2 a and b) being fed 0° (dotted line) and 180° (solid line) apart. 47

Figure 3.8 Illustration of the four-element dual-fed sub-array. 49

Figure 3.9 Comparison of measured and simulated results of the return loss (dB) of the four-element dual series-fed array. 49

Figure 3.10 Comparison of measured and simulated results of E-plane radiation pattern of the 4 element dual series-fed array. 50

Figure 3.11 Rat-Race coupler used in each single-fed sub-array architecture. 51

Figure 3.12 Simulated results (from Momentum) of the Rat-Race coupler used in each sub-array architecture. 52

Figure 3.13 Illustration of the single-fed four-element sub-array. 53

Figure 3.14 Measured S_{11} for six first generation single-fed sub-arrays....54

Figure 3.15 Comparison of S_{11} between ADS and HFSS simulations with measurement data of six four-element sub-arrays. 55

Figure 3.16 Comparison of the E-field co-pol measurement of the single four-element sub-array across bandwidth and the six four-element sub-arrays that comprise the hexagonal configuration. 56

Figure 3.17 Illustration of the six-element sub-array (dimensions shown are in mm). 58

Figure 3.18 S_{11} (dB) of the six-element array. 59

Figure 3.19 H-plane pattern at 5 GHz (φ-plane). 60

Figure 3.20 E-plane pattern at 5 GHz (θ-plane). 60

Figure 3.21 E-plane pattern over frequency (θ-plane, from 4.5 GHz to 5.5 GHz, 100 MHz increments). 61

Figure 4.1 The effect of adding (turning on) subsequent sub-arrays on azimuth (H-plane) pattern simulated in HFSS. 65

Figure 4.2 Picture of the fabricated hexagonal structure with six four-element sub-arrays. 65

Figure 4.3 S_{11} of the 8-way coupler used to measure omni-directional pattern. 67

Figure 4.4 3-D polar plot of the hexagonal structure simulated in HFSS. 68

Figure 4.5 Azimuth radiation pattern at θ=90 degrees (broadside) for the hexagonal structure. 69

Figure 4.6 Elevation radiation pattern for the hexagonal structure. 70

Figure 4.7 Return loss for different sizes of ground plane for the single sub-array (dimensions are in mm). 71

Figure 4.8 Elevation radiation pattern at φ=0 degrees (broadside) for different sizes of ground plane for a single sub-array. 72

Figure 4.9 Measurement vs. HFSS simulation of azimuth pattern for the hexagonal four-element structure at 5 GHz. 74

Figure 4.10 Gain of the hexagonal structure over frequency. 75

Figure 4.11 Omni-directional pattern (H-plane) for hexagonal structure of four-element sub-arrays over 4.5 GHz to 5.5 GHz frequency range. 76

Figure 4.12 H-plane comparison between square, hexagonal and octagon configuration of four-element sub-arrays simulated at 5 GHz, and measured hexagonal four-element structure at 5 GHz. 77

Figure 4.13 Simulation of azimuth plane comparison between 2, 4, and 6 arrays being used. 79

Figure 4.14 Simulation of azimuth plane comparison between pattern resulting from every second sub-array being used with that of the hexagonal configuration. 80

Figure 4.15 Creation of nulls at specific azimuth angles by using first and fourth sub-array fed with 180 degree out-of-phase signals. 82

Figure 4.16 Comparison of elevation pattern ($\varphi=0^{\circ}$) between hexagonal configuration with sub-arrays being fed by different phase differential at the input in addition to each sub-array being advanced/lagged with respect to the neighboring sub-array (the arrow shown signifies tilting of the elevation pattern resulting from the change in feed phase differential). 83

Figure 4.17 Single dual-fed sub-array with different phase/amplitude of the input signals (the arrow shown signifies tilting of the elevation pattern resulting from the change in feed phase differential). 84

Figure 4.18 Linear array analysis with middle element as the reference element. 86

Figure 4.19 H-plane pattern for 3 sub-arrays for $60^{\circ}< \varphi <120^{\circ}$ given by array analysis for different hexagon widths (a_1 and a_2) and the pattern simulated using HFSS for width a_1. 88

Figure 5.1 (a) Z-slot aperture-coupled microstrip antenna, (b) Cross-section. 91

Figure 5.2 Illustration of the Z-slot aperture-coupling approach. 93

Figure 5.3 Characteristics of (a) the perturbed CP patch microstrip antenna, (b) the coupling Z-slot in the ground. 94

Figure 5.4 Single element Momentum results vs. the equivalent circuit model. 95

Figure 5.5 Single Z-slot aperture-coupled antenna characteristics. 96

Figure 5.6 Simulated (HFSS) versus measured co- and cross-polarized E-plane patterns of the Z-slot aperture-coupled antenna at 5 GHz. 98

Figure 5.7 S_{11} for the single Z-slot aperture-coupled patch antenna. 99

Figure 5.8 Axial ratio over frequency for single patch Z-slot aperture-coupled antenna. 100

Figure 5.9 Rat-Race coupler in four-element CP sub-arrays. 102

Figure 5.10 Simulated results (Momentum) of the meandered Rat-Race coupler used in four-element CP arrays. 103

Figure 5.11 Illustration of the four-element CP array. 104

Figure 5.12 Meandered matching network in each half of the four-element CP array. 105

Figure 5.13 Axial ratio over frequency for the four-element CP Z-slot aperture-coupled array. 106

Figure 5.14 S_{11} of the four-element Z-slot aperture-coupled CP array. 107

Figure 5.15 Comparison of E-plane patterns at $\varphi=90^{\circ}$ and $\varphi=0^{\circ}$ for the four-element Z-slot aperture-coupled CP array. 108

Figure 5.16 Simulated (HFSS) LHCP polarization ratio of the meandered four-element CP array. 108

Figure 5.17 Illustration of the four-element CP array. 109

Figure 5.18 Matching network in each half of the four-element CP array. 110

Figure 5.19 Simulated axial ratio over frequency for the four-element Z-slot aperture-coupled array. 111

Figure 5.20 Simulated S_{11} of the four-element Z-slot aperture-coupled CP array. 112

Figure 5.21 Comparison of the simulated (HFSS) E-plane patterns at $\varphi=90^{\circ}$ and $\varphi=0^{\circ}$ for the four-element Z-slot aperture-coupled CP array. 113

Figure 5.22 Simulated (HFSS) LHCP polarization ratio of the four-element CP array. 113

Figure 5.23 Capacitor (left) and inductor (right) models. 115

Figure 5.24 S_{11} (dB) and S_{12} (degrees) comparison between MDLX, ADS and HFSS models for capacitor. 116

Figure 5.25 S_{11} (dB) and S_{12} (degrees) comparison between MDLX, ADS and HFSS models for inductor. 117

Figure A.1 Magnetic current sheet. 129

Figure B.1 Illustration of the trace of the locus of an electric field for elliptical polarization in time at the particular location. 133

Figure B.2 Feed locations for circularly polarized nearly square microstrip patch antennas [41] © [1979] IEEE. 135

Figure B.3 Illustration of k', k_{10} and k_{01} [47] © [1988] IEEE. 137

Figure B.4 Axial ratio vs. normalized frequency [44] © [1979] IEEE. 137

Figure C.1 Illustration of major and minor lobe, HPBW and FNBW. 138

ABSTRACT

The focus of this dissertation is on the development and circuit modeling of planar series-fed, linear- and circular-polarized microstrip aperture-coupled antennas and N-element arrays operating in C-band. These arrays were designed to be used as part of airborne or land-based frequency-hopped communication systems. One of the main objectives of this work was to maintain a constant beam angle over the frequency band of operation. In order to achieve constant beam pointing versus frequency, an anti-symmetric series-fed approach using lumped-element circuit models was developed. This series feed architecture also balances the power radiated by each element in the N-element arrays.

The proposed series-fed approach was used in the development of four-element series-fed aperture-coupled arrays with 15% 10 dB impedance bandwidth centered at 5 GHz and a gain of 11.5 dB, to construct an omni-directional radiator. Omni-directional radiators with pattern frequency stability are desired in a multitude of applications; from defense in tactical communications, information gathering, and detection of signal of interest to being part of sensors in medical applications. A hexagonal assembly of six series-fed microstrip aperture-coupled four-element arrays was used to achieve the omni-directional radiation with 0.6 dB peak to peak difference across 360˚ broadside pattern and 0.6 dB gain variation at the specific azimuth angle across 15% impedance bandwidth. Given that each of these six arrays can be individually controlled, this configuration allows for individual pattern control and reconfiguration of the omni-directional pattern

with increased gain at specific azimuth angles and the ability to form a directional pattern by employing a fewer number of arrays. Incorporating a beam-forming network or power distribution network is also possible.

Wide 3 dB circular polarization (CP) bandwidth was achieved without external couplers and via only a single feed with a unique Z-slot aperture–coupled microstrip antenna. A single RHCP Z-slot aperture-coupled antenna has ~10% CP and 10 dB impedance bandwidth. The series-fed network consisting of lumped elements, open-circuited stubs and transmission lines was subsequently developed to maintain more than 5% CP and 10% 10 dB impedance bandwidth in the series-fed four-element Z-slot aperture-coupled CP array that could also be used for-omni-directional radiation.

CHAPTER 1:

INTRODUCTION

1.1 Motivation

Advancing the state of antennas for phased array technology is of national and global significance. Antenna systems are key components in most microwave communication systems, and applications for phased arrays range from medical imaging and industrial quality testing to unmanned vehicles and homeland security. Antenna performance requirements for the mentioned uses are very stringent and may call for highly directive designs with wide viewing coverage and the ability to independently control the beams of antennas composing the phased array. The task of designing arrays remains challenging. In particular, there is a need for developing omni-directional antenna techniques with the ability to maintain constant elevation pointing with frequency, and beam segmenting capabilities. In this work, the investigation centers on new omni-directional arrays that are low cost and operate in the C-band.

The intrinsic ability of omni-directional antennas to provide non-directional pattern in azimuth plane and communicate over wide angular ranges makes them suitable for a variety of applications. They are essential to many high data rate communication systems, and specifically, they are extensively used in a variety of defense applications. In tactical communications, they serve in transmitting and receiving between ground-based operators. In information gathering, omni-directional antennas are used to provide

360° monitoring of the environment, and collect the signal information, while the additional ability of the proposed omni-directional radiator to form directional patterns could also be used in determining the direction of a signal of interest. The antennas used in defense applications, apart from being robust and portable, must adapt to harsh environments not only with the ability to adjust the radiation to a desired direction, but also to be able to form more than a single beam in order to receive signal information from different directions at the same time. The type of antenna presented in this work (Figure 1.1) may find use in reconnaissance applications such as airborne or land-based frequency-hopped communications systems that require essentially 2-D coverage (e.g. land-to-land data transfer) but may be prone to tilting of the platform or be subject to jamming signals.

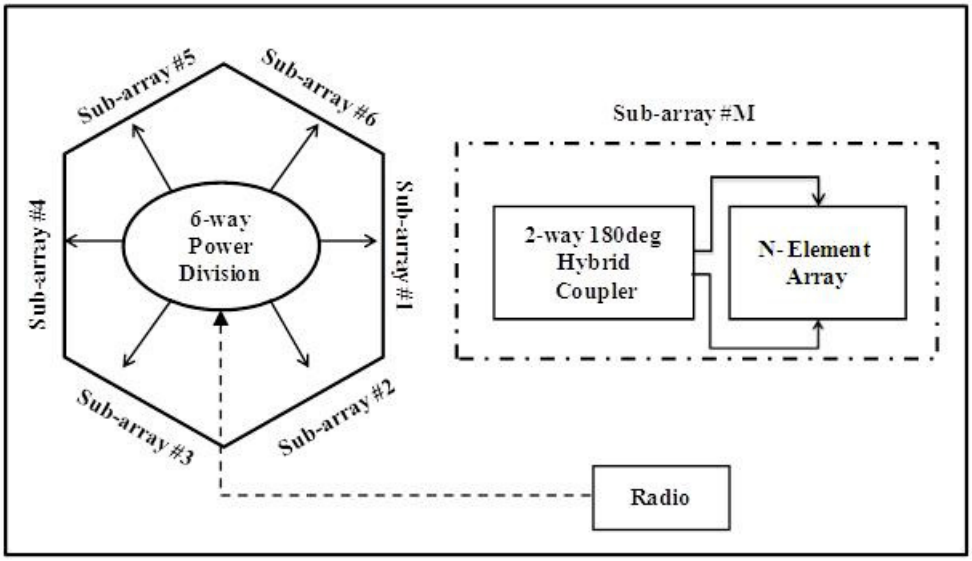

Figure 1.1 Overview of the proposed system [71] © [2012] IEEE.

Multipath interference caused by reflections of the transmitted signal from objects in the environment can severely degrade the performance of a communications link. One reason for this degradation is that the distortion due to multi-path interference can

depolarize signals. For this reason, circularly polarized antennas are advantageous in communication between a circular- and a linear-polarized antenna since they are able to receive arbitrary linear polarizations with minimal signal loss. Thus, since the antennas and the arrays proposed in this work would be part of the systems that operate in a high multi-path and interference environment, the ability of the antenna array system to provide circular polarization is very beneficial. Furthermore, increasing channel capacity is accomplished by the added ability of the proposed antenna system to steer the beam in the desired direction to reduce multi-path or for jamming signals (directing nulls in the desired direction to suppress unwanted radiation). The ability to steer a phased array, and enhance radiation in a desired direction, while minimizing it in another direction if desired, is essential to increasing channel capacity and minimizing interference.

1.2 Existing Methods

Omni-directional radiators found in literature, or commercially available omni-directional antennas, in general, do not provide the capability for beam steering and beam segmenting due to the inherent nature of their designs. Most of these radiators consist of a single element and thus cannot incorporate a network to steer the beam. A single element omni-directional radiator also cannot provide sectoral radiation. Several commercially available designs primarily of the dipole type, vertically polarized antennas that can achieve the required size, bandwidth or power handling specifications, but have an issue in ascertaining beam-pointing versus frequency characteristics, and do not offer capability for beam steering for attitude correction. Planar designs do not in general provide 360^{o} coverage. The biconical horn in [1] is an alternative, and it is formed by joining two cones at their narrower sides (Figure 1.2 (a)). The elevation and azimuth

pattern of the biconical horn could be manipulated by changing the flare angles θ_a and θ_b of each cone. The geodesic slotted cylindrical (GSC) antenna also radiates omni-directionally, but is relatively complicated in design and manufacturing. A GSC antenna is comprised of inner and outer conductive cylinders, where radiation occurs through the slots in the azimuth direction in the outer cylinder (Figure 1.2 (b)) [2]. It is fed by equally spaced probes positioned in the middle of the base of the cylinder. Beam-steering achieved by switching between probes is somewhat impractical for a GSC antenna.

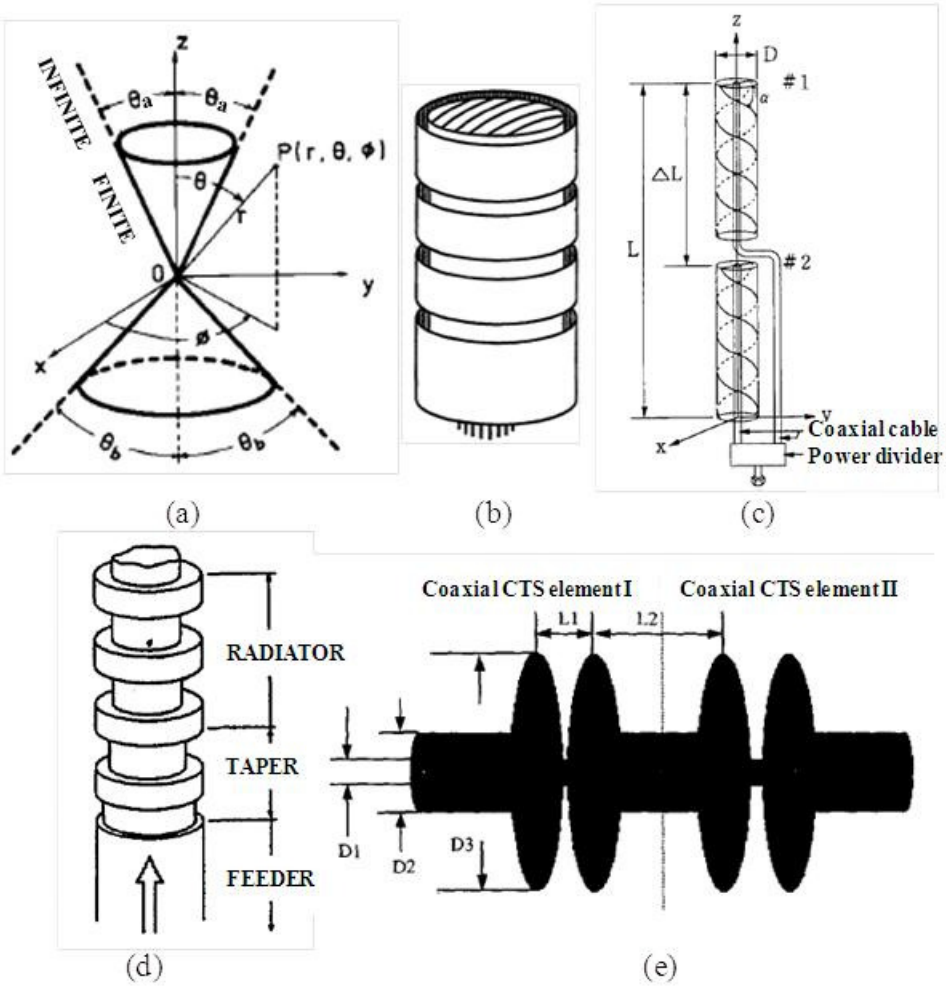

Figure 1.2 (a) Biconical horn antenna with flare angles θ_a and θ_b [1] © [1988] IEEE. (b) GSC antenna [2] © [1999] IEEE. (c) Configuration of a bifilar helical antenna [3] © [1994] IEEE. (d) Dielectric rod antenna with periodic corrugations [4] © [1986] IEEE. (e) Coaxial CTS array [5] © [2001] IEEE.

Other topologies considered for omni directional radiators such as dielectric resonator designs, linear arrays using bifilar helical elements [3], periodic rod antennas [4] and coaxial continuous transverse stub arrays (C-CTS) [5] cannot meet the combined beam steering and frequency stability requirement. Linear arrays using bifilar helical elements consist of two wires wrapped around two cylinders fed by coaxial cables and a power divider (Figure 1.2 (c)). The diameter D and pitch angle alpha determine the direction (angle) at which the antenna is radiating, while the length of the coaxial cables to each cylinder determines the aperture phase difference. Even though the aperture phase difference will reduce pattern drift with frequency, the angle at which the antenna radiates will change with frequency since both D and alpha depend on wavelength. The periodic rod antenna in Figure 1.2 (d) is a high gain antenna composed of periodically corrugated cylindrical waveguide, where perturbations in the cylinder cause the leakage of energy and thus radiation. This rod antenna is difficult to feed, while beam segmenting is not possible due to similar limitations noted for the linear bifilar helical array. The coaxial continuous transverse stub array (Figure 1.2 (e)) is another type of omni directional antenna, where a coaxial transmission line is altered by periodic disk shaped stubs. Even though high gain could be achieved, beam segmenting is not achievable and the manufacturing is rather difficult.

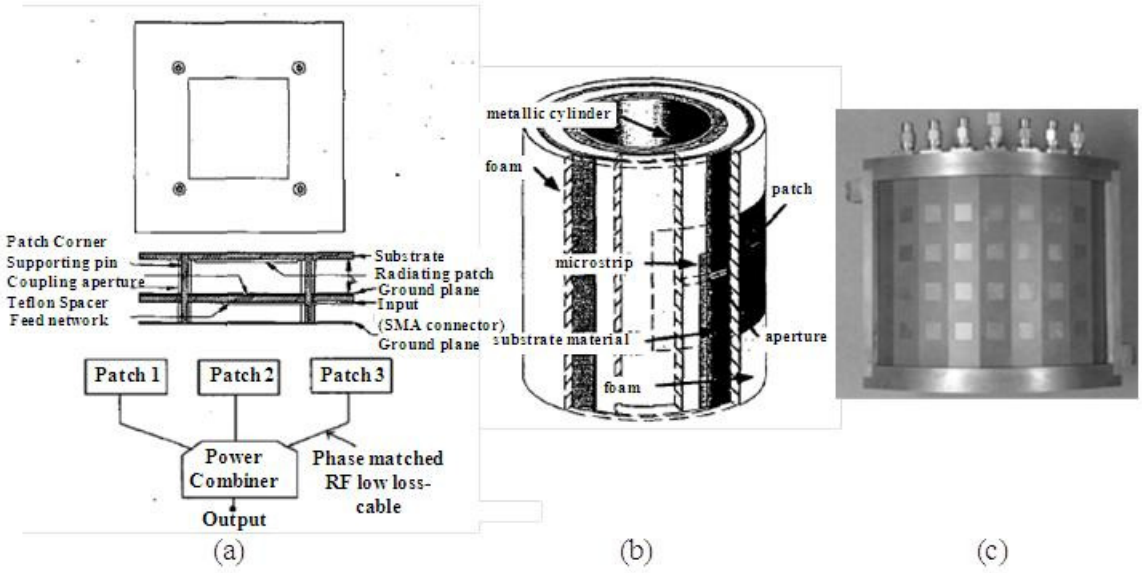

Figure 1.3 (a) Patch antenna structure (top). Three-patch antenna and a power combiner (bottom) [6] © [2003] IEEE. (b) Conformal aperture coupled microstrip array on a cylindrical surface [7] © [1999] IEEE. (c) Faceted configuration of aperture-coupled arrays [8] © [2005] IEEE.

Similar to the proposed design, a patch array on a cylindrical body was reported in [6] and has three wide band aperture-coupled patches placed 120 degrees apart on a cylinder. Each patch faces the cylinder, while its substrate faces the outside of the cylinder. Four Teflon spacers provide the gap between the patch and its substrate, and the ground with an aperture. The configuration is fed by three identical cables, which are further fed by a three-way power combiner (Figure 1.3 (a)). This structure is too simple to provide full beam-steering capabilities, and three patches provide a scalloped radiation pattern. Similar approaches using patches on cylindrical or curved frames were described in [7] and [8]. In the configuration described in [7] and shown in Figure 1.3 (b), the 8 x 2 arrays (8 pairs) of aperture-coupled patches were placed on a metallic cylinder. The metallic cylinder is wrapped with a foam layer that is enclosed by a substrate layer with feed structure on the side closer to the foam layer, and the aperture on the outside surface, followed by another substrate layer with patches facing the outside. This arrangement is

able to achieve the omni-directional pattern, but the number of patch elements placed vertically (in this case 2) provides little pattern control and the manufacturing of the array adds complexity as it is achieved by heating the substrates into a cylinder shape. In [8], seven four-patch sub-array elements were placed on an elliptical surface (Figure 1.3 (c)). However, this configuration does not achieve full omni-directional pattern characteristics.

1.3 Series-fed Microstrip Aperture-coupled Antennas and N-element Arrays

Given the mentioned limited capabilities of other omni-directional radiators, there was a need for an easy to assemble, omni-directional array topology that would circumvent the issue of keeping constant beam-pointing versus frequency found in other approaches. Additionally, the objective was not only for the proposed architecture to provide omni-directional radiation, but also to enable beam-segmenting in instances when omni-directional radiation is not required or when an antenna pattern null is desired for attitude compensation.

The approach taken herein was to construct a cylindrical antenna by combining multiple N-element sub-arrays in a hexagonal arrangement (Figure 1.1). Each N-element sub-array (SA) is comprised of aperture-coupled microstrip antennas that are fed in an anti-parallel, series configuration. This anti-parallel feed ensures a constant broadside beam angle over frequency. In contrast to the alternative omni-directional antenna solutions, the proposed array provides the ability to incorporate a mechanism that would adjust its pattern to enable roll/tilt correction, and at the same time, realize pattern nulls as desired. The proposed feeding mechanism presents an elegant solution for providing beam segmentation capabilities for the phased array, with scalability of its parameters; e.g. , for a forthright method to alter the number of antenna elements, N, in each array.

Multipath interference, among other environmental factors, impedes antenna performance and plays a major role in the strength of the received signal from the antenna. Multipath interference is caused by reflections from objects in space which causes two waves to travel different paths and arrive with different amplitude and phase, thus interfering. It has a depolarizing effect on the signal and a great deal of research has been done [9-10] to investigate channel characteristics, the effects of multi-path and the ways to mitigate it and provide for more reliable connectivity. As multipath interference causes waves to often have arbitrary polarization, it is beneficial to use circular polarization (CP) to reduce its negative effects by giving the antenna the ability to transmit/receive in both vertical and horizontal polarization when attempting to communicate to a linear-polarized antenna and in that way increase the channel capacity.

Unlike the conventional complex antenna feeding mechanisms [11-16] which involve dual feeding to induce CP by exciting two orthogonal modes of equal amplitude, 90 degrees out of phase, each antenna element of the array used in this work is single-fed though a Z-shaped aperture in the ground plane that provides both of the necessary conditions for CP. The CP microstrip Z-slot aperture-coupled antenna array presented here could likewise be used in a hexagonal configuration for omni-directional radiation, and incorporate a beam-forming network.

1.4 Contributions

In summary, the contributions of this dissertation are:

1. Development of a serial feeding approach for N-element uniform aperture-coupled arrays. Implementation of the N-element series-fed approach in four-element aperture-coupled array with 15% 10 dB impedance bandwidth and 11.5 dB of directivity.
2. Design of a linear-polarized omni-directional radiator, with center frequency at 5 GHz and 15% 10 dB impedance bandwidth, able to obtain 6 dB of gain with only 0.6 dB variation in azimuth pattern. The omni-directional radiator achieves beam angle frequency stability with 0.6 dB of variation at a specific azimuth angle across the operational bandwidth, and has the ability to provide sectoral radiation and incorporate beam-forming or power distribution network.
3. Assessment of the azimuth pattern sensitivity to various parameters of the N-element arrays used in composition of the proposed omni-directional hexagonal structure.
4. Development of an approach to obtain wide circular polarization bandwidth without the use of an external coupler in aperture-coupled microstrip antennas centered at 5 GHz. Single RHCP Z-slot aperture-coupled antenna achieves ~10% CP and 10 dB impedance bandwidth.
5. Design of a uniform series-fed circular-polarized Z-slot aperture-coupled microstrip array for integration into circular-polarized omni-directional radiator. The CP bandwidth of up to 5.6% at 5 GHz is demonstrated in the

RHCP four-element Z-slot aperture-coupled CP array architectures with ~19.5 dB LHCP polarization ratio.

1.4 Dissertation Overview

The emphasis of this dissertation lays on the development of a series-feeding methodology for use in the array structures that could be used as standalone radiators or be integrated into an omni-directional radiator. The building block of the research described herein is the aperture-coupled microstrip antenna, both linear and circularly polarized. The architecture, radiation characteristics and advantages of using aperture-coupled antennas and arrays are addressed in more detail in Chapter 2. Further, Chapter 2 gives a theoretical overview of differences in linear and circularly polarized configurations of aperture-coupled antenna, and fundamentals of linear array analysis and its application to aperture-coupled arrays. Basics of linearly and circularly polarized omni-directional arrays are also presented to provide an outline of the work explained in subsequent chapters.

The feeding approach used in arrays described in this research distributes power equally and maintains equal phase at each antenna element in N-element array. The foundation of Chapter 3 is centered on the explanation of the feed network and how it was applied to develop single- and dual-fed four-element aperture-coupled array. The ability of the feeding approach to be easily applied to N-element array was demonstrated through the development of the six-element aperture coupled array.

An omni-directional radiator with stable beam-pointing versus frequency was developed by assembling six four-element aperture-coupled arrays detailed in Chapter 4. Chapter 4 focuses on the operation of the hexagonal structure producing the omni-

directional pattern that varies less than 0.6 dB both in azimuth and across 15% 10 dB impedance bandwidth centered at 5 GHz at a particular azimuth angle. The computational analysis of the omni-directional radiator is greatly simplified through the use of closed-form analysis of the ground plane size and its effect on omni-directional pattern, also presented in Chapter 4. As a non-single element omni-directional antenna, the feasibility of sectoral radiation of the hexagonal structure is demonstrated as well.

Unlike the rectangular slot in the ground used to feed the antenna elements in Chapter 3 and 4, circular polarization in single element and series-fed aperture-coupled arrays is achieved utilizing a Z-shaped aperture. The Z-aperture-coupled antenna element is subsequently used to develop circularly polarized four-element arrays in Chapter 5. Rationalization behind using a Z-slot to induce two equal amplitude orthogonal field components 90 degrees out of phase is provided in Chapter 5. While a Z-slot in the ground is not the only way to induce circular polarization in aperture-coupled antennas, it is a unique approach that minimizes circuit complexity to obtain wide circular polarization bandwidth using only a single feed.

The final chapter (Chapter 6) of this dissertation presents a summary of the work described and suggests a future path for this research.

CHAPTER 2:

PROPERTIES OF MICROSTRIP APERTURE-COUPLED ANTENNA AND ARRAYS

2.1 Introduction

The rationale behind the choice of aperture-coupled microstrip antenna for an antenna element used in the development of series-fed arrays is provided through a theoretical perspective of the advantages of aperture-coupled antennas and arrays. Hence, the architecture of aperture-coupled antennas (Figure 2.1) is explained and its performance characteristics compared with microstrip- and probe-fed microstrip antennas. In particular, some of the topics covered are the choice for antenna and feed substrate, how impedance bandwidth is affected by substrate thickness and its dielectric constant, what parameters influence surface wave radiation, and techniques for obtaining circular polarization for these antennas. The considerations for the preference of serial against corporate feeding in arrays are also examined. Finally, the method in which omni-directional array, both linear and circularly polarized, was developed, is examined through a review of linear arrays and their evolution into omni-directional arrays. The theory provided in this chapter is aimed to show that aperture-coupled antennas incorporated into arrays fed serially via method developed in this work provide significantly better performance in terms of bandwidth and flexibility of its parameters (patch and aperture shape, independent choice of substrates etc.) compared to other microstrip antenna array topologies and can be easily integrated into omni-directional array configurations.

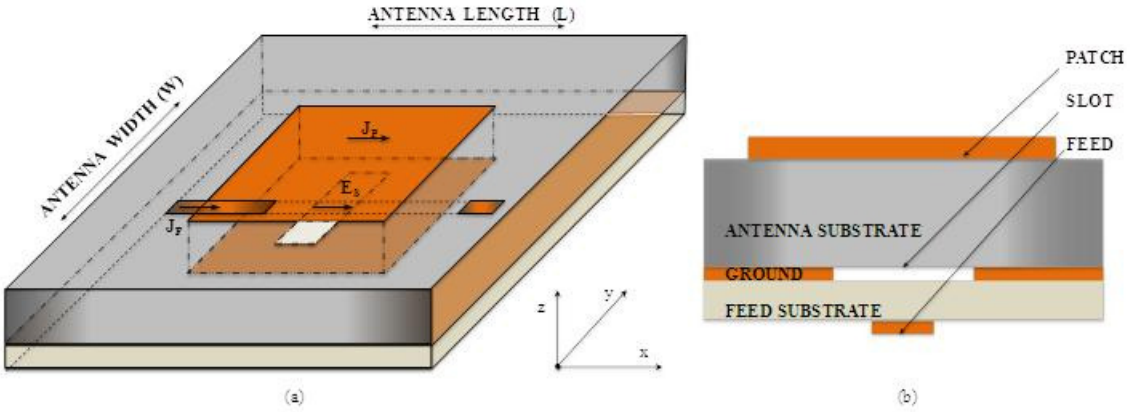

Figure 2.1 (a) Aperture-coupled microstrip antenna. (b) Cross-section.

2.2 Aperture-coupled Microstrip Patch Antenna

The basic structure of the aperture-coupled antenna [17] consists of two different substrate materials on top of each other. The microstrip patch antenna sits on the top of the upper dielectric, while the feed network is placed on the bottom of the lower dielectric (Figure 2.1). The overall antenna element size is minimized by such vertical arrangement of the radiating elements and the feed network. Electromagnetic energy is coupled to the antenna through the aperture in the ground plane, situated in between two substrates. The orientation, the position and particularly the length of the aperture directly influence the amount of energy coupled to the antenna and back radiation, where maximum coupling is achieved if the aperture is centered with respect to the microstrip patch antenna element. Thus, the shape, the size and the position of the antenna element and the aperture can be varied to achieve desired impedance match and directivity. Likewise, two dielectric layers can be independently chosen to optimize both antenna radiation characteristics and feed network loss (this will be further explained in terms of its effect on bandwidth). It should be noted that the aperture coupled feed eliminates the

need for live vias and errors in finding appropriate feed position, both of which affect reliability and limit possible bandwidth that could be achieved.

2.2.1 Linear Polarization

The radiation characteristics of aperture-coupled microstrip antenna are analogous to microstrip- and probe-fed microstrip antenna. Hence, the fundamental principle of operation of microstrip antennas, independent of the way they are fed, is the same. Subsequently, the effect of the aperture-coupled feed is introduced. Various methods of analysis, such as transmission-line model, cavity model and full-wave with integral equations and Method of Moments were used to analyze aperture-coupled microstrip antennas, and similarly aperture-coupled antennas [18-25]. Here, the cavity model is utilized, being more accurate than the transmission-line model and less complex than the full-wave model.

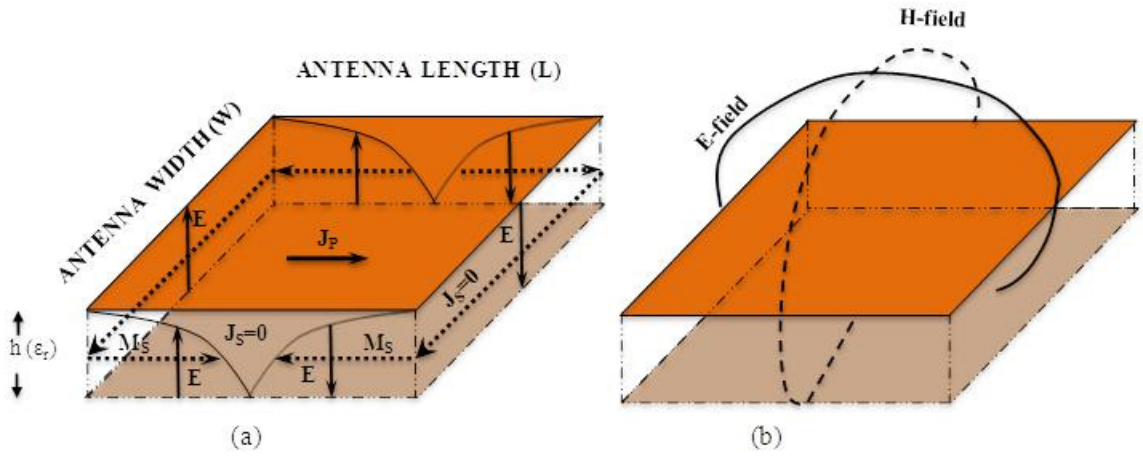

Figure 2.2 (a) Cavity model representation of the microstrip patch antenna. (b) Far E- and H-field patterns.

The aim of the cavity model is to determine the resonant frequency of the microstrip antenna and its E and H far-field patterns. In doing so, a microstrip antenna

can be treated as a lossy dielectric-loaded cavity (Figure 2.2), whose top and bottom walls can be regarded as electric conductors and the four sidewalls are assumed to be magnetic walls signifying open circuit [26]. Sidewalls are responsible for the radiation of the antenna. When to voltage is applied, charge is distributed between the ground plane and the bottom surface of the microstrip antenna. Repulsion of the same polarity charges on the bottom surface of the antenna pushes the charges to the top surface, establishing current densities on both surfaces. Thus, a small current is present on the top surface of the antenna, whose flow from bottom to top surface of the antenna consequently produces a small tangential magnetic field on the edges of the antenna, but it can be neglected as the attractive force between the oppositely charged ground and bottom surface of the antenna is greater for practical height-to-width ratios of the microstrip. Since the thickness of the substrate is much less than the wavelength, the field below the patch is considered constant with respect to height of the substrate. Therefore, only TM^z field configurations are used (field configurations for the rectangular resonant cavity are given in [27]). For the antenna element for which W>L>h, such as the one used in this work, the dominant mode is the TM^z_{001} (Figure 2.3), where its resonant frequency is given by (2.1) [26].

$$(f_r)_{001} = \frac{1}{2W\sqrt{\mu\varepsilon}} = \frac{\upsilon_0}{L\sqrt{\varepsilon_r}} \tag{2.1}$$

where υ_0 is the speed of light in free space., W and L are the width and length, respectively of the antenna element, and ε_r is the dielectric constant of the substrate.

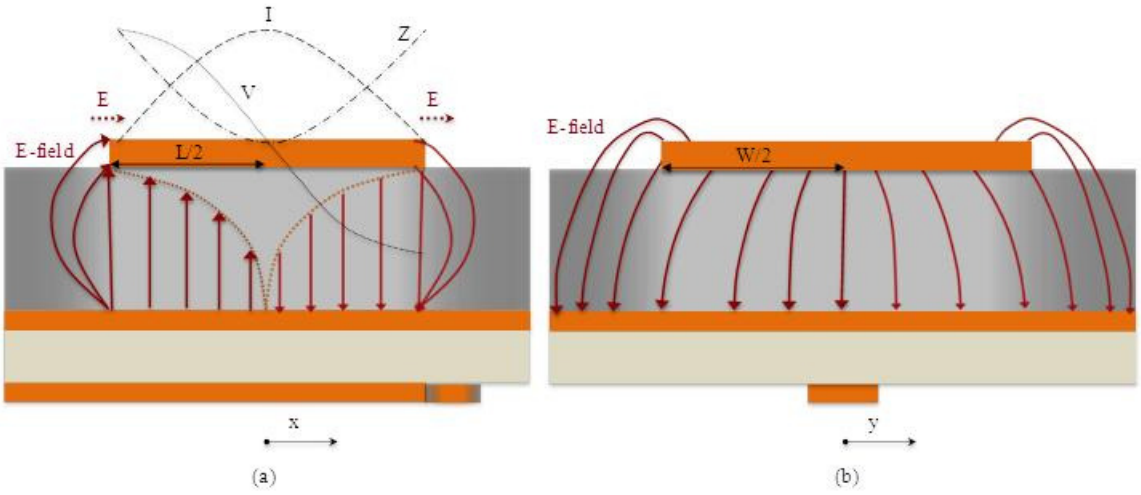

Figure 2.3 (a) Cross-section of the E-field, voltage (V), current (I) and impedance (Z) distribution along the length of the aperture-coupled antenna without the effect of the aperture. (b) E-field along the width of the antenna.

The fields radiated outside the cavity (by the microstrip antenna) are obtained by placing, in this case, a perfect conducting surface on the sidewalls of the cavity and introducing equivalent current densities (of the known components of the field i.e. tangential electric and magnetic field) on the surface of the cavity, which force the fields inside of the cavity to be zero (surface equivalence theorem or Huygens's principle). In such way, based on uniqueness theorem, sources within the cavity along with the description of tangential component of either electric or magnetic field on the surface, uniquely specify the field within the lossy boundary. Thus, as shown in Figure 2.2, the microstrip antenna is represented by equivalent electric current density J_P, while the sidewalls are represented by equivalent electric and magnetic current densities, J_S and M_S respectively. J_S and M_S represent the electric (E) and magnetic (H) fields of the slots. Both J_P and J_S can be neglected as the electric current density on the top surface of the microstrip antenna, for J_P, and tangential field on the edges of the antenna, for J_S, are negligible as noted before. Thus, the cavity can be represented by four magnetic current

densities (M_S) on each sidewall as depicted in Figure 2.2. In order to be able to formulate field expressions, current densities must radiate into unbounded medium, which is not the case when either electric or magnetic boundary exists. Thus, image theory is utilized to remove the presence of the ground, resulting in doubling of the M_S on the sidewalls of the cavity.

The aperture-coupled feed could also be analyzed using Huygens's principle and Bethe hole theory of diffraction by small holes [28]. The aperture in the ground is shorted with a perfect electric conductor and an equivalent magnetic surface current M_{SURF} is placed on its surface (Figure 2.4). Magnetic surface current of the same magnitude, but with opposite direction, is placed on the bottom of the aperture for continuity of the E-field [20]. J_F is an equivalent electric surface current on the feed line. Hence, the aperture in the ground plane is magnetically coupled to the microstrip patch antenna. The amount of coupling is given by (2.2) [29], where x_0 is the aperture offset away from the edge of the antenna. Coupling of the aperture to antenna is mostly affected by the size of the aperture, primarily its length. The cross-section of the alteration of the E-field due to presence of the aperture is also shown in Figure 2.4. The center location of the aperture with respect to the antenna element aids in improving pattern symmetry and polarization purity. The feed line underneath the aperture extends beyond the coupling aperture into an open circuited i.e. tuning stub, and its length is used to adjust the imaginary part of input impedance of the aperture-coupled microstrip antenna.

$$Coupling \approx \iiint_V \overline{M} \cdot \overline{H} dv \approx \sin\left(\frac{\pi x_0}{L}\right) \tag{2.2}$$

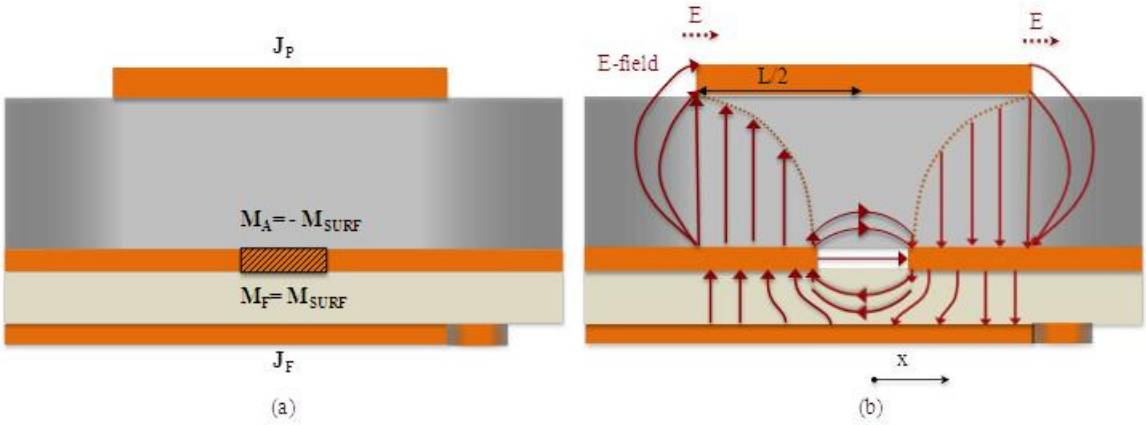

Figure 2.4 Cross-section of aperture-coupled antenna. (a) Magnetic current surface distribution across the aperture. (b) E-field due to aperture-coupling of the antenna.

Two magnetic slots that run along the width of the antenna are responsible for the radiation of the antenna. Since the antenna is assumed to be λ/2 long (as length determines the frequency at which it resonates), and M_S current densities along those walls are of the same amplitude, but 180° out of phase, they cancel each other out. It should be noted that the electrical length of the antenna is greater than λ/2, or it is the effective length L_e in [26] to account for the edge effects where the E-field is not uniform due to fringing fields (the cavity model assumes negligible fringing). Finally, electric (2.3) and magnetic fields (2.4) in [30] can be computed with the use of the array factor for the two-element aperture array (Appendix A), where two sidewalls along the width of the antenna represent each element of the array.

$$E_\theta(\theta,\phi=0) = -j\frac{k_0 W V_0 e^{-jk_0 r}}{2\pi r}\left\{\frac{\sin\left(\frac{k_0 h}{2}\sin\theta\right)}{\frac{k_0 h}{2}\sin\theta}\right\}\cos\left(\frac{k_0 L_e}{2}\sin\theta\right) \qquad (2.3)$$

where $V_0=hE_0$ [26] $$E_\phi(\theta,\phi=90^\circ)=j\frac{k_0WV_0e^{-jk_0r}}{2\pi r}\left\{\frac{\sin\left(\frac{k_0W}{2}\sin\theta\right)}{\frac{k_0W}{2}\sin\theta}\cos\theta\right\} \quad (2.4)$$

Magnetic coupling of the aperture to the antenna in [18] can be represented by a transformer in a circuit representation of aperture-coupled antenna in Figure 2.5, utilizing the explained cavity model for the antenna, aperture magnetic current and dynamic planar waveguide model for the microstrip feed. The input impedance of the aperture-coupled antenna (Y_{IN}) is that of (2.5), and it is expressed in terms of Y_L, Y_e, Y_a, and Y_b, which are the input admittances at the center of the aperture of the microstrip feed, tuning stub, higher order modes in the waveguide model of the feed, aperture-coupled antenna and back radiation, respectively. The resistive part of Y_{IN} at resonance decreases with increasing width of the patch antenna and increases with larger length of the aperture. On the other hand, the length of the tuning stub alters the reactive portion of the input impedance at resonance (tuning stub longer than λ/4 adds inductance as the reactance moves from an open circuit at the end of the stub) [20].

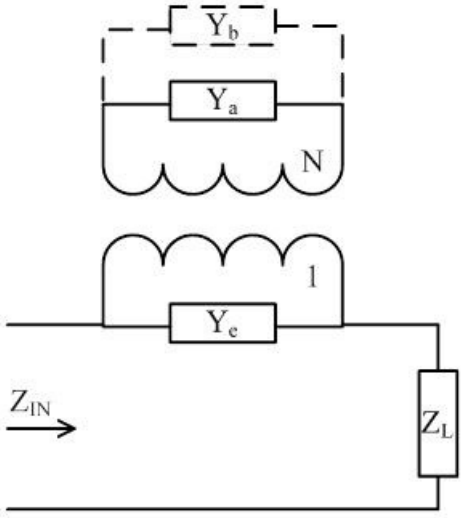

Figure 2.5 Circuit representation of the aperture-coupled antenna in [18] © [1991] IEEE.

$$\frac{1}{Y_{IN}} = \frac{1}{Y_L} + \frac{1}{Y_S}$$
$$Y_S = N^2\left(Y_e + Y_a\right) \tag{2.5}$$
$$Y_{ap} = Y_e + N^2\left(Y_a + Y_b\right)$$

The impedance bandwidth of aperture-coupled antennas can be examined through the prism of parameters that directly influence it: surface waves, substrate thickness and its dielectric constant. Air-dielectric boundaries, such as the one present in aperture-coupled antenna, give rise to and are impinged upon by surface waves. The ground plane beneath dielectric reflects these waves and causes their propagation within the substrate, leading to a decrease in radiation efficiency (2.6) from [31], increase in mutual coupling in arrays of antenna elements and diffraction at the edges of the substrate.

$$\eta = \frac{P_{rad}}{P_{rad} + P_{SW}} \tag{2.6}$$

where P_{rad} is space wave power and P_{sw} is surface wave power.

The surface waves presence cannot be avoided since they propagate unattenuated (propagation constant is real) as the TM_0 mode (which has zero cut-off frequency) of the substrate [32], and their phase velocity (2.7) and cutoff frequencies (2.8) [32] are dependent on substrate parameters, namely its thickness and dielectric constant. In order for only TM_0 mode to be present, the thickness of the single-layer substrate is given by (2.9) (case when n=1 in (2.8) [30]). How surface waves affect different performance parameters of microstrip antennas was studied in more detail in [31, 33-37].

$$v \xrightarrow[h\uparrow]{} k_0\sqrt{\frac{\varepsilon_d \mu_d}{\varepsilon_0 \mu_0} - 1} \tag{2.7}$$

which occurs for large substrate thicknesses. (phase constant of an unattenuated mode propagated by dielectric guide approaches intrinsic phase constant of the dielectric (k_d), k_0 is the intrinsic phase constant of the air).

$$f_r = \frac{nc}{4h\sqrt{\varepsilon_d \mu_d - \varepsilon_0 \mu_0}} \tag{2.8}$$

where f_r is the resonant frequency, and n is 0, 2, 4…for TM_n and 1, 3, 5… for TE_n surface modes, ε_d is dielectric constant of the substrate, h is thickness of the substrate.

$$\frac{h}{\lambda_0} < \frac{1}{4\sqrt{\varepsilon_r - 1}} \tag{2.9}$$

One of the most advantageous aspects of aperture-coupled antennas lies in the facility to place antenna elements and feed network on distinctive substrates. Greater bandwidth and diminished loss or lower total quality factor (more efficient radiation) for the antenna are achieved with the antenna substrates with lower dielectric constant and bigger volume (higher substrate thickness), while higher dielectric constant is more suitable for feed substrate (less spurious radiation). This trend can be readily seen in (2.10) [26] and (2.11) [26]. In (2.11), Q_{rad} is the dominant term for thin substrates (h<0.01λ_0).

$$BW = \frac{VSWR - 1}{Q_{total}\sqrt{VSWR}} \sim \frac{1}{\sqrt{\varepsilon_r}} \tag{2.10}$$

$$\begin{gathered} \frac{1}{Q_{total}} \sim \frac{1}{Q_{rad}} + \frac{1}{Q_{cond}} + \frac{1}{Q_{diel}} + \frac{1}{Q_{SW}} \\ Q_{rad} = \frac{2\omega\varepsilon_r}{hG_t/l}K, \quad Q_{cond} = h\sqrt{\pi f \mu \sigma}, \quad Q_{diel} = \frac{1}{\tan\delta} \end{gathered} \tag{2.11}$$

where $tan\delta$ is the substrate loss tangent, σ is the conductivity of antenna/ground plane conductors, and the total conductance per unit length of the radiation slots is G_t/l [26].

Terms in Q_{total} are related to quality factors representing losses associated with space waves (Q_{rad}), conduction (Q_{cond}), dielectric (Q_{diel}) and surface waves (QSW) respectively. However, thicker substrates also increase surface wave power and in turn increase the quality factor for the antenna, which then reduces bandwidth (as ~$1/Q_{total}$ in (2.10)). In addition, thicker substrates also reduce coupling in aperture-coupled antennas. It is apparent that these parameters factor in the possible microstrip antenna bandwidth that could be attained. In addition to using thick substrates with low dielectric constant to increase the bandwidth of aperture-coupled antennas, dual-fed, various stacked antenna and strip-slot-foam-inverted patch (SSFIP) configurations, among which are the ones in [38-40], were reported in literature. The impedance bandwidth of aperture-coupled antennas up to 20%-50% was achieved.

2.2.2 Circular Polarization

For microstrip antennas, circular polarization is usually attained utilizing a single feed by either proper positioning of the feed, trimming off the diagonal corners of the antenna, or with use of dual feeds, such as the ones in Figure 2.6, to excite two orthogonal modes with quadrature phase difference. The conditions under which the locus of the electric field vector traces a circle in time are given in Appendix B. Circular polarization by dual feeding of square microstrip antennas is accomplished by exciting linearly polarized field of TM^{z}_{010} mode on one edge and linearly polarized field of TM^{z}_{001} mode on the neighboring edge of the antenna (in the perpendicular direction), by placing each feed at the edge location where the field created by the other mode exhibits a null. Quadrature phase difference between these orthogonal modes is then introduced via an external 90° power divider (Figure 2.6). Single-fed induced circular polarization

eliminates external circuitry needed to introduce quadrature phase difference between orthogonal modes, and reduces the overall footprint of the antenna. Herein, a means of single feeding the antenna to obtain circular polarization is of primary interest, and its mode of operation is thus examined more closely [41-48].

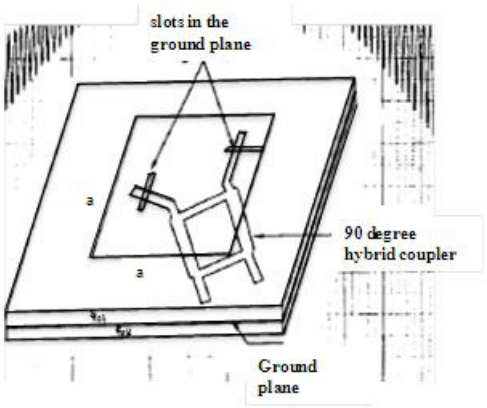

Figure 2.6 Circular-polarized aperture-coupled antenna with coupler in [14] © [1989] IEEE.

Perturbing the microstrip antenna cavity itself, by cutting off diagonal corners of square antenna of length a, is a way to attain circular polarization with a single feed. The mechanism for obtaining circular polarization in such a way can be viewed in light of cavity perturbation theory. In [32], the fractional change in resonant frequency $((\omega-\omega_0)/\omega_0)$ resulting from perturbing the cavity by $\Delta\tau$ (with H_0, E_0 fields inside) is proportional to the ratio of stored electric (ΔW_e) and magnetic (ΔW_m) energies removed by perturbation to the total stored energy (W) before the perturbation (2.12). The resonant frequency of the perturbation is thus changed by perturbing the cavity at the proper location, which is usually the point where electric field is maximum and magnetic field is minimum, or vice versa. The relation between the change in frequency $(k_- - k_+)/ k'$ of the antenna and the amount of trimming the corners of length a-a' (Figure B.2) needed for that particular change in frequency in [41] is determined by (2.13). Perturbation of the antenna caused by trimming its corners along diagonal increases k_- without having a great

impact on k_+. However, (2.13) is only an approximation since perturbation results in disturbance of fringing fields on the edges of antenna, not accounted in (2.13).

$$\frac{\omega-\omega_0}{\omega_0} \approx \frac{\iiint_{\Delta\tau}\left(\mu|H_0|^2-\varepsilon|E_0|^2\right)d\tau}{\iiint_{\tau}\left(\mu|H_0|^2-\varepsilon|E_0|^2\right)d\tau} = \frac{\Delta\overline{W_m}-\Delta\overline{W_e}}{W} \tag{2.12}$$

$$\frac{k_- - k_+}{k'} \approx \frac{2(a-a')}{\pi a}\sin\left[\frac{\pi(a-a')}{a}\right] \tag{2.13}$$

(determination of k' is given in Appendix A).

Wide circular polarization bandwidth, with circular polarization bandwidth (CPBW) defined as CPBW(%)≈36.7h/λ+0.16 (h>0.005 λ) in [47], is much easier to realize with dual-polarized antennas as it usually depends on the impedance bandwidth of the external hybrid used to provide 90° shift between two orthogonal modes. In widening of CPBW, given that CPBW induced by the perturbation on the antenna alone is narrow (Figure 2.7), the topology of aperture-coupled antenna is more advantageous when compared to microstrip- or probe-fed antennas. To increase CPBW, the aperture-coupled feed allows for adjustment of greater number of frequency dependent parameters, for example, aperture shape, its length and width. The dependence of CPBW with respect to substrate thickness (h) in Figure 2.7 suggests that even increasing substrate thickness to 0.09 λ in an attempt to widen the bandwidth, as it was done in this work, would produce CPBW of only ~3.5%.

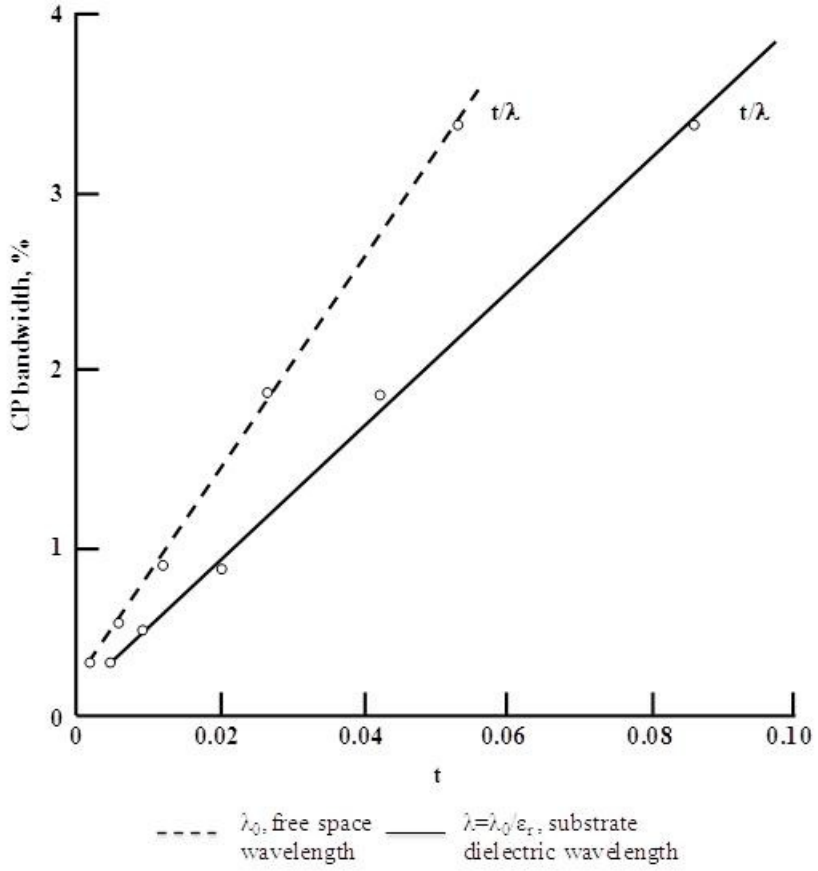

Figure 2.7 Percent CPBW versus substrate thickness [47] © [1988] IEEE.

Coupling of the orthogonal modes in circularly polarized single-fed aperture-coupled antennas [49-51] with a goal of obtaining CP, was done using two or more apertures symmetric about the center of the antenna (Figure 2.8). In the case when two apertures are used to generate CP, each aperture in these works essentially operates at slightly different frequency (determined mostly by its length) providing one of the orthogonal field components (or a combination of, for more than two apertures), while the quadrature phase difference of the currents in each aperture occurs at the frequency in the middle of resonant frequencies of each aperture. Results obtained using these configurations are impedance bandwidth in the range from 10% in [52] to 16.6% in [49]

(Figure 2.8 (a)), and CPBW of 2.2% and 2.5 % in [51] (Figure 2.8 (c)) and [50], respectively, to 4.6% in [49] (Figure 2.8 (b)).

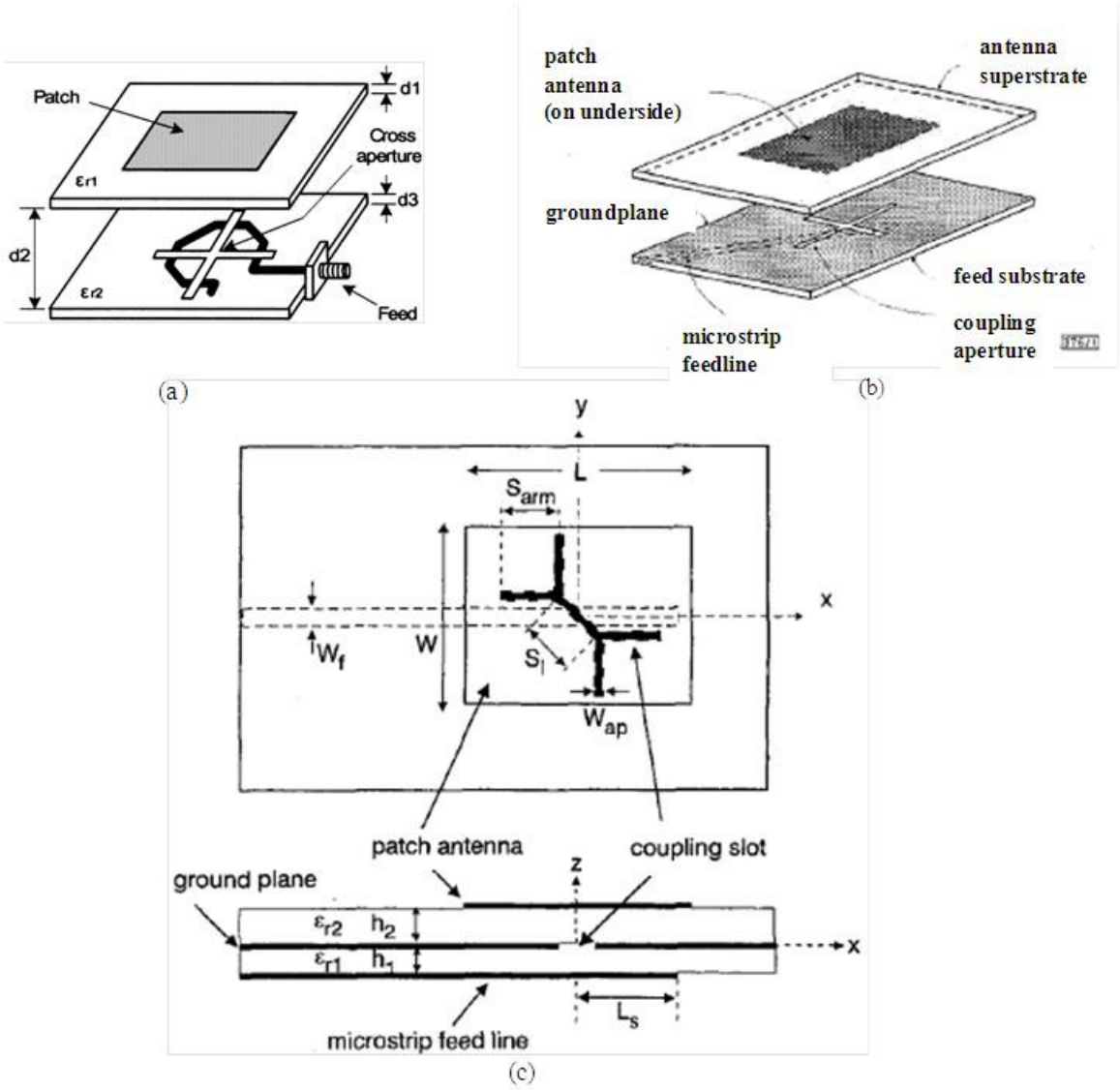

Figure 2.8 Single-fed circularly polarized aperture-coupled antennas from (a) [49] © [2003] IEEE, (b) [50] © [1996] IEEE, (c) [51] © [1998] IEEE.

2.3 N-Element Linear Array Analysis

Omni-directional radiator described in this work employs a hexagonal configuration of six series-fed aperture-coupled microstrip arrays. As such, its radiation characteristics can be examined as an arrangement of six linear arrays. This section thus

offers an overview of linear array analysis theory and array parameters that influence characteristics of importance such as its pattern, directivity, gain and bandwidth.

Rather than increasing the electrical size of a single antenna, an array configuration of equal antenna elements is chosen to increase directivity (thus gain) of a design as its pattern results from pattern multiplication of the field of a single element in the array at the reference position and the corresponding array factor (AF) ($E_{total}=E_1+E_2+...E_n$, for n elements => $E_{total}=[AF][E_{element}]$), Figure 2.9. Pattern multiplication determines the specific locations where maxima and minima (nulls) of the array pattern occur.

Array pattern characteristics depend on geometry of the array, number of antenna elements used, their relative spacing, excitation amplitude and phase, and the antenna element pattern. In choosing the topology for the array, the choice is usually made between the most appropriate amplitude distribution (uniform, Tschebyscheff, binomial etc.) among the elements that results in a given beam-width and side lobe level. Even though both Tschebyscheff and binomial amplitude distributions with non-uniform amplitude distribution among the elements of the array can give lower side-lobe level, uniform distribution with broadside radiation is chosen in this work as it yields the highest directivity and narrowest half-power beamwidth, characteristics generally desirable in, for example, satellite communications.

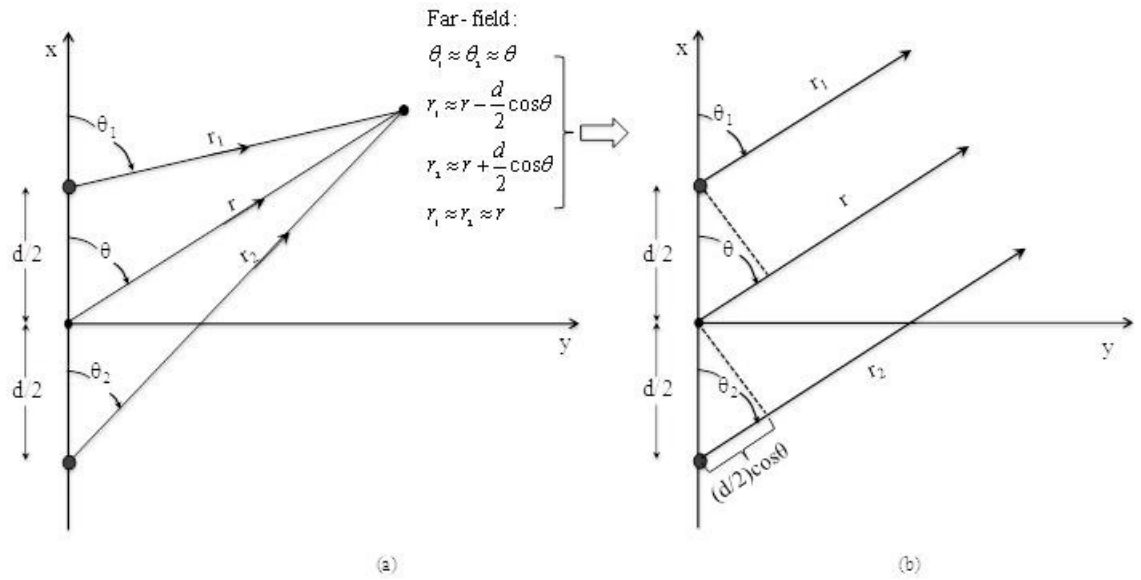

Figure 2.9 Illustration of pattern multiplication. (a)Two-element array with elements equidistant from reference point at x,y,z=0, and their total radiated field. (b)The total radiated far field resulting from two-element array referenced at x,y,z=0 [26].Reprinted with permission from John Wiley & Sons, Inc..

An N-element linear array with uniform amplitude distribution and spacing (d), in Figure 2.10, has elements with equal amplitude, where each subsequent element has progressive phase of ψ (ψ=kdcosθ+β). Its array factor is given by (2.15) and is dependent on ψ, where varying this progressive phase between the elements steers the main beam in a desired direction. The nulls of the array are found by setting AF in (2.15) to zero (sin(Nψ/2)=0) and are dependent on d and β (ψ) . The maxima occurs when ψ=0, and the maximum of the first minor lobe (side lobe) occurs at ~-13.5dB (when Nψ/2≈3π/2).

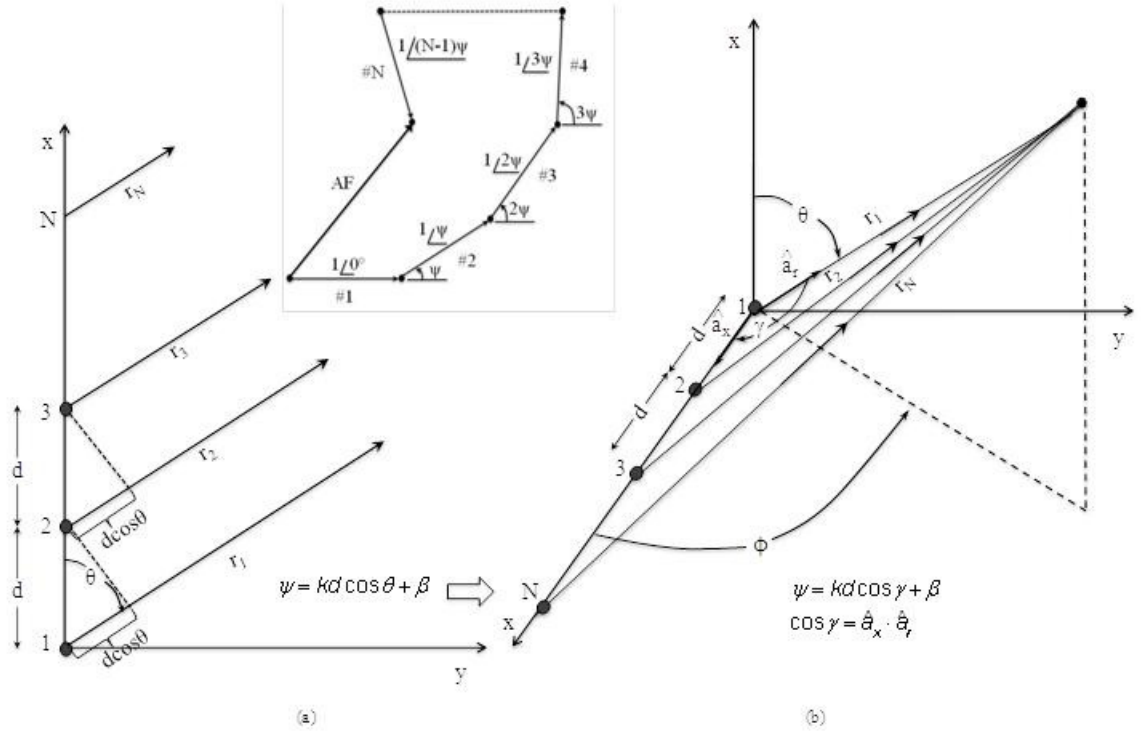

Figure 2.10 The total radiated far-field resulting from N-element linear array referenced at x,y,z=0.(a) N-element linear array with uniform amplitude, spacing and progressive phase ψ, positioned along x-axis.(b) 3-D geometry of the total radiated far-field resulting from N-element linear array positioned along x-axis and referenced at x,y,z=0 [26]. Reprinted with permission from John Wiley & Sons, Inc..

$$AF = 1 + e^{j(kd\cos\theta+\beta)} + e^{j2(kd\cos\theta+\beta)} + \ldots + e^{j(N-1)(kd\cos\theta+\beta)} = \sum_{n=1}^{N} e^{j(n-1)(kd\cos\theta+\beta)} \tag{2.14}$$

or

$$AF = \sum_{n=1}^{N} e^{j(n-1)\psi} \tag{2.15}$$

If both sides of (2.15) are multiplied by $e^{j\psi}$ and that expression subtracted from (2.14), the normalized array factor (AF) referenced at the center of the array can be written as (2.16) [26].

$$(AF)_n = \frac{1}{N}\left[\frac{\sin\left(\frac{N}{2}\psi\right)}{\sin\left(\frac{1}{2}\psi\right)}\right] \tag{2.16}$$

This work sought to devise an array with broadside radiation (perpendicular to the plane of the array). Accordingly, in order for the maxima of the uniform array in Figure 2.10 to be directed perpendicular to the array axis or θ=90°, the elements of the array must be fed in phase (β=0). When phase between the elements is the same and the separation between the elements is greater or equal to λ/2, there will be one null in the pattern due to the array factor. In addition, in order to avoid having any grating lobes (or maxima other than the main lobe), separation between the elements should not be greater λ_0. The conditions and expressions for obtaining nulls, maxima, minima, etc. for broadside array are given in more detail Appendix C. The array factor in (2.15) along with element pattern for the single microstrip antenna element (2.3) can be used to find E_{total} for the uniform broadside array configurations used in this work.

As a consequence of arranging the antenna elements in the array fashion a series of effects on antennas performance must be considered. Some of these are mutual coupling of the antenna elements, scan blindness, the size of the array and its achievable bandwidth, and the choice of feed network. For separation between the elements less than $0.1\lambda_0$, smallest isolation between antenna elements is present when the elements are positioned along the E-field plane. This is due to fields present on the air-dielectric boundary of the antenna, where space waves and higher order modes influence the amount of coupling for small spacing. On the other hand, surface waves contribute the most to coupling of the antenna elements if the distance between them is large [26]. In

addition, the scan blindness poses a problem in scanning of array. The scan blindness effect disturbs side lobe level and polarization purity, and originates also due to occurrence of surface waves, present in both the antenna and feed substrates for aperture-coupled microstrip arrays. Scan blindness causes input impedance mismatch and it transpires when the incident power on the array is trapped in the surface wave modes [53], where its effect is greater in thicker substrates.

Two of the most common feed network arrangements, corporate and series feed, employed in aperture-coupled antennas are shown in Figure 2.11 (linear polarization) and 2.12 (circular polarization, sequentially-fed in Figure 2.12 (b)). The antennas of the array configuration in this work are fed by a unique yet straightforward series feed formation. Series type of feeding offers distinct advantages over corporate feed network in simplicity, volume that it occupies and thus array fabrication cost reduction. It also does not involve external components that introduce significant power loss in the network, such as power dividers, that must be utilized in a corporate feed. The series feed network in broadside arrays does however have a limit on the achievable instantaneous bandwidth that depends on the array length, given as $\Delta f/f=0.886\lambda_0/L$ in [54]. Wide impedance match is harder to attain in uniform broadside linear arrays ($\psi=0$) since power must equally be divided among the elements for uniform current distribution, while keeping the relative progressive phase (ψ) between the elements to zero.

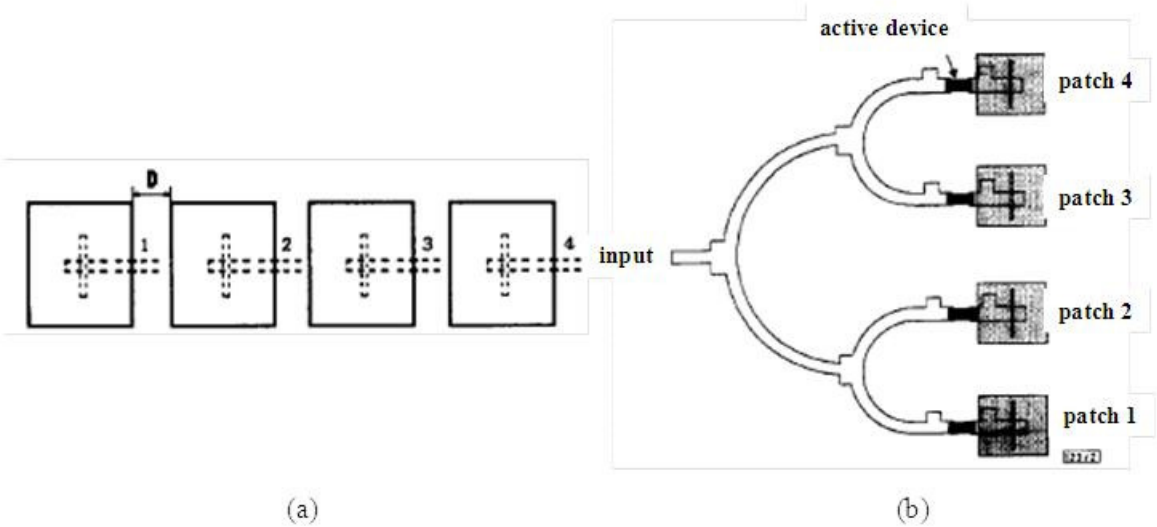

Figure 2.11 (a) Series-fed linearly polarized array topology from [55] © [1992] IEEE. (b) Corporate-fed linearly polarized array topology from [56] © [1995] IEEE.

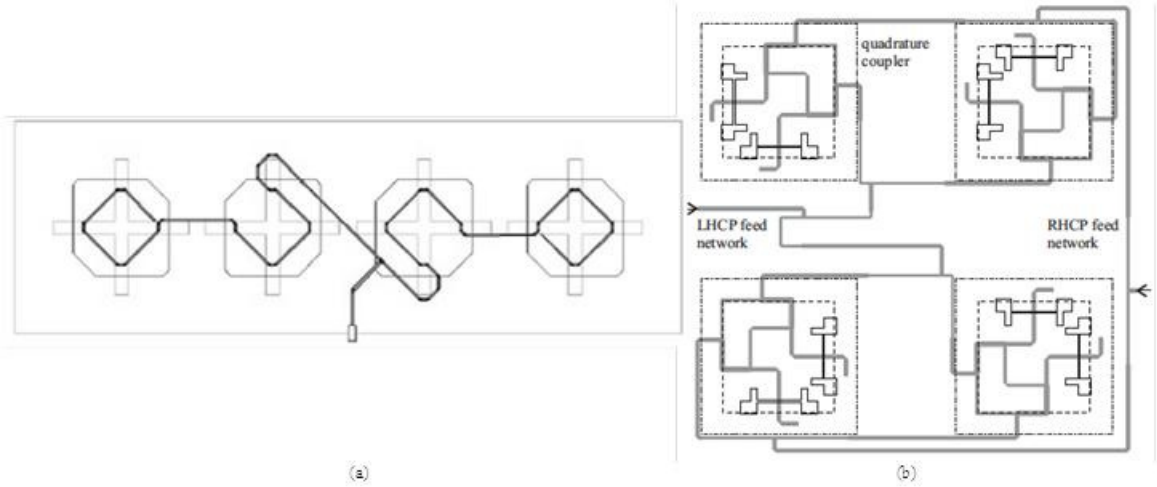

Figure 2.12 (a) Series-fed circularly polarized array architecture from [57] © [2010] IEEE. (b) Corporate sequentially-fed circularly polarized array architecture from [58] © [Year] IEEE.

2.4 Omni-directional Array

An omnidirectional antenna is one that delivers a directional pattern in one plane and a nondirectional pattern in a perpendicular plane (Figure 2.13). In the case of the aperture-coupled antennas in this work, a non-directional pattern is derived using broadside directed patterns of N aperture-coupled arrays. Since radiation intensity, i.e. the

power radiated from an antenna per unit solid angle, can be given as a summation of far-zone electric field of antenna in θ and φ planes (2.17) [26], maximum directivity is given by (2.18) [26]. As such, directivity represents a summation of polarizations in both θ- and φ-plane. Given the definition of directivity in (2.18), the one for an omnidirectional radiator can be approximated by (2.19) [26].

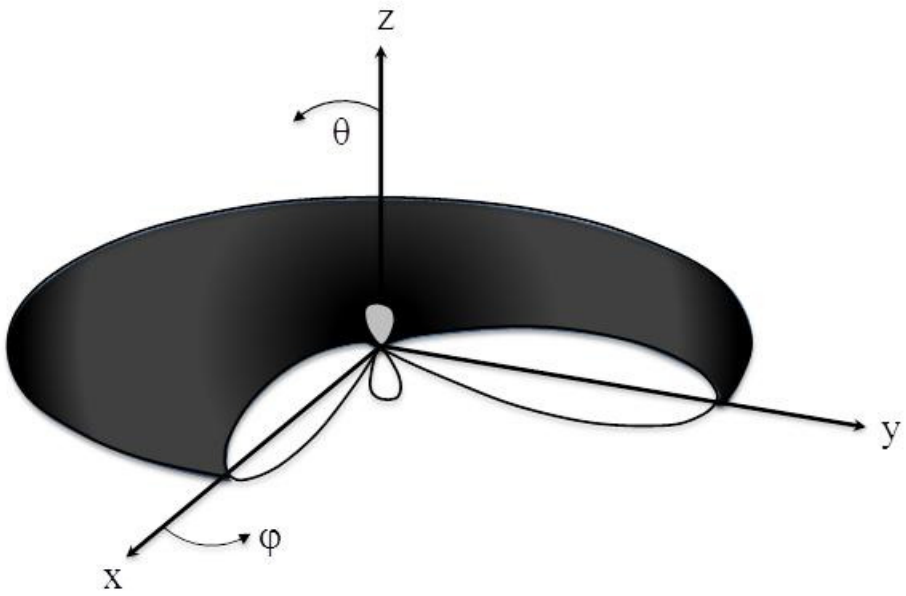

Figure 2.13 An omni-directional pattern.

$$
\begin{aligned}
U(\theta,\varphi) = \frac{r^2}{2\eta}\left|E(r,\theta,\varphi)\right|^2 &\approx \frac{r^2}{2\eta}\left[\left|E_\theta(r,\theta,\varphi)\right|^2 + \left|E_\varphi(r,\theta,\varphi)\right|^2\right] \\
&\approx \frac{1}{2\eta}\left[\left|E_\theta(\theta,\varphi)\right|^2 + \left|E_\varphi(\theta,\varphi)\right|^2\right] \\
&= B_0 F(\theta,\varphi)
\end{aligned}
\tag{2.17}
$$

where B_0 is a constant. If U_0 represents radiation intensity of an isotropic source, and P_{rad} is total radiated power, maximum directivity, D_0, is given by (2.18).

$$D_0 = \frac{U\big|_{\max}}{U_0} = \frac{U_{\max}}{\mathrm{P}_{rad}/4\pi} = 4\pi \frac{B_0 F(\theta,\varphi)\big|_{\max}}{B_0 \int_0^{2\pi}\int_0^{\pi} F(\theta,\varphi)\sin\theta d\theta d\varphi} = 4\pi \frac{F(\theta,\varphi)\big|_{\max}}{\int_0^{2\pi}\int_0^{\pi} F(\theta,\varphi)\sin\theta d\theta d\varphi} \tag{2.18}$$

$$U = \left|\sin^{n}(\theta)\right| \qquad 0 \le \theta \le \pi, \quad 0 \le \varphi \le 2\pi \tag{2.19}$$

For omni-directional antennas whose pattern can be approximated by (2.19), directivity (dB) in terms of half power bandwidth (HPBW) was approximated using curve-fit equation (2.20) in [59]. Directivity with respect to HPBW using this approximation can be seen in Figure 2.14.

$$D_0 = 10\log\left[191.0\sqrt{0.818 + 1/HPBW} - 172.4\right]\mathrm{dB} \tag{2.20}$$

Since omni-directional radiation of this work pertains to an arrangement of broadside N-element arrays, directivity of an omni-directional antenna as given by (2.21) in [60] might be more applicable to this work. The radiation pattern of broadside collinear arrays in [60], was estimated by E(θ)=(sinbθ)/bθ, where b is given in terms of HPBW and is equal to 159/HPBW. Thus, the directivity approximation for moderate to high gain antennas with respect to an isotropic radiator in terms of HPBW was expressed as (2.21) in [60].

$$D_0 = \frac{101}{HPBW - 0.0027[\mathrm{HPBW}]^2} \tag{2.21}$$

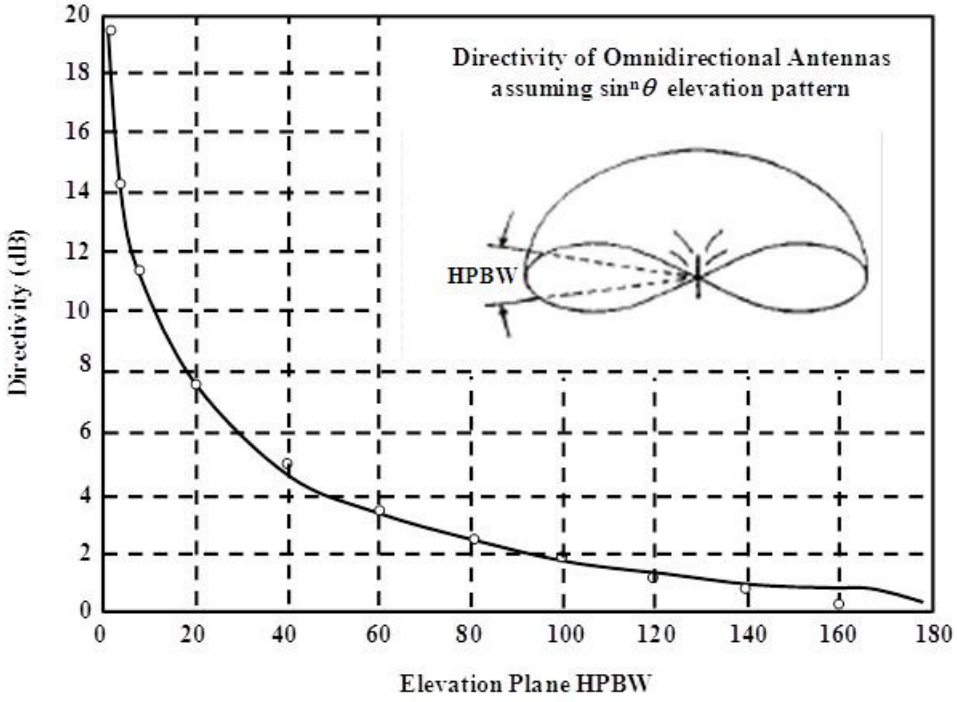

Figure 2.14 Directivity of an omni-directional antenna with respect to the elevation plane HPBW approximated by (2.20) from [59] © [1993] IEEE.

Microstrip arrays with the aim of achieving omni-directional coverage were first wrapped around missiles [61]. These configurations consisted either of a continuous strip of metal or an array of microstrip radiators positioned around the missile circumference. The topologies with a continuous strip of metal need no less than one feed point for each guided wavelength in order achieve omni-directional coverage [62]. Since these wraparound antennas are conformal, unlike the antenna structure of this work, the effect of curvature on these antennas is a significant factor and was thus studied in greater detail for both linearly and circularly polarized architectures [62-66]. The advantage of the omni-directional radiator in this work is that omni-directional coverage is not compromised by using planar arrays and their non-conformity, while the approach for achieving omni-directional coverage could be easily applied if the antenna arrays were

placed on conformal surfaces. Thus, even though the omni-directional antenna in this work is not placed on a cylinder shaped conducting surface, but rather it is an arrangement of planar aperture-coupled microstrip arrays in a hexagonal manner, few conclusions regarding the effect of the number of circumferentially placed radiators (arrays) and their mutual spacing can be noted similarly. The number of arrays utilized to achieve a nearly uniform omni-directional pattern determines the minimum ripple in the gain of an antenna. Correspondingly, there is an optimum circumferential spacing between the arrays (center-to-center antenna spacing) to provide uniform azimuthal coverage. The preferred separation in the elevation plane between antenna elements in an array fed along z-axis, as in the structure presented herein, was found to be $0.85\lambda_0$, while the separation of $0.6\lambda_0$ between elements in azimuth plane produced the greatest directivity in [62]. Similar results were found for circularly-polarized wraparound arrays [61], where the optimum separation between the arrays was found to lie between $0.35\lambda_0$ and $0.7\lambda_0$, and the element spacing less than $0.35\lambda_0$ would degrade axial ratio of the structure due to mutual coupling between the antennas (arrays). In the configuration presented in this work, it was found through simulation that six arrays, spaced approximately $0.5\lambda_0$ along the circumference of the hexagon, is the optimum number needed to produce uniform omni-directional pattern. In addition, the center-to-center inter-element spacing of also $\sim 0.5\lambda_0$ within each array resulted in the greatest directivity for individual arrays.

2.5 Conclusion

Basic theory concepts regarding the operation of aperture-coupled antennas and their patterns were reviewed in this chapter. Methods for achieving circular polarization

for aperture-coupled antennas by means of single-feed were also presented and compared to dual-fed circularly polarized aperture-coupled antennas. The discussion on series-fed aperture-coupled antennas and arrays in this dissertation and their utilization in achieving omni-directional pattern characteristics will be aided by theoretical outline of linear array analysis, their feeding methods and basic characteristics of omni-directional antennas that were also provided in this chapter.

CHAPTER 3:

APERTURE-COUPLED MICROSTRIP ANTENNA SUB-ARRAYS

3.1 Introduction

The advantages of microstrip patch antennas described in the previous chapter are widely known. Their broad use is primarily due to the ease of the fabrication, low cost and simplicity of design. These characteristics, combined with the straight-forward integration with microstrip distribution networks make them especially well suited for phased array applications [67].

In this work, the design of a low cost microstrip patch antenna array (Figure 3.1) suitable for frequency-hopped communications is presented. Two of the main considerations are to achieve (i) an instantaneous bandwidth >10% and (ii) to minimize the elevation beam-angle variation over frequency. A suitable solution to these requirements is an Nx1 microstrip patch array. As shown herein, the use of an aperture-coupled feed along with the proper choice of substrate material provides sufficient bandwidth and also avoids the need for live vias. A series-feed approach, combined with an anti-symmetric dual excitation from both ends of the array, helps to address the elevation beam-pointing specification and reduces the distribution network complexity.

In the following sections the four-element array architecture, six-element design and their feeding networks are described along with simulated and measured return loss and radiation pattern data. An equivalent circuit model for the aperture-coupled patch, which was used to design an inter-element matching network that achieves equal power

distribution to the microstrip patch elements is also presented. All configurations were designed to operate in the C-band. It is shown that the four-element designs operate with approximately 600MHz of bandwidth, with 30 degree elevation beamwidth and a measured gain of ~11dB, and that the gain of six-element array is 12.6dB with ~16% bandwidth.

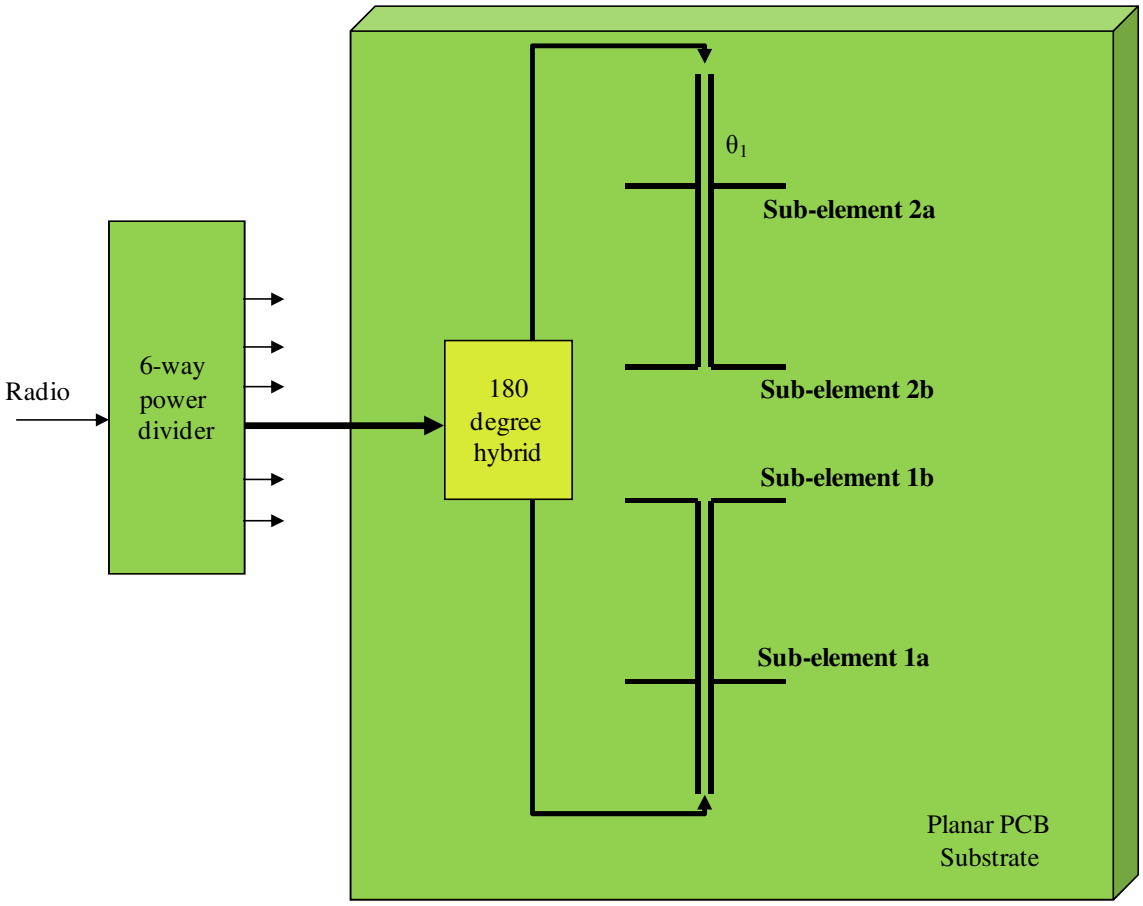

Figure 3.1 Schematic of a single sub-array.

3.2 Series-Fed Approach and Derivation of Network Representation

Each sub-array (SA) is comprised of two pairs of slot-coupled and anti-parallel series-fed elements, depicted in Figure 3.1. The dual series-feeding mechanism employed maintains a broadside pattern over frequency, where opposite ends of the array are fed

with equal but anti-phase signals. The series feeds have been used in order to simplify and reduce the overall footprint. While corporate feed networks are often used in this type of application, they can be comparatively more complex than the series approach because of the power splitters and impedance matching that are required [63, 68].

An illustration of the aperture-coupled microstrip antenna configuration is given in Figure 3.2. The antenna element is located on the upper substrate (Rogers RT/duroid 5880), 3.17 mm thick and with a dielectric constant of 2.2 (h_A, Figure 3.2), and the feed network is located on a lower substrate (Rogers RO4003C), 0.51 mm thick and with a dielectric constant of 3.7 (h_F, Figure 3.2). These substrates were selected due to their suitable dielectric constants.

In what follows an analysis of the series feed used in each sub-array is presented with an emphasis on ensuring proper phasing and equal power distribution to each element. The feeding approach was used in a four-element sub-array, and further investigated for implementation in a six-element sub-array. The characteristics of both six- and four-element sub-array are discussed in subsequent sections of this chapter. An extended analysis of the approach and further characterization of the designs [69-71] is presented.

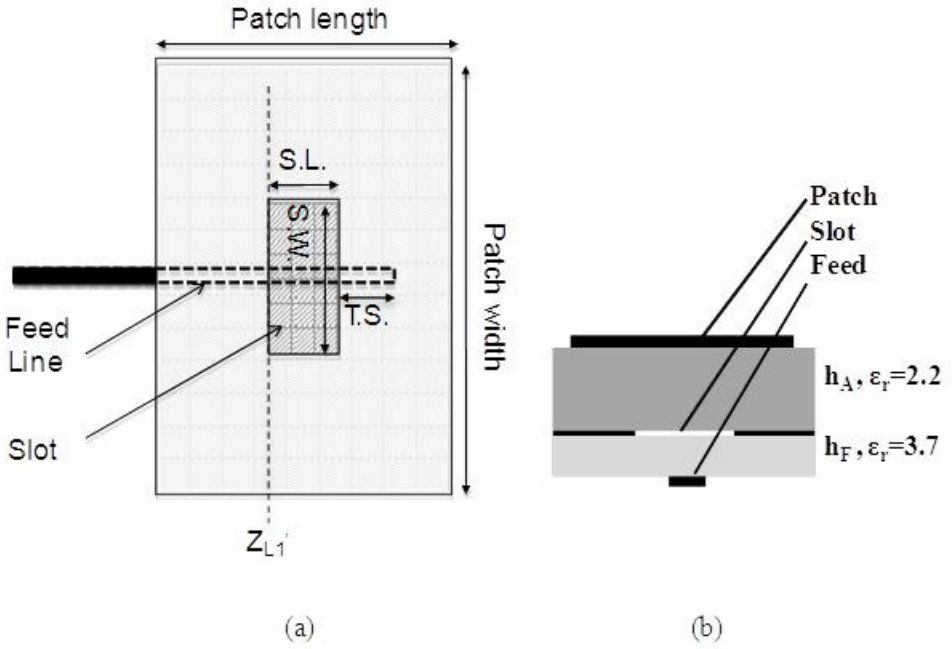

Figure 3.2 (a) Single element layout. (b) Cross-section of the antenna.

The equivalent circuit model for the antenna element is shown in Figure 3.3. A single patch was first designed in Agilent's Momentum with the parameters given in Table 3.1 (a). The results of the electromagnetic (EM) simulation were subsequently used to extract the parameters of the circuit model as shown in Table 3.1 (b). An open circuit stub is appended to the layout in the EM simulation, and represented by a closed-form model in ADS circuit simulations. The patch model is valid over at least the 4 to 6 GHz range (Figure 3.4).

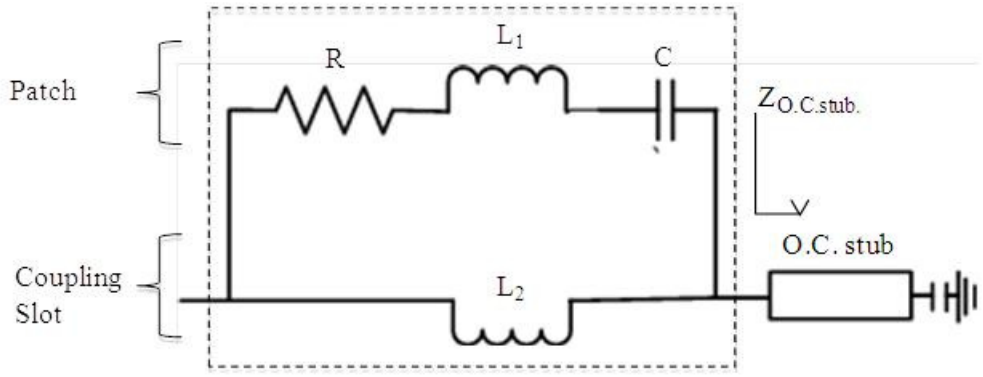

Figure 3.3 Single element (microstrip antenna) model with open circuit stub appended on the right-hand side.

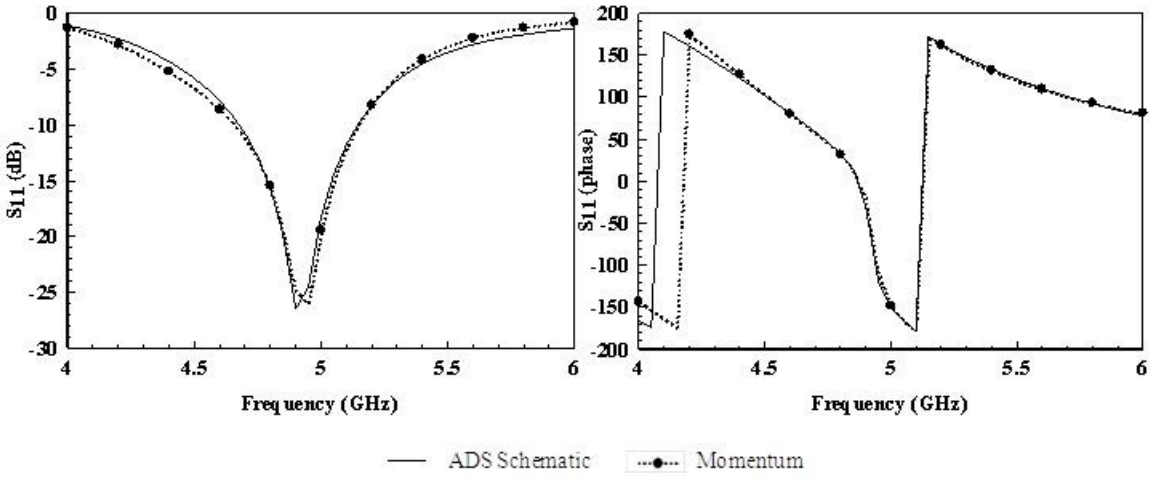

Figure 3.4 Single element Momentum results vs. the equivalent circuit model.

Table 3.1 Single element characteristics.

(a)

Patch Model (ADS Momentum)	Size (mm)
Width	25
Length	17
Slot width (S.W.)	9
Slot length (S.L.)	4
Tuning stub (T.S.)	2.1

(b)

Patch Model (ADS Schematic)	Value
R	287.6 Ω
C	0.013 pF
L1	82.6 nH
L2	4.6 nH
Tuning stub (T.S.)	2.1 mm

To introduce the series-feed approach, equivalent circuit representations for two- and three-element networks are described; hereafter these are referred to as the 2- and 3-

element models. In Chapter 4, the combination of two, anti-symmetrically fed pairs of these models to form sub-arrays of the omni-directional antenna is described. The circuit representation allows efficient determination of the matching circuit topology using circuit optimization techniques.

A representation of the two-element model is shown in Figure 3.5. Here, ZL_1' represents the EM simulation results of a single antenna element (ZL_1) that is terminated by a stub. Between ZL_1' and the second identical antenna element, represented again by ZL1, a matching network is inserted to satisfy the condition $(ZIN_1)^* = ZL_1$, where $(ZIN_1)^*$ is the complex-conjugate of the transformed load impedance presented in series with ZL_1. This condition ensures equal power division between the elements and results in an overall input impedance of $ZL_2 = 2 \cdot Re(ZL_1)$, which has been matched to 50 ohms. The matching network is also designed to ensure that the two elements are fed in phase. The behavior of the complex impedances over frequency is shown in Figure 3.6. The element-to-element spacing is determined by the total length of the microstrip lines, which was kept to less than $\lambda_0/5$ at 5 GHz to maintain low sidelobes.

In order to extend the two-element model to a three-element version, the network must be modified to maintain equal power distribution to each of three antennas. To achieve this, each element was designed to have an impedance of approximately one-third the desired overall input impedance. The impedance of a single element was reduced to the desired level by offsetting the coupling slot beneath the antenna element and by adjusting the width of the feed lines. As before, an equivalent circuit model was extracted from the EM simulation results. The matching networks between the first and second (Figure 3.5, Matching Network #1), and second and third elements (Figure 3.5,

Matching Network #2) provide a conjugate match to the impedance of the single patch model. The impedances at selected points in the three-element model (ZL_1, ZIN_1 and ZIN_2) are shown in Figure 3.6. Dimensions of the matching networks are provided in Table 3.2 (Matching Network #1 for the two-element model) and Table 3.3 (Matching Network #1 and #2 for the three-element model).

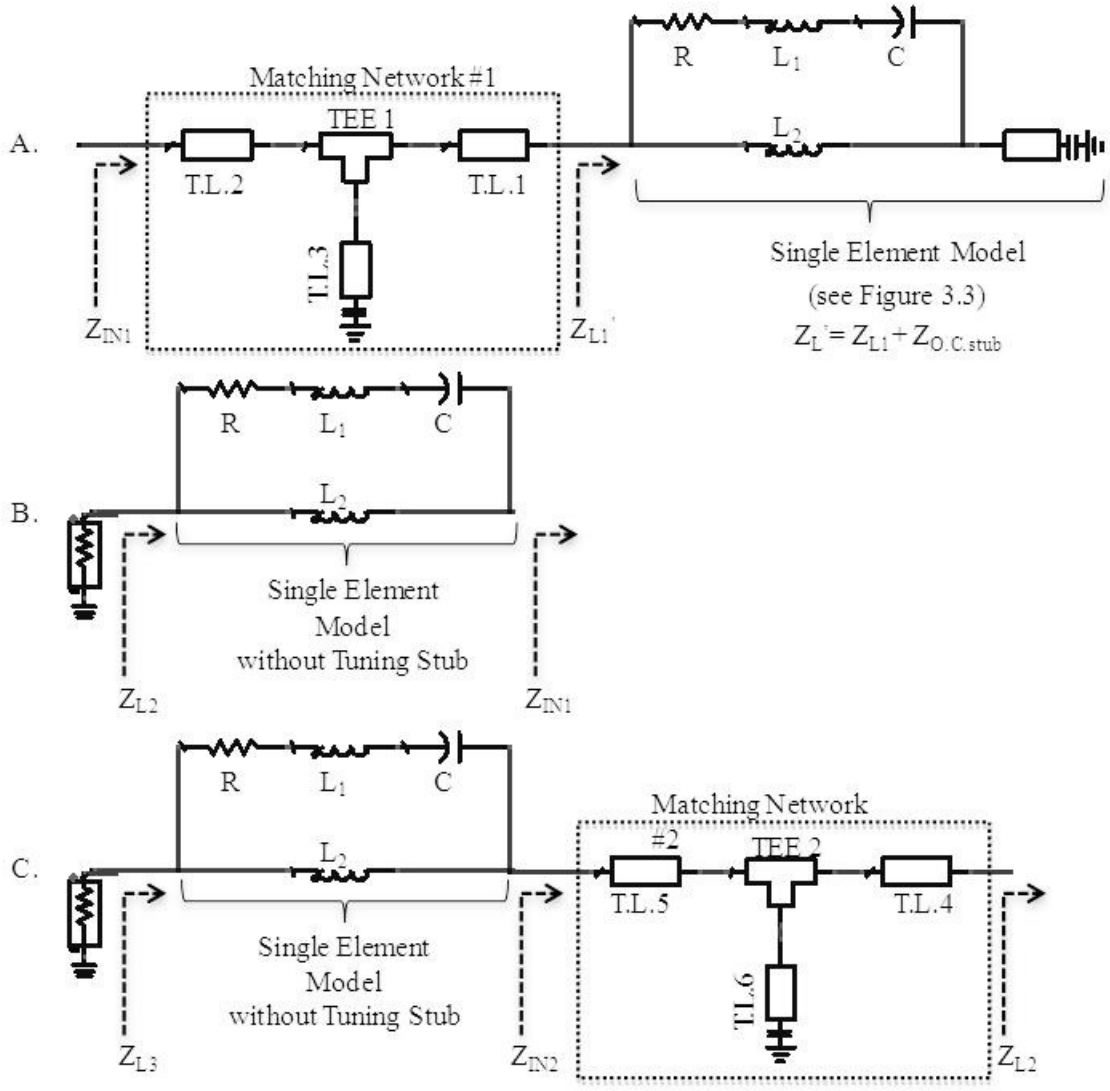

Figure 3.5 ADS schematic of two element model (A and B) and three element model (A, B without source termination, and C).

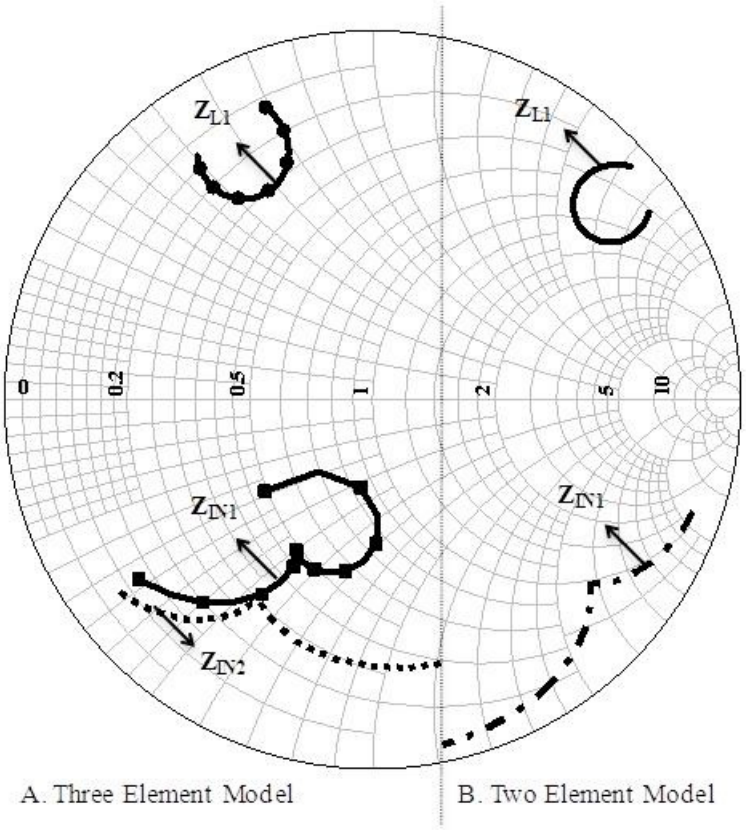

Figure 3.6 Impedances (reference Figure 3.5) for 2-element approach (B) and 3-element approach (A) (4.5 to 5.5 GHz).

Table 3.2 Matching network for 2-element approach.

	Length (mm)	Width (mm)
T.L 1	10.42	1.05
T.L.2	13.58	0.6
T.L.3	4.58	0.6

Table 3.3 Matching networks for 3-element approach.

	Length (mm)	Width (mm)
T.L 1	8.78	4.43
T.L.2	13.22	2.04
T.L.3	3	3
T.L.4	6	2
T.L.5	16	0.92
T.L.6	3.34	3

3.3 Four-Element Aperture-Coupled Antenna Sub-Array

In what follows, two configurations of series-fed four microstrip patch array that utilize planar design for ease of fabrication and signal routing are presented. Each element is an aperture-coupled patch, and a feed at each end of the array is used to excite a pair of elements in series (Figure 3.6). The inner patches have a short, open-circuit stub that extends beyond the coupling slot for impedance matching, and a second stub between elements is used to achieve equal power distribution between the slots, the feeding approach described in the previous section.

3.3.1 Frequency Beam-Stability at Broadside

The natural tendency of a series fed array to have beam tilting over frequency is circumvented by using opposing, anti-symmetric balanced feed points. The physical anti-asymmetry of the array about its center forces the currents going to each half of the array to be out of phase. In order to account for the difference in the feed-line directions, the signals applied to each end of the array are 180 degrees out of phase. Anti-phase components of the input signal at each end of the array force the E-field radiated by the each pair of elements to add rather than subtract in the broadside direction (Figure 3.7). Hence, the combination of the series feed network configuration and the out of phase dual-feed forces excitation symmetry about the center of the array, therefore keeping the elevation beam fixed at broadside independent of frequency. This approach makes this element suitable for low cost frequency-hopped phased array antennas.

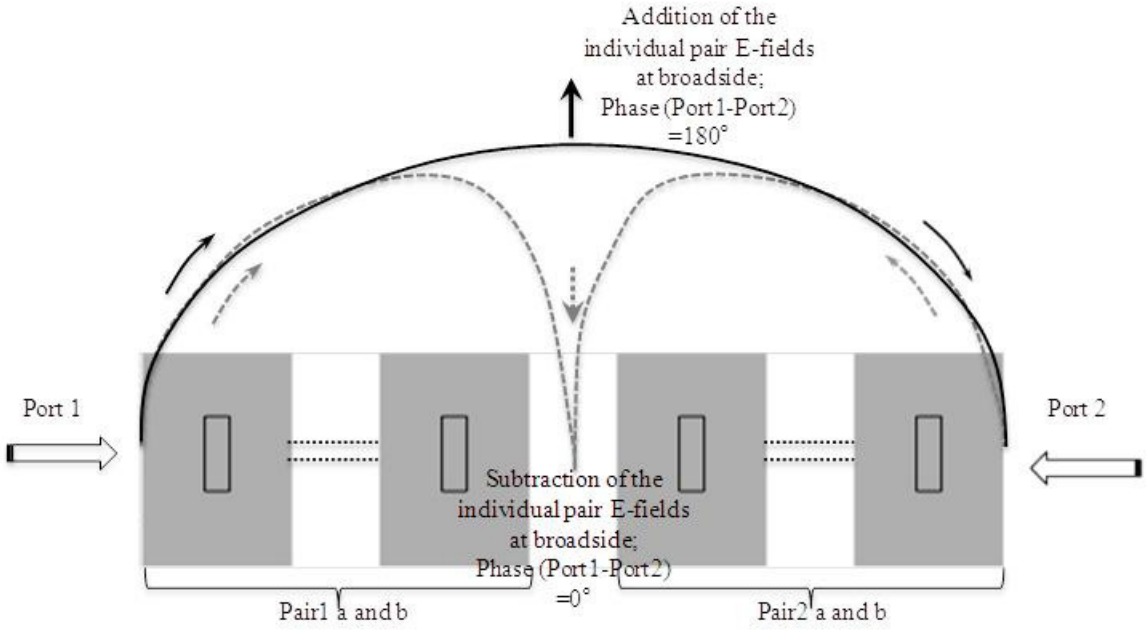

Figure 3.7 Summation of E-fields resulting from two pairs of elements (Pair 1 a and b; Pair 2 a and b) being fed 0° (dotted line) and 180° (solid line) apart.

3.3.2 Dual Feed Constraints and Applications

Two different four-element architectures presented here are a single and a dual-fed array topology. Single-fed array uses a coupler to provide 180 degree phase shift between two halves of the array. Dual-fed array does not employ a coupler, but rather uses two independent 180 degree out of phase signals at each end of the array to maintain pattern at broadside. Both single and dual-fed array structures were fabricated with intent to incorporate them into an omni-directional radiator. Thus, preference between the two is observed in view of their facility to be used for that particular application. Simple and and easy integration of omni-directional construct makes the single-fed array a preferred choice when only azimuth beam forming is desired. Furthermore, the number of external components in single-fed configuration is about half that needed for dual-fed array. The dual-fed design requires utilization of external couplers to provide two 180 degree out of

phase signals at each end of the array and as such is harder to accommodate within overall dimensions of the omni-directional construct. Alternatively, additional substrate layer with components fabricated using standard PCB techniques could be used to avoid the use of external components. Nonetheless, if there exists requirement for scanning of the array in elevation plane, dual feed must be utilized.

3.4 Dual Feed Approach Results

A dual series-fed, four microstrip patch array antenna is shown in Figure 3.8 and the characteristics of its matching network in Table 3.3, with additional information given in Table 3.4. While the real-valued Z_{in} at each end of the array could be further transformed in order to maximize return loss, in this design the value was sufficiently close to 50 Ohms and no additional matching at input was needed. Figure 3.9 shows the comparison of the return loss between the measurement and simulated data for the four-element array. The measured return loss of the fabricated array is >10dB over a 600MHz frequency range. It is believed that the discrepancy between the measured and simulated results is partially due to connector limitations, as those available for the initial measurements are not recommended for use beyond 4 GHz due to their large size. The limited extension of the substrate beyond the patch edges, which was approximately 250 mils, may also contribute to the differences in the measured data. Both of these issues are improved in single-fed second generation test structures. Figure 3.10 shows the measured and simulated E-plane radiation pattern.

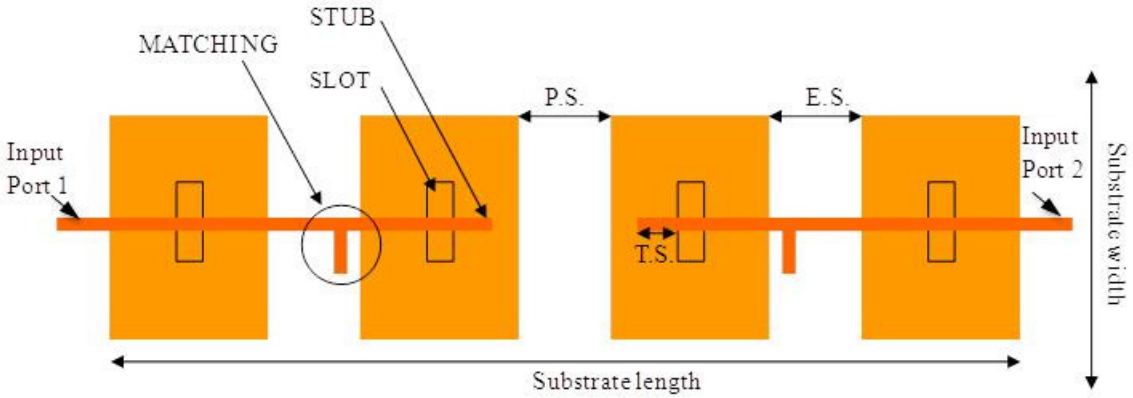

Figure 3.8 Illustration of the four-element dual-fed sub-array.

Table 3.4 Dual-fed array characteristics.

Array Element	Size (mm)
Substrate length	115
Substrate width	45
Tuning stub (T.S.)	3.6

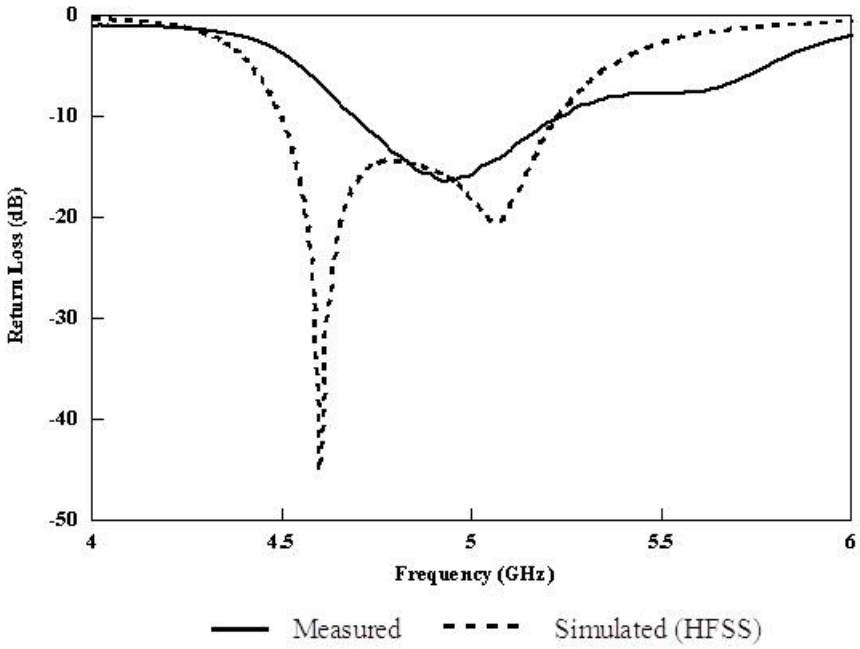

Figure 3.9 Comparison of measured and simulated results of the return loss (dB) of the four-element dual series-fed array.

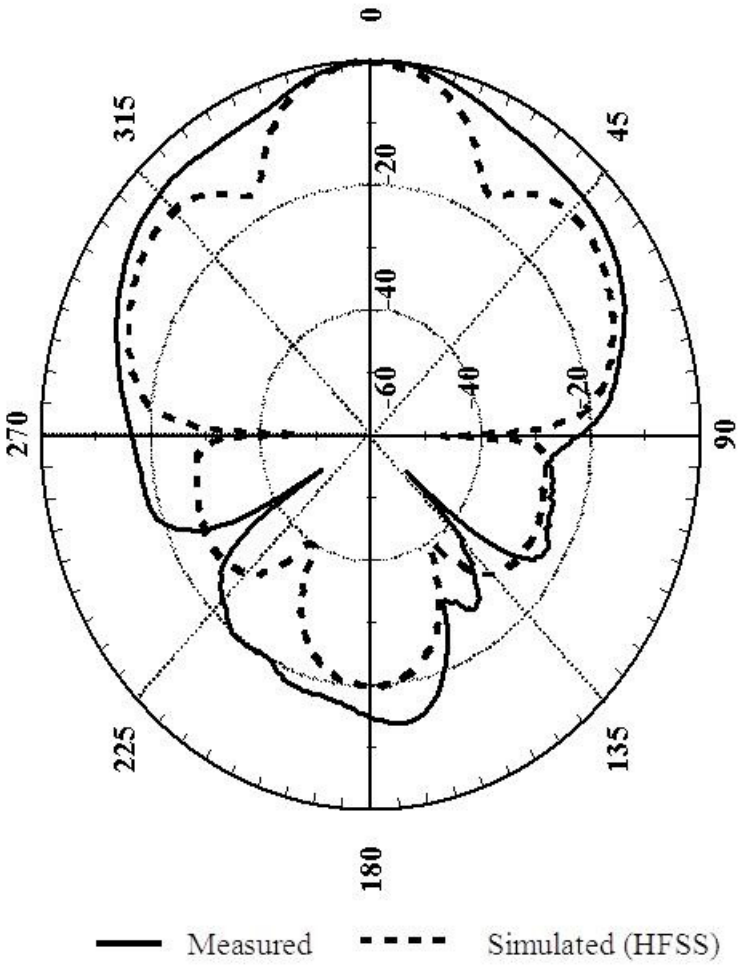

Figure 3.10 Comparison of measured and simulated results of E-plane radiation pattern of the 4 element dual series-fed array.

3.5 Single-Fed Aperture-Coupled Microstrip Antenna Sub-Array

A second generation test structure uses a 180 degree hybrid between two pairs of elements in both four- and six-element array. The advantage of integrating the coupler into the feed network is that a single feed-point is produced, which simplifies the construction of the omni-directional configuration described in next chapter. This however limits scanning capabilities of the arrays in the elevation plane unless additional

components are integrated in the array structure, as described in more detail in the following chapter.

3.5.1 180-degree Equal Power Split Hybrid Rat-Race Coupler Design

The four- and six-element sub-arrays include a 3-dB Rat-Race hybrid coupler (Figure 3.11). This coupler integrated into the center of the feed network provides an equal power, anti-phase (180° +/-2°) split between the two halves of the sub-array (Figure 3.12). Assuming proper phase balance from the coupler over the desired frequency band, this configuration ensures a fixed beam angle at least over the bandwidth of the 180 degree coupler. The microstrip lines leading into the coupler were meandered to reduce size and to avoid adverse effects of fringing fields near the coupling slots. A comparison of the simulation results between the array fed by the coupler, and the same array fed at each side by anti-phase signals showed negligible coupling effects from the close proximity of the coupler to the coupling slots for the patches.

Figure 3.11 Rat-Race coupler used in each single-fed sub-array architecture.

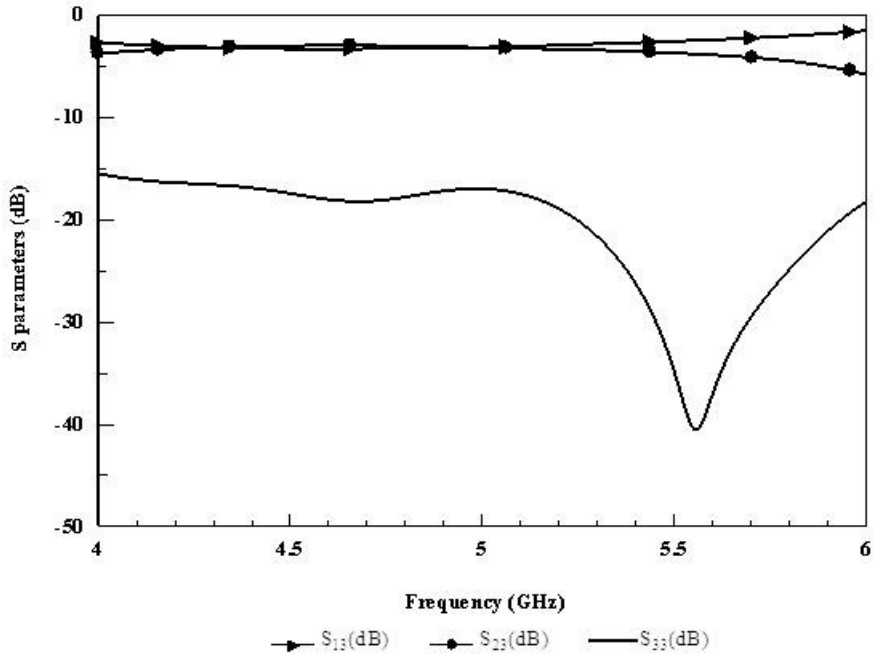

Figure 3.12 Simulated results (from Momentum) of the Rat-Race coupler used in each sub-array architecture.

3.5.2 Four Aperture-Coupled Antenna Sub-Array with a 180-degree Equal Power Split Hybrid Rat-Race Coupler

The four-element single-fed slot-coupled microstrip antenna sub-array was designed, as first explained in dual-fed architecture in [69] using the two-element model approach. As shown in Figure 3.13, each element in two 2-element pairs is identical to the geometry described in Table 3.1 (a), and the matching network of the first and second construction are those defined in Table 3.2. Other physical properties of the SA's are given in Table 3.5. Momentum was used to simulate the overall sub-array architecture and verify the model, and subsequently Ansoft's HFSS was used to account for the finite substrate dimensions. The three-element model was also utilized in the development of a six-element SA to validate the scalability of the proposed series-fed approach described in the next section.

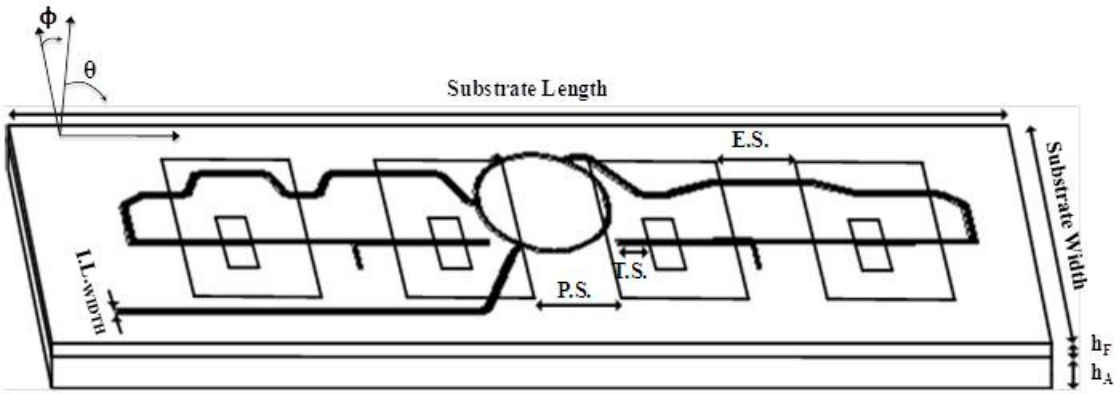

Figure 3.13 Illustration of the single-fed four-element sub-array.

Table 3.5 Single-fed four-element array characteristics.

Array Element	Size (mm)
Antenna substrate height (h_A)	3.17
Feed substrate height (h_F)	0.51
Substrate length	123.1
Substrate width	36.6
Element spacing (E.S.)	11.6
Pair spacing (P.S.)	11.6
Input line width ($I.L._{WIDTH}$)	1
Tuning stub (T.S.)	3.6

The first generation single-fed sub-arrays were fabricated using standard lithography and copper etching methods. Sub-arrays were fabricated and the return loss of each six sub-arrays was measured to verify reasonable uniformity in the prototype fabrication process. As shown in Figure 3.14, the measured S_{11} for all six sub-arrays are in somewhat close agreement. The variation that is observed may be due to using an inconsistent amount of non-conducting epoxy in bonding each antenna layer and feed layer together. The variation in the sub-array performance will naturally impact the fidelity of the omni-directional coverage, so more robust multi-layer bonding methods are preferred.

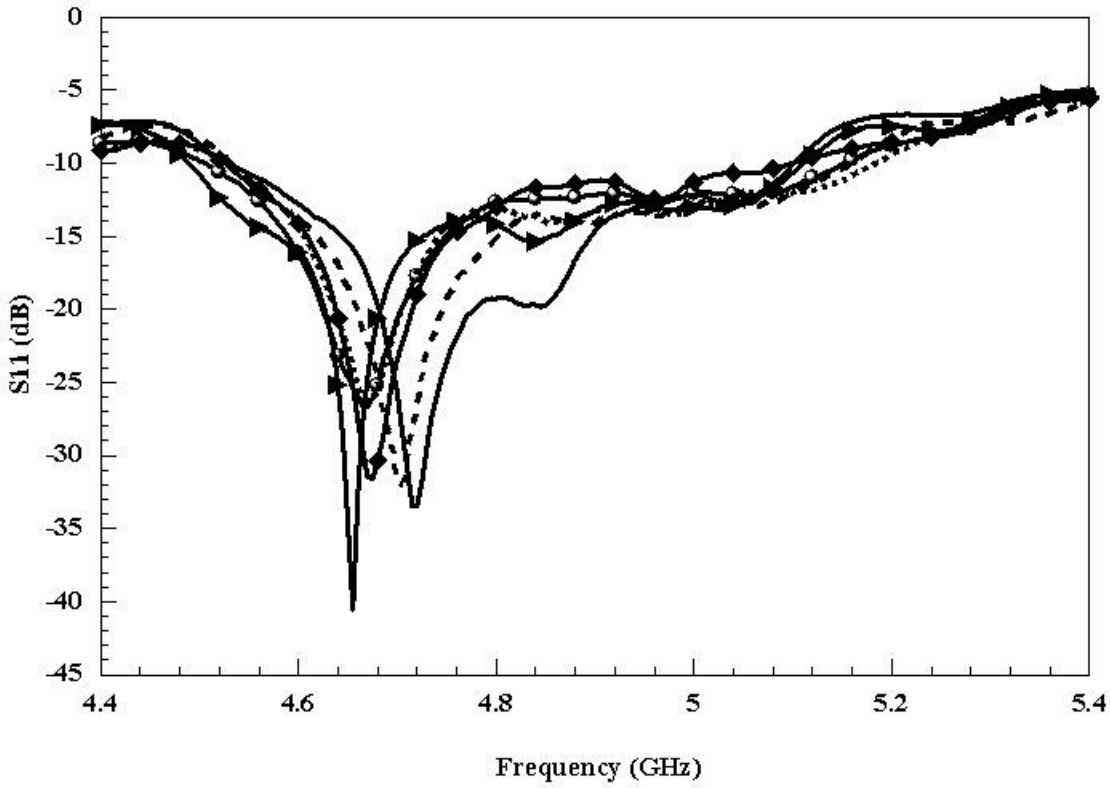

Figure 3.14 Measured S_{11} for six first generation single-fed sub-arrays.

Additional analysis of the single-fed sub-array with the aim of narrowing down the parameters with greatest impact on uniform omni-directional pattern, followed the fabrication of the first single-fed prototype and its measured results. It was found that the width of the second prototype must be adjusted in an effort not to have a scalloped omni-directional coverage. Thus, six second generation single-fed four-element sub-arrays were prepared. The S_{11} of the sub-arrays is given in Figure 3.15, which includes measured data, simulation results from ADS (equivalent circuit model) and HFSS results. Each of the six sub-arrays has at least 750 MHz of bandwidth, with return loss greater than 10 dB from 4.45 GHz to 5.2 GHz. Based on HFSS simulation results, the sub-array maximum directivity is 11.5 dB in the broadside direction. Measured and simulated

radiation patterns are given in Figure 3.16. The half-power beamwidth is 26˚ and sidelobe levels are approximately 8-13 dB below the main lobe. Differences in the elevation measurement between the six arrays are attributed to fabrication tolerances associated with the circuit milling process that was used, antenna-to-feed substrate alignment discrepancies and the possible existence of air gaps between the two substrate layers.

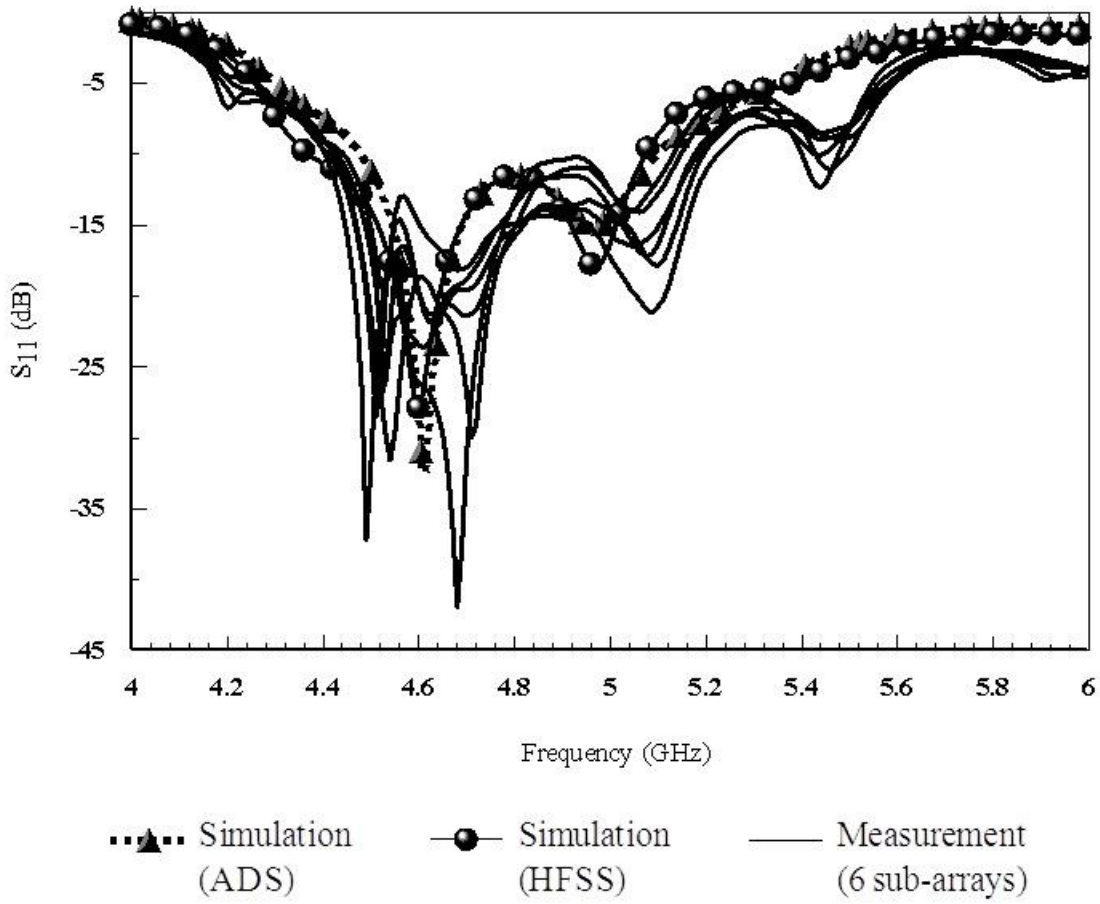

Figure 3.15 Comparison of S_{11} between ADS and HFSS simulations with measurement data of six four-element sub-arrays.

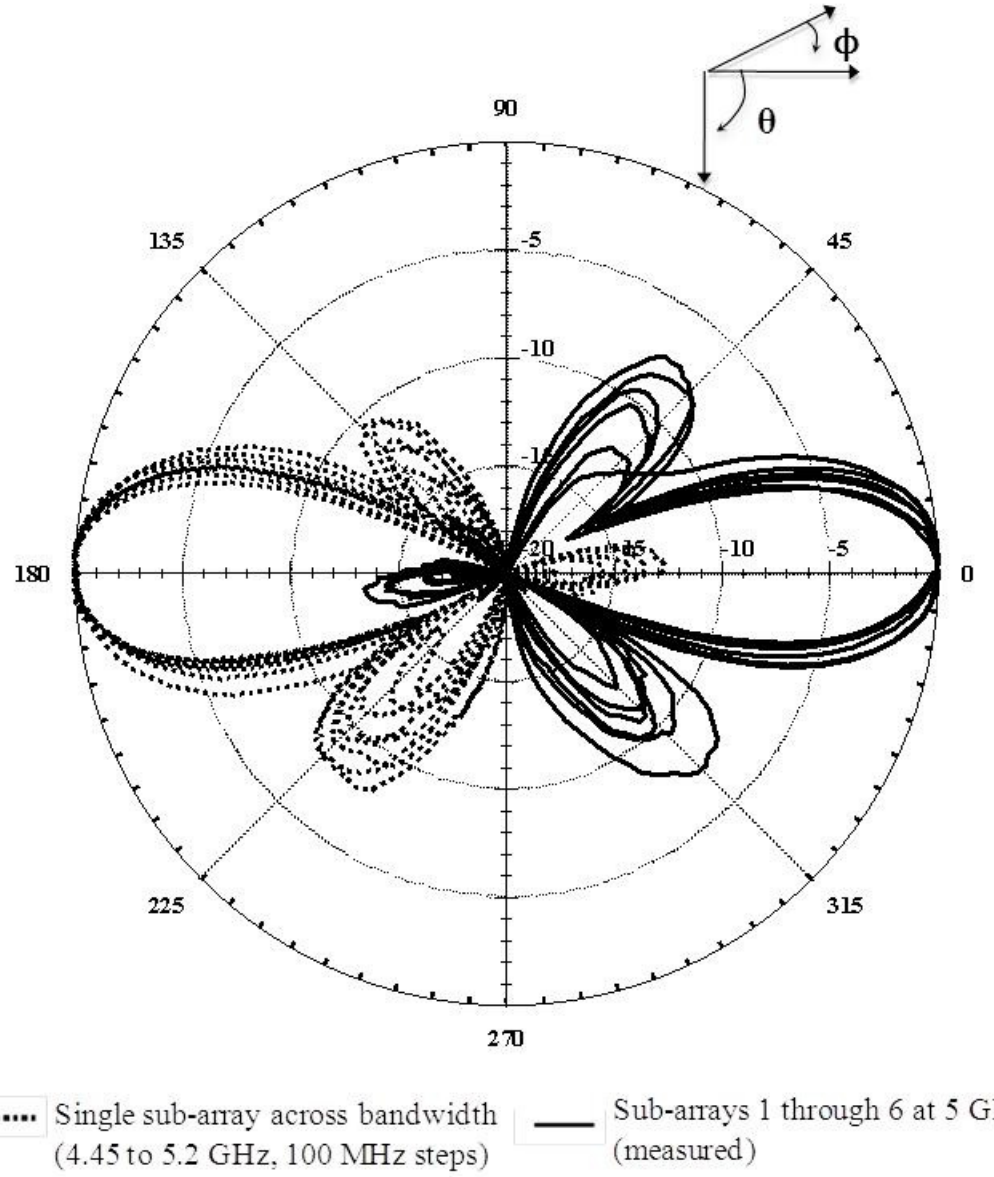

Figure 3.16 Comparison of the E-field co-pol measurement of the single four-element sub-array across bandwidth and the six four-element sub-arrays that comprise the hexagonal configuration.

3.5.3 Six-Element Aperture-Coupled Antenna Sub-Array with a 180-degree Equal Power Split Hybrid Rat-Race Coupler

Six-element array was designed in order to examine whether the proposed series-fed approach can be successfully used to develop N-element arrays. In addition, greater directivity can be achieved when two antenna elements are added. Thus, the goal was to

develop a single antenna element that now uses a third of the input power instead of half as was the case in the four-element array. Subsequently, matching network is used to distribute the input power evenly among the antenna elements in each half of the six-element array.

A single antenna element with a lower input impedance compared to the one used in the four-element arrays was designed by altering the size of the coupling aperture and its position with respect to the antenna. The effect of coupling slot length was discussed in Chapter 2. It was noted that the resonant frequency and the real part of input impedance (amount of coupling) are adjusted with proper slot length, while its imaginary part of the input impedance is changed with variation in the length of the tuning stub. The centered position of the slot with respect to the antenna achieved maximum coupling between those two. Likewise, the width of the feed line beneath the slot determines the amount of coupling. If however input impedance of the single patch is to be decreased by large amount without changing the resonant frequency, as needed in a 3-element approach in order to distribute power evenly among elements, adjusting the slot length alone is insufficient. Thus, in order to decrease input impedance of each element, the coupling slot was moved off-center and the width of the feedline was adjusted to maximize coupling. The effect of offsetting the slot on input impedance is in accordance with analysis in [20], where it was found that input impedance decreases as the slot is moved along its length and by large amount along its width.

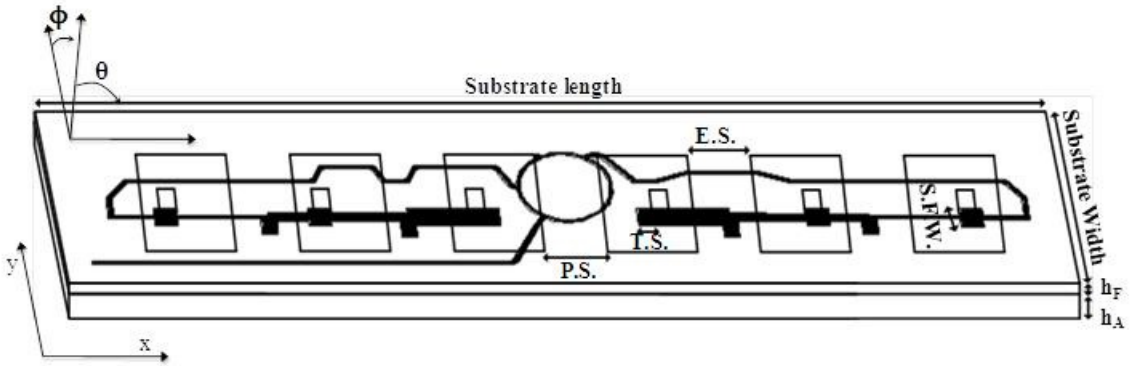

Figure 3.17 Illustration of the six-element sub-array (dimensions shown are in mm).

The networks were also designed to ensure that the input impedance at each end of the array is 50 Ω. The matching networks consist of feed lines and open-circuited stubs in between, as used in the four-element formations. The input impedance at each antenna element was adjusted to ~Z_{in}/3 or 17 Ω by moving the coupling slot off center. The coupling slot dimensions, its location and the widths of each of the series transmission lines composing the matching networks were designed and optimized using Ansoft's HFSS. Dimensions of the array other than those of the matching network are given in Table 3.6.

Table 3.6 Six-element sub-array characteristics.

Array Element	Size (mm)
Antenna substrate height (h_A)	3.17
Feed substrate height (h_F)	0.51
Substrate length	185
Substrate width	36.6
Element spacing (E.S.)	11.5
Pair spacing (P.S.)	11.5
Tuning stub (T.S.)	1.73
Slot Length (S.L)	3
Slot Width (S.W.)	9
Slot Offset in x(S.O.x)	3
Slot Offset in y (S.O.y)	2
Slot Feedline Width (S.F.W)	2.5

The six-element slot coupled microstrip antenna array has ~16% bandwidth and S_{11} below 10 dB from 4.54 to 5.34 GHz as shown in Figure 3.18. Discrepancies between measured and simulated results in the S_{11} data are most likely due to manual assembly of the antenna and feed layers and potential air gaps between these layers.

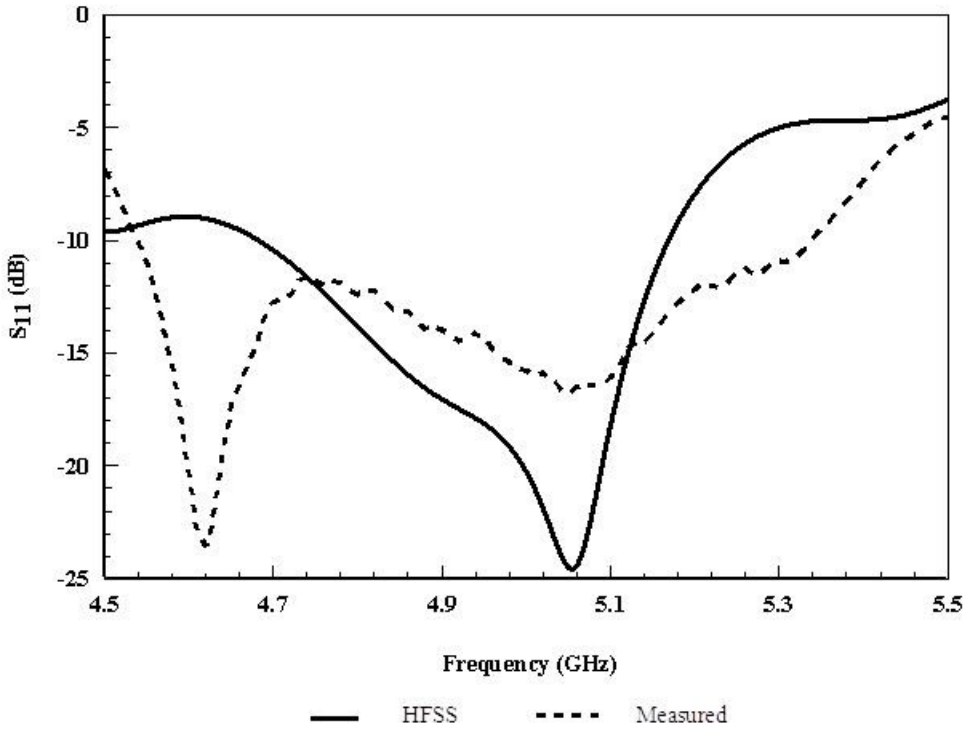

Figure 3.18 S_{11} (dB) of the six-element array.

The antenna array pattern was measured in both azimuth and elevation directions (Figure 3.19 and Figure 3.20). Both E- and H- plane patterns show that the measured results of the fabricated array correspond well to the HFSS simulation, with the exception of slightly higher side lobe levels seen in the measured E-plane pattern.

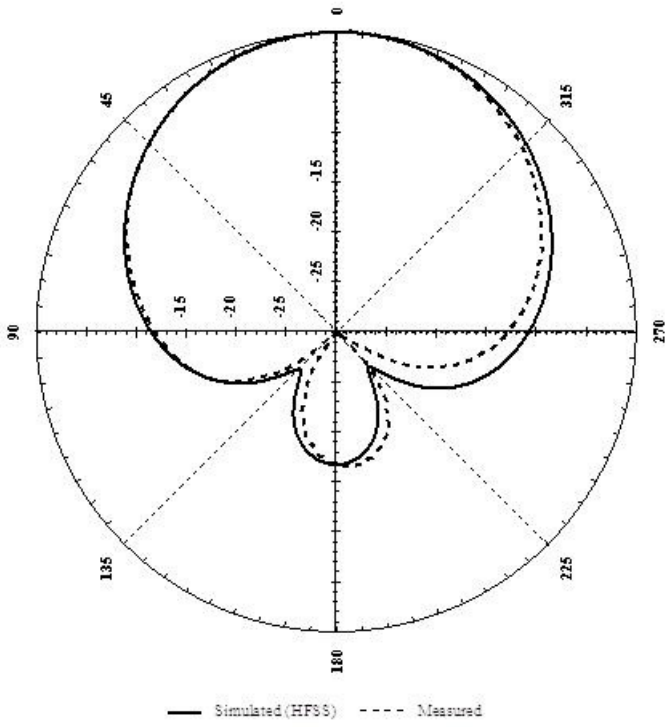

Figure 3.19 H-plane pattern at 5 GHz (φ-plane).

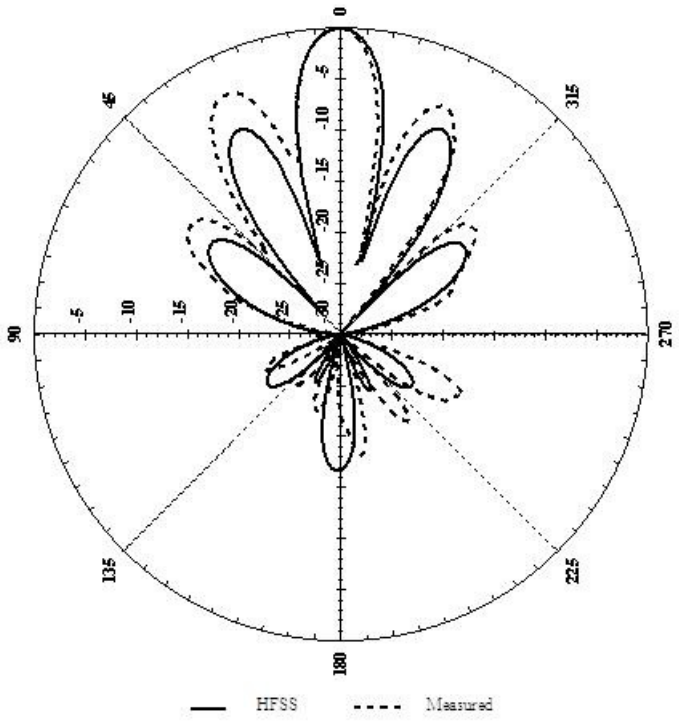

Figure 3.20 E-plane pattern at 5 GHz (θ-plane).

The elevation beam-pointing stability versus frequency for the fabricated array is shown in Figure 3.21. The array has 15˚ half-power beamwidth and the side lobe levels are at 28˚ with respect to the main lobe. The pattern stability with frequency is valid over the entire operational bandwidth and can be noted from 4.5 GHz to 5.5 GHz as shown in Figure 3.21. The gain of the array was measured to be 12.6 dB, compared to 12.95 dB that the HFSS simulation predicted. Further optimization of the arrays parameters may be done in HFSS to improve the gain performance.

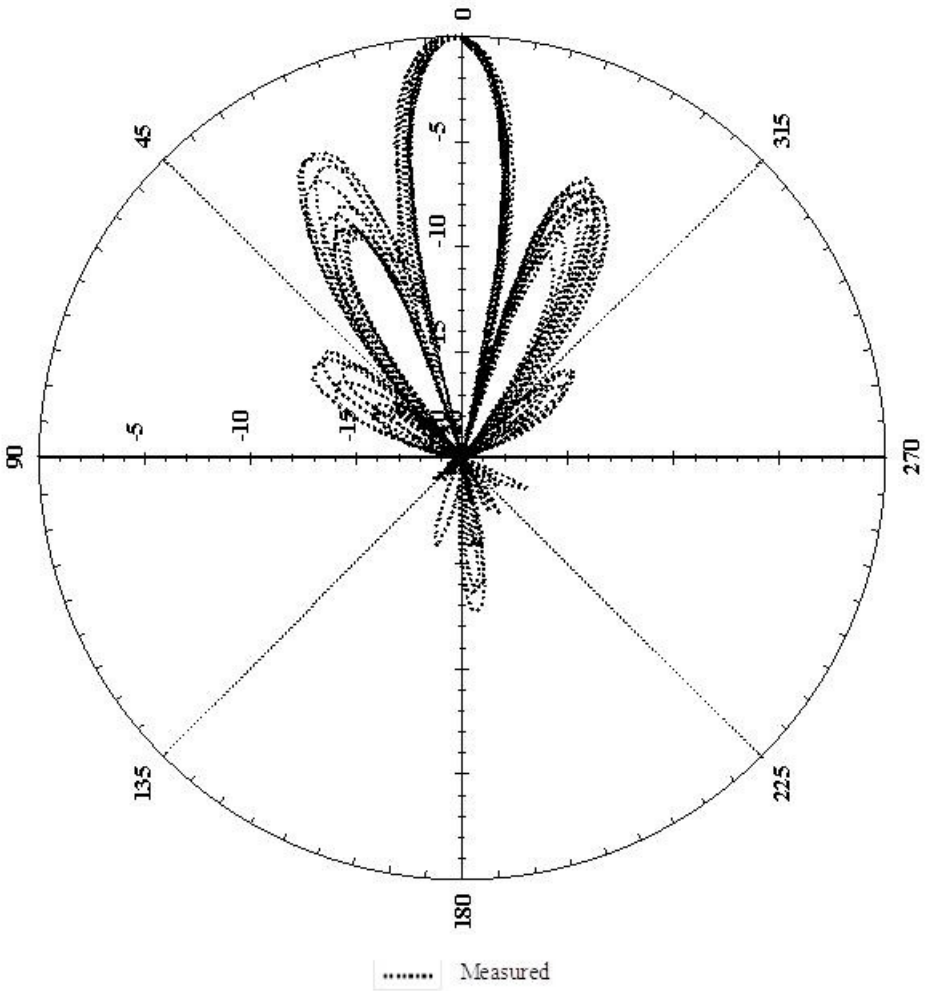

Figure 3.21 E-plane pattern over frequency (θ-plane, from 4.5 GHz to 5.5 GHz, 100 MHz increments).

3.5.4 Impact of Increasing the Number of Antenna Elements

The simulated directivity of the six-element SA was 13 dB, a 1.5 dB increase over the four-element SA, while the bandwidth was somewhat smaller compared to the four-element design. As mentioned, additional optimization could lead to both wider bandwidth and higher directivity in the six-element design. In general, addition of each two subsequent elements (one to each half of the array) could lead to 1-3dB increase in directivity, where special attention must be paid to applying proper excitation amplitude and phase to the elements at each end of the array, and the element-to-element separation in order to minimize side-lobes.

3.6 Conclusion

Dual and single-fed with 180 degree hybrid integrated N-element configurations for use in a 3-D omni-directional implementation were presented. In all configurations, the elevation beam-angle is fixed at broadside due to the use of an anti-symmetric feed from both ends of the array. An inter-element impedance matching approach, implemented in both four and six-element aperture fed microstrip antenna arrays and thus scalable to N elements, is shown to balance the excitation amplitude at each element. The feeding methodology can be extended to a series arrangement of different planar antenna elements, e.g. slots, dipoles etc.

CHAPTER 4:

HEXAGONAL CONFIGURATION OF SINGLE-FED FOUR-COUPLED ANTENNA SUB-ARRAYS

4.1 Introduction

The objective of this work was to develop a low-cost, medium gain omni-directional antenna operating in the C-band that enables eventual integration of electronics for radiation pattern control. It is demonstrated that an omni-directional radiator with stable beam pointing can be effectively realized by combining multiple series-fed N-element aperture-coupled arrays presented in Chapter 3 into hexagonal arrangement. Planar designs were not considered in this work. Alternative approaches to realize omni-directional radiators were mentioned in Chapter 1. These topologies, in general, either suffer from beam-pointing variation over frequency, or do not offer the capability for beam steering for attitude correction, and do not facilitate advanced beam-reconfiguration options such as eliminating coverage from certain sectors for jamming avoidance. Unlike those approaches, a hexagonal arrangement of 1-D arrays, as this work presents, would allow for azimuth beam-steering if an appropriate network (e.g. power distribution network) was used. In addition, the concept of elevation beam steering using dual-fed structures detailed in the previous chapter is also presented. The amount of scanning achievable, both in azimuth and elevation plane, with present configuration of dual-fed array is also explained.

A cylindrical arrangement of six four-element arrays using series feed mechanism for N-element slot-coupled microstrip antenna arrays is shown to achieve optimum omni-directional beam characteristics and exhibit pattern stability over frequency in the C-band. The impact of using different number of N-element arrays to assemble omni-directional topology is shown. The cylindrical arrangement is measured to have a gain of 6 dB over 750 MHz of bandwidth. A closed-form omni-directional pattern analysis is also developed.

4.2 Omni-Directional Array Pattern Synthesis

The evolution of the overall omni-directional pattern as one to five individual SA contributions are added is presented in Figure 4.1. As additional arrays are turned on, the angle of maximum radiation continues to rotate to the center of the active portion of the antenna. The superposition of all six sections yields an omni-directional pattern. By using an appropriate power distribution feed network power can be re-distributed in this manner to generate an expanding omni-directional coverage, or coverage in selected portions of the azimuth plane.

Herein two generations of a cylindrical antenna construct are presented. The second generation is depicted in Figure 4.2. These two variations used two alterations of the single-fed four-element arrays described in Chapter 3.

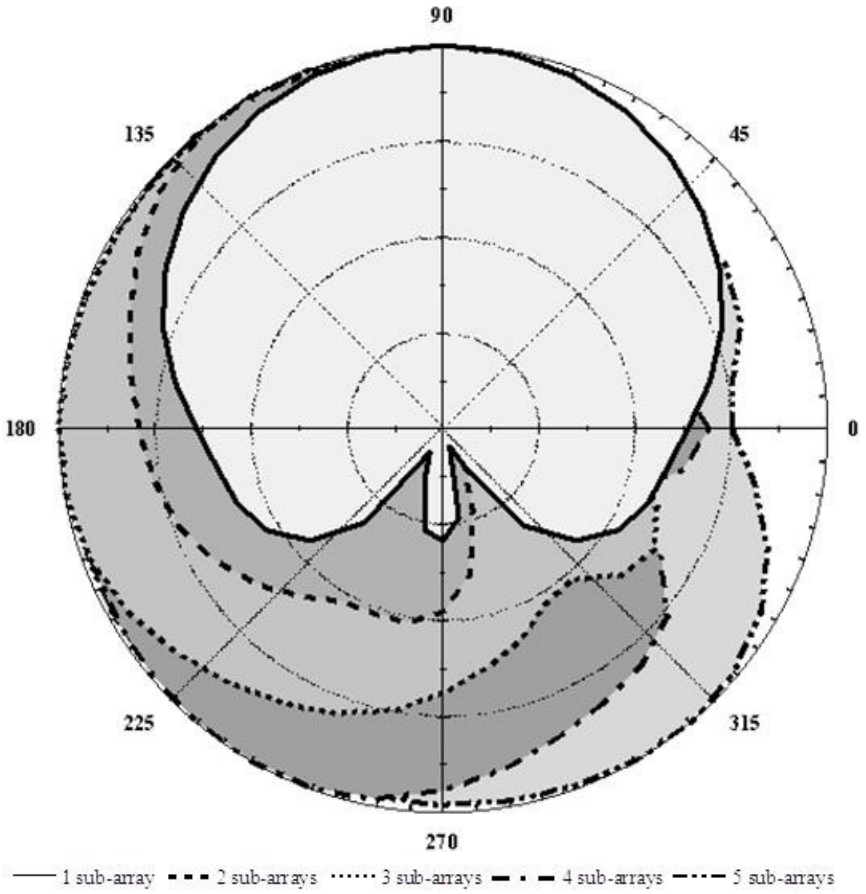

Figure 4.1 The effect of adding (turning on) subsequent sub-arrays on azimuth (H-plane) pattern simulated in HFSS.

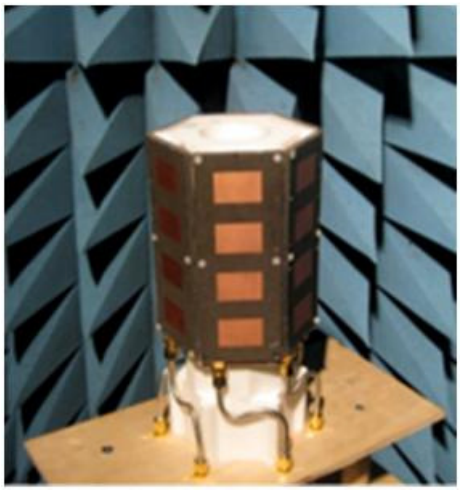

Figure 4.2 Picture of the fabricated hexagonal structure with six four-element sub-arrays.

4.2.1 Omni-Directional Pattern Characteristics

To assemble the 3-D structure six fabricated sub-array feed layers were first mounted on a hexagonal Teflon apparatus. The Teflon holder was designed to provide structural support for the sub-arrays while minimizing electromagnetic interaction with the feed layers that face toward the center of the holder. In the first iteration, copper tape was used to bond the ground planes of adjacent sub-arrays together in order to provide continuity of the ground plane around the 3-D structure. Silver epoxy was utilized to ensure proper connection between ground planes and the copper tape. Continuity of the ground layer was thought to be essential in preventing the occurrence of nulls in the azimuth radiation pattern. Proper alignment of the feed network to the patch antenna layer and mounting of sub-arrays on a Teflon holder was achieved through the use of Teflon screws as alignment marks. The six sub-arrays were fed using an 8-way 0-degree coaxial coupler (Mini Circuits P/N ZB8PD-6.4) with two ports terminated in a matched load. The 8-way coupler used to measure the cylindrical configurations is operational across the whole bandwidth of the sub-arrays. The return loss at the input to the coupler is greater than 13 dB from 4.45 to 5.2 GH as shown in Figure 4.3.

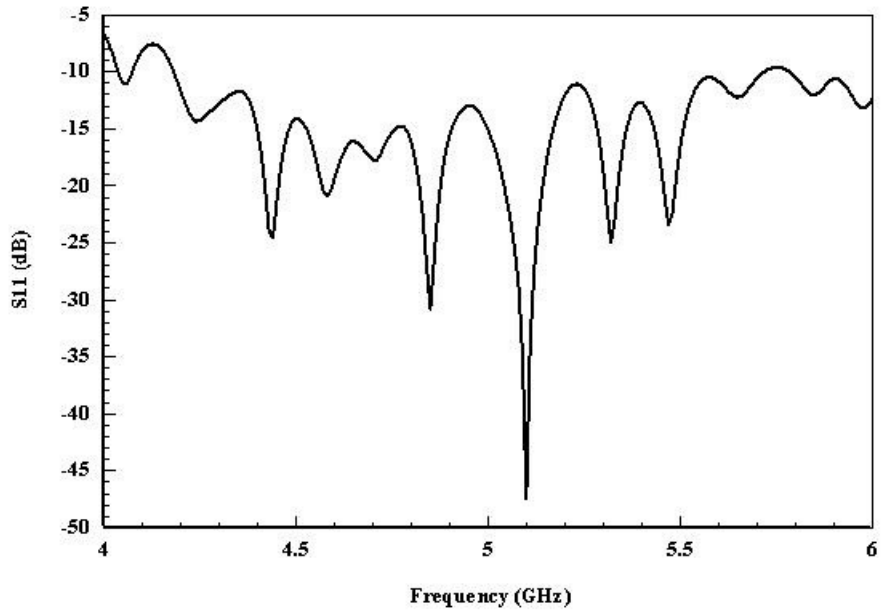

Figure 4.3 S_{11} of the 8-way coupler used to measure omni-directional pattern.

The 3D structure was simulated in Ansoft's HFSS by assembling six sub-arrays in a hexagonal manner as shown in Figure 4.4 (the hexagon (or cylinder) around the array structure is the radiation boundary used in the simulations). The 3-D plot of the simulated radiation pattern given in Figure 4.4 illustrates excellent omni-directional coverage. Although the antenna is not perfectly cylindrical (rather, it is hexagonal) the variation in gain over azimuth was only approximately +/- 0.5 dB. The simulated maximum gain was ~6 dB at 5 GHz.

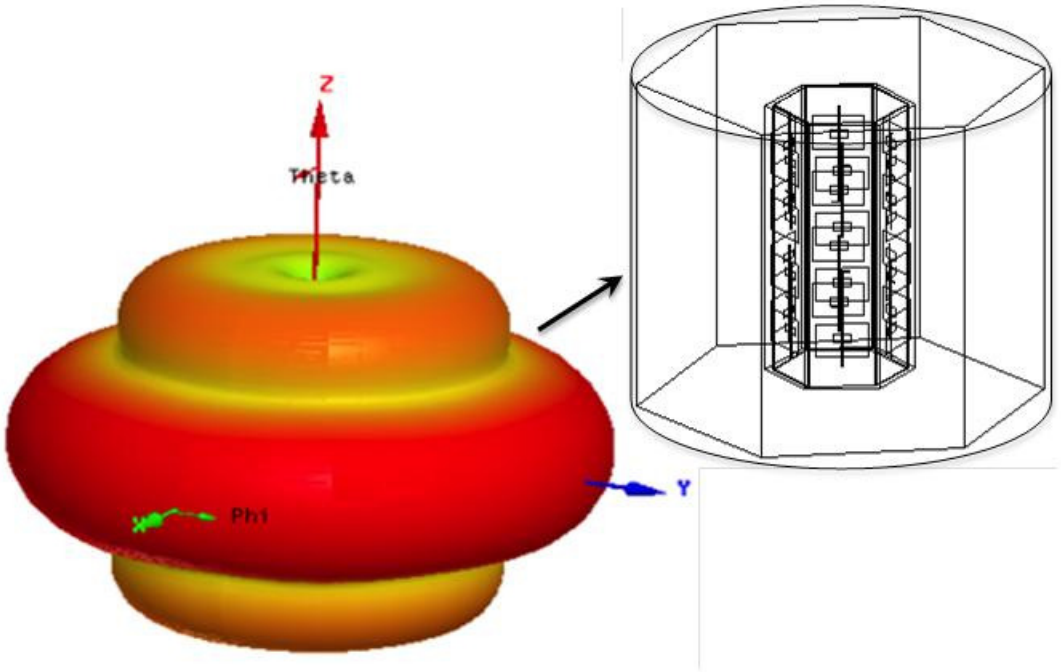

Figure 4.4 3-D polar plot of the hexagonal structure simulated in HFSS.

Comparisons between measured and simulated radiation patterns are given in Figures 4.5 and 4.6. The measured azimuth radiation pattern at 5GHz agrees closely to the simulated results from HFSS (Figure 4.5), and demonstrates a variation of +/-1.5 dB over the 360-degree span. Although the antenna measurement system that was used did not readily enable a full elevation cut to be measured, the data taken between +/-45 degrees is in good agreement with the HFSS simulation results (Figure 4.6). The simulated and measured 3-dB beam widths are 35 and 30 degrees respectively.

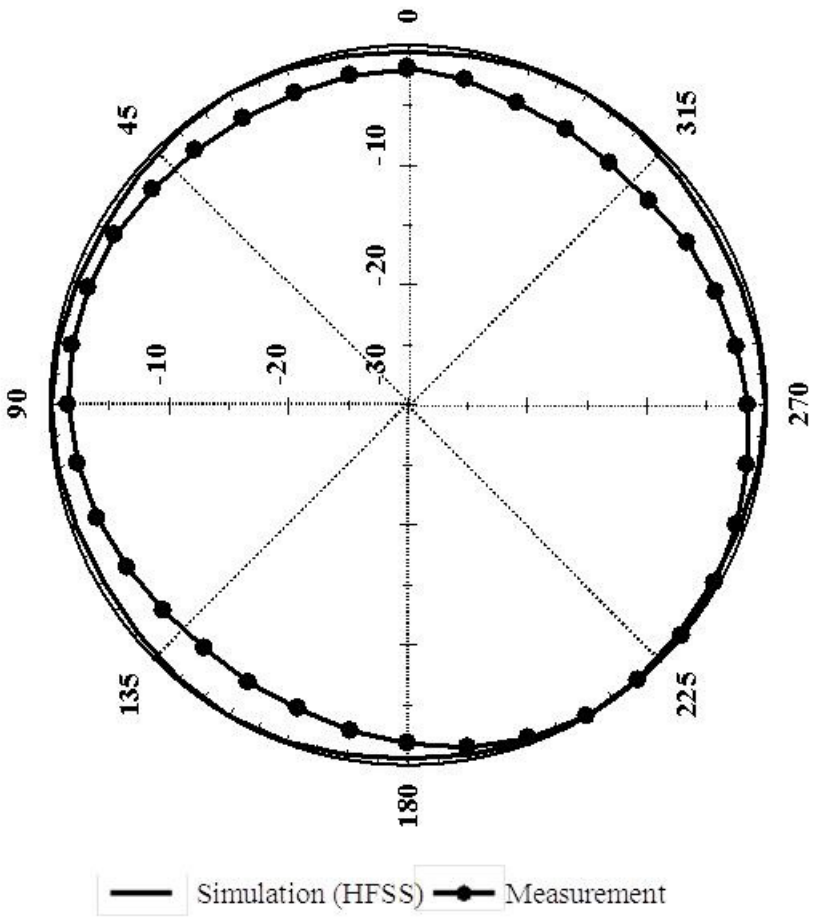

Figure 4.5 Azimuth radiation pattern at θ=90 degrees (broadside) for the hexagonal structure.

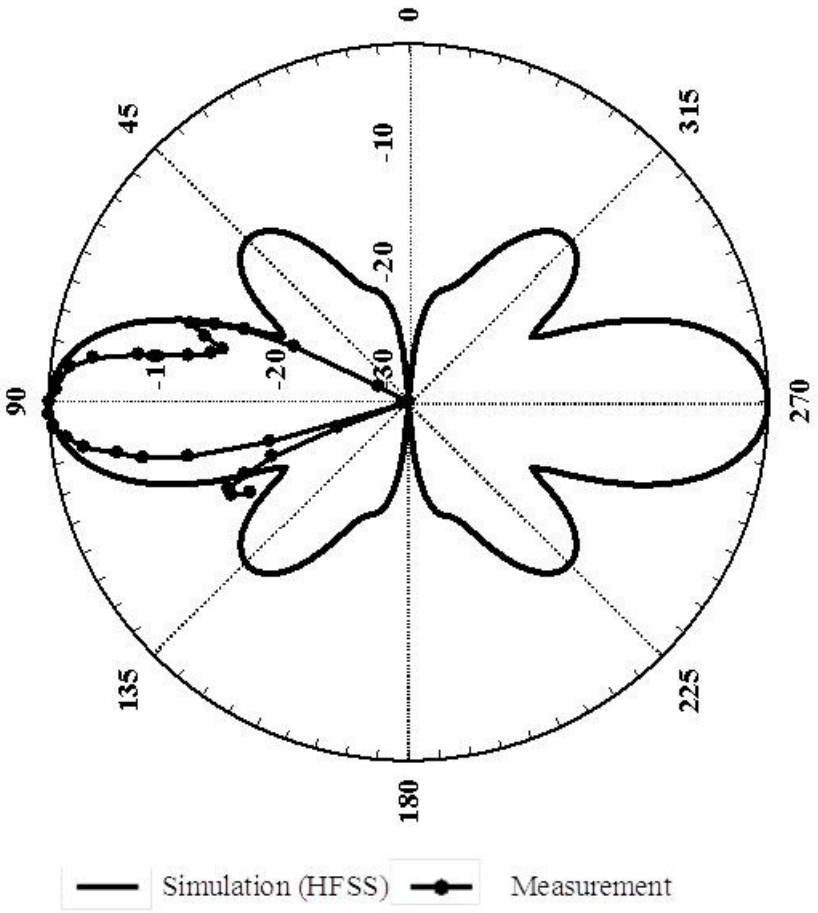

Figure 4.6 Elevation radiation pattern for the hexagonal structure.

Following the fabrication and measurement of the first generation omni-directional radiator, the aim was to further analyse the impact of different sub-array parameters that may had impact on azimuth radiation pattern variation of +/-1.5 dB rather than +/-0.5 dB as predicted by simulation. In doing so, additional HFSS simulations were performed in order to investigate the impact of increasing the size of the ground plane of individual sub-arrays, and thus the substrate surrounding the patch elements. The fabricated sub-arrays in the first measured omni-directional radiator had 10mm of ground/substrate extending beyond the edges of patches, partly to accommodate the Teflon alignment screws. S_{11} results for different ground plane extensions for the single

sub-arrays showed that minimal performance variation was introduced for ground extensions ranging from 4.8 to 12.8 mm (Figure 4.7). The impact of ground plane size on the sub-array radiation pattern was likewise relatively small, with the most noticeable differences occurring at the back lobe direction (Figure 4.8). The results of this study imply that the sub-array widths can be reduced in order to shrink the diameter of the hexagonal structure, and potentially further improve the uniformity of the omni-directional coverage. This change, however, necessitated changes in the assembly process used to mount the sub-arrays to the Teflon center support.

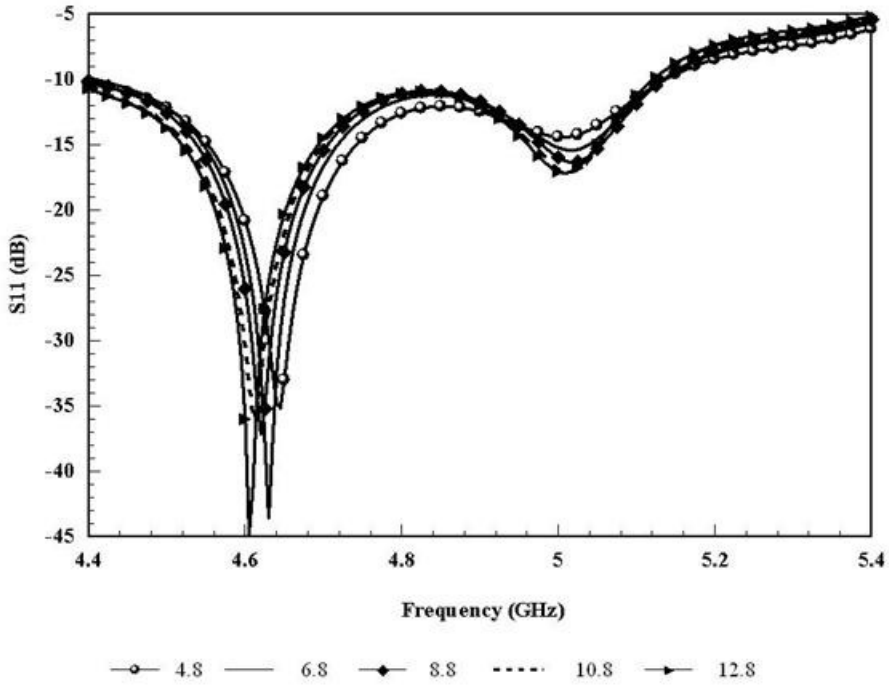

Figure 4.7 Return loss for different sizes of ground plane for the single sub-array (dimensions are in mm).

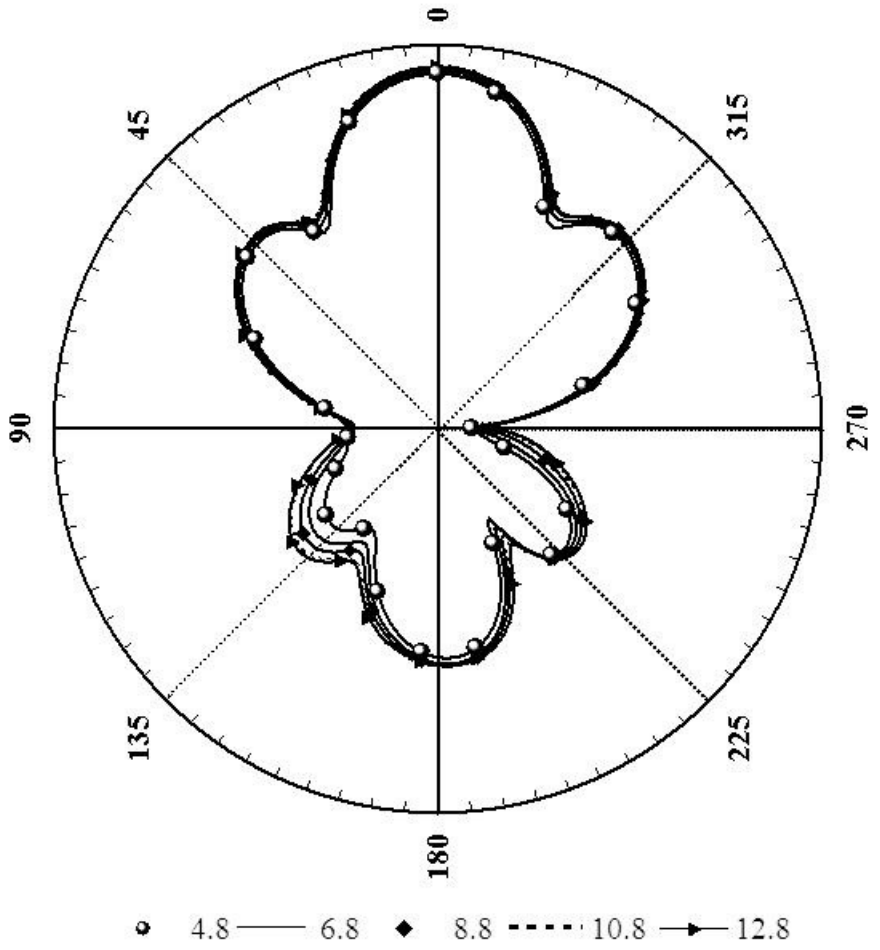

Figure 4.8 Elevation radiation pattern at φ=0 degrees (broadside) for different sizes of ground plane for a single sub-array.

In the second iteration of the hexagonal structure, the sub-arrays were also secured on a Teflon holder such that their individual ground planes formed a uniform surface, however silver epoxy and copper tape were deemed not necessary. It was believed that improvement made on the second iteration of single-fed sub-arrays will be sufficient to provide necessary improvement in omni-directional coverage. In particular, even though the study of the effect of ground plane size of each sub-array revealed that the individual sub-array pattern was not significantly influenced by it, the non-scalloped

omni-directional coverage was found to be highly dependent on the overall circumference of the hexagon. Thus, the width of the second-generation single-fed four-element arrays was significantly reduced.

The azimuth radiation pattern at $\theta=90^\circ$ for the 3-D second generation hexagonal configuration is shown in Figure 4.9. The broadside gain was measured to be 6 dB and it varies by less than +/-0.6 dB versus azimuth across the bandwidth of the antenna (4.45 GHz to 5.2 GHz). The gain at any specific broadside angle also varies less than +/- 0.6 dB across the same bandwidth (Figure 4.10). The measured pattern is in close agreement to the simulated pattern from HFSS. The differences in azimuth radiation pattern between measured and simulated values may be due to non-identical arrays composing the structure. Difficulty lies in an attempt to produce six identical multi-layer arrays by manual assembly. The measured omni-directional pattern shown in Figure 4.9 could be further improved by fabricating the sub-arrays using photolithography techniques along with the use of a laminating press that would ensure proper alignment and the absence of air gaps between antenna and feed substrates. Simulated results of the 3-D six-element sub-array design showed that the directivity could be increased by at least 1-2 dB by adding the two additional patches to each SA.

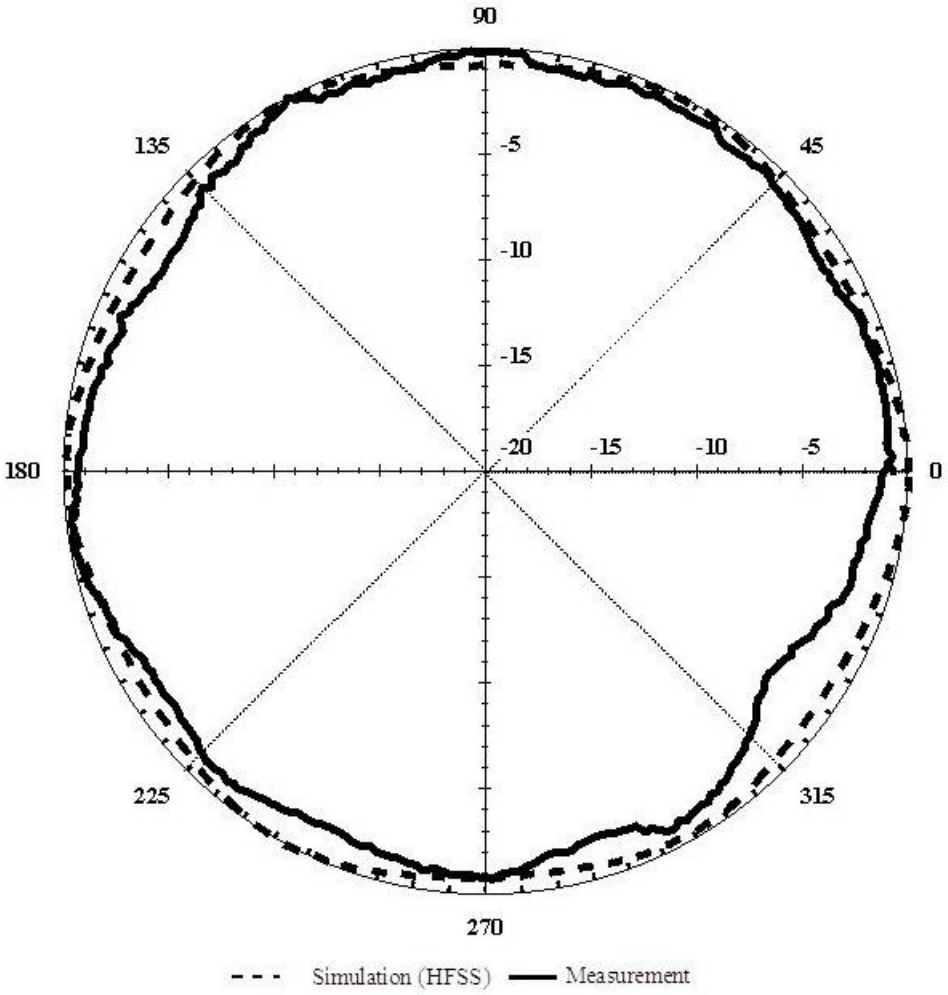

Figure 4.9 Measurement vs. HFSS simulation of azimuth pattern for the hexagonal four-element structure at 5 GHz.

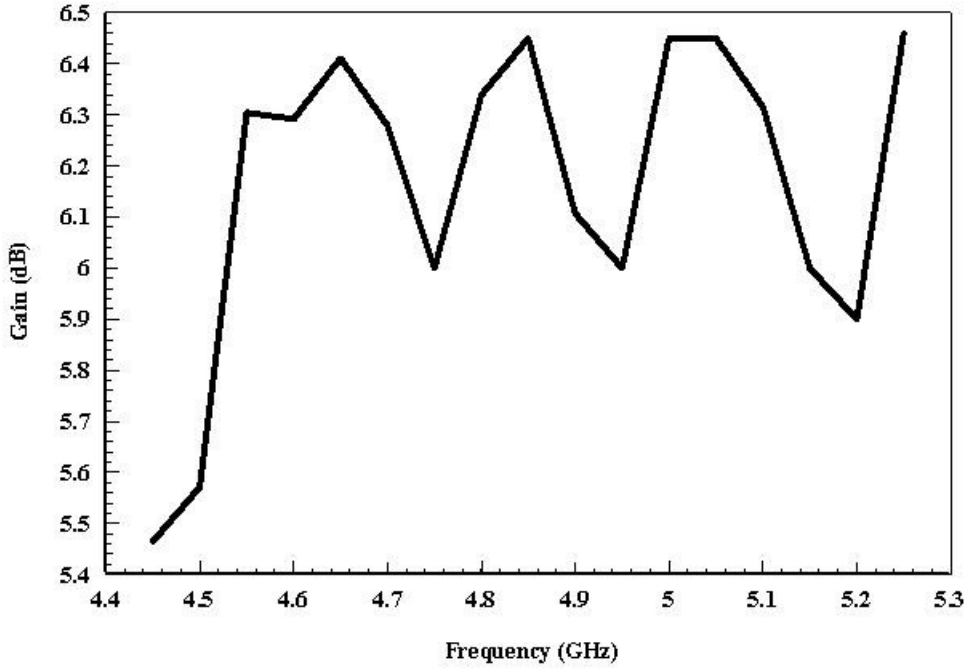

Figure 4.10 Gain of the hexagonal structure over frequency.

The azimuth pattern was measured across the range of frequencies and corresponds closely to the simulated results shown in Figure 4.11. The elevation pattern stability was presented in the previous chapter (Figure 3.16). The simulation was performed in Ansoft's HFSS from 4.5 GHz to 5.5 GHz. It can be seen that the greatest variation of pattern across 1 GHz of bandwidth is 1 dB, and that is between two ends of the frequency range.

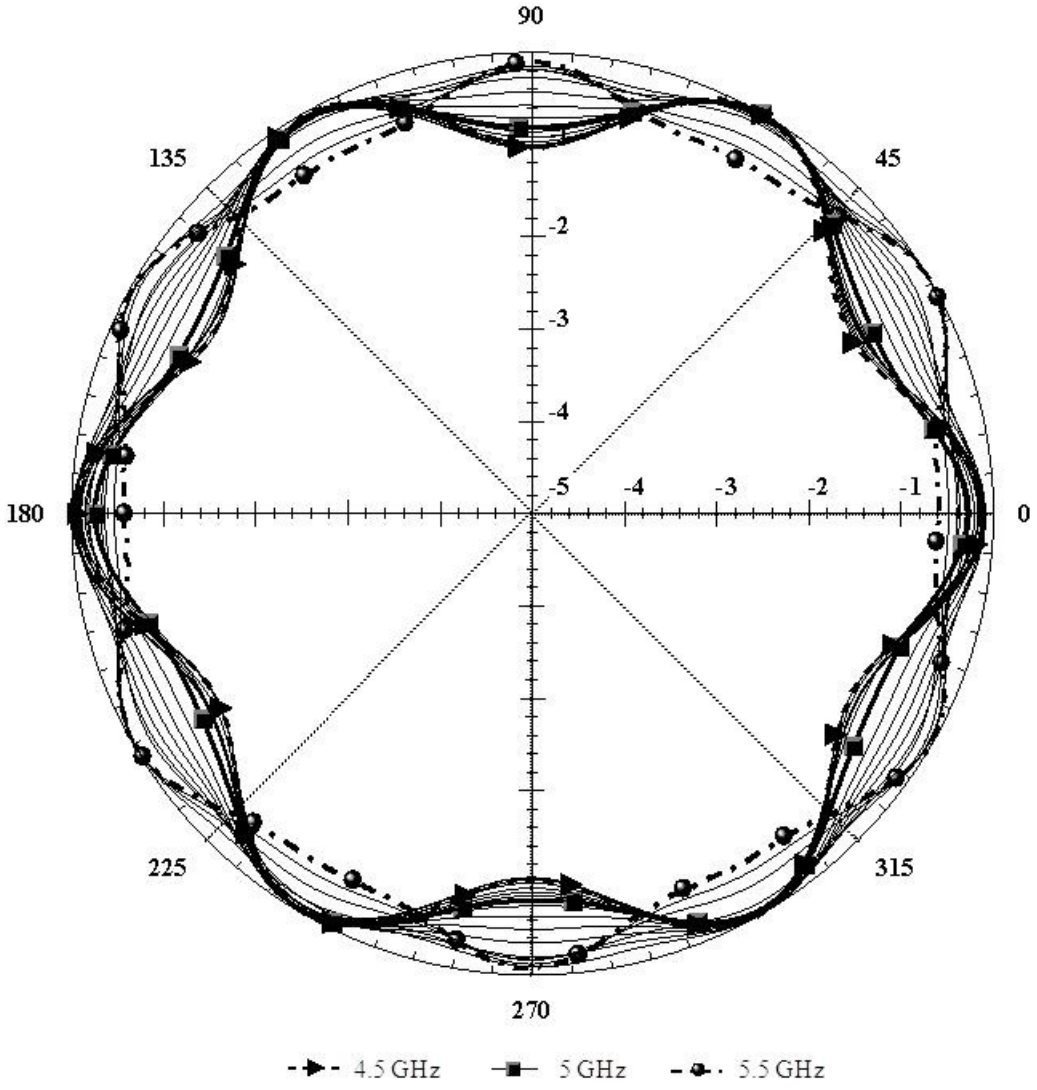

Figure 4.11 Omni-directional pattern (H-plane) for hexagonal structure of four-element sub-arrays over 4.5 GHz to 5.5 GHz frequency range.

4.2.2 The Effect of Using a Different Number of Sub-Arrays

Just as the number of elements in each sub-array impacts the directivity of the 3-D structure, it is equally important to examine the optimum number of sub-arrays that result in an omni-directional pattern. The use of four and eight sub-arrays (or square and octagonal configurations, respectively) was thus compared against the selected hexagonal configuration. HFSS simulation results for each approach are presented in Figure 4.12. It

can be seen that the square configuration produces a non-uniform radiation pattern at points 90° apart, with directivity at least 5 dB lower than the neighboring maxima. On the other hand, the more complex octagon design yields an almost identical pattern to the hexagon.

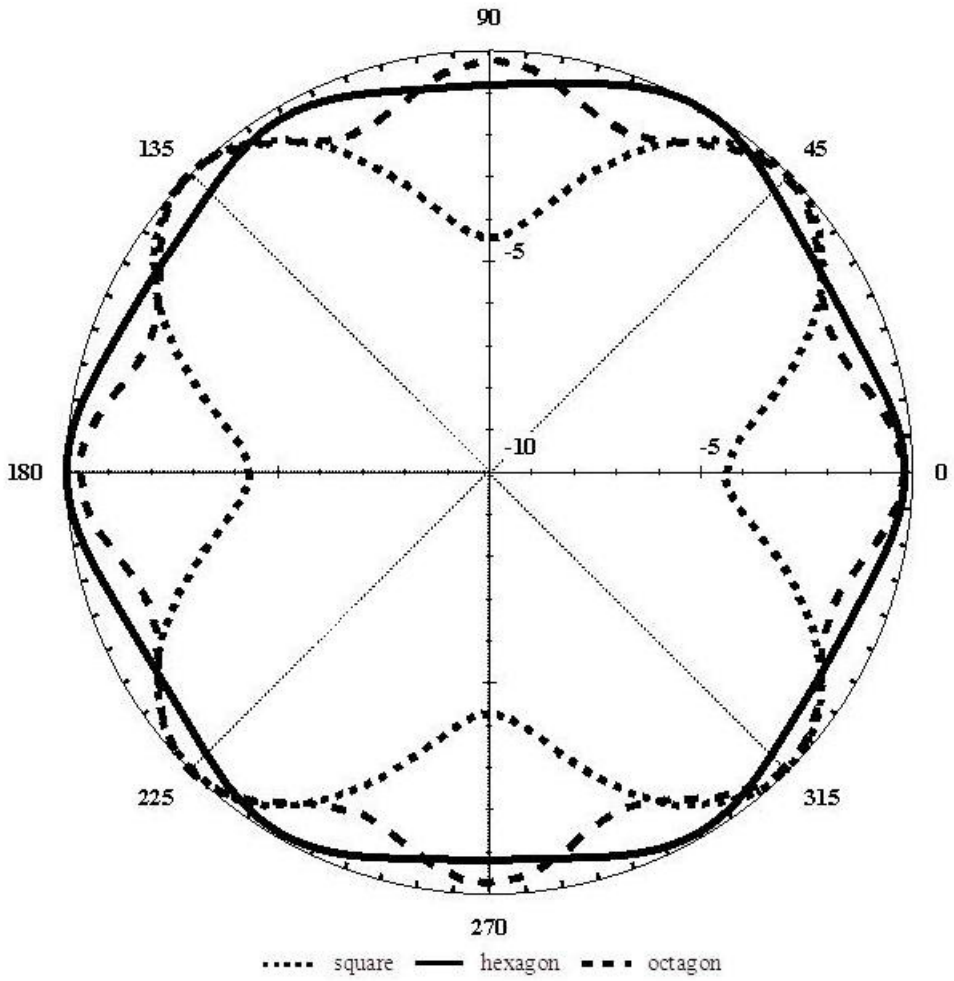

Figure 4.12 H-plane comparison between square, hexagonal and octagon configuration of four-element sub-arrays simulated at 5 GHz, and measured hexagonal four-element structure at 5 GHz.

4.2.3 Sectoral Radiation

Apart from uniform omni-directional coverage, the intent was to provide the ability for sectoral radiation as before mentioned. If an appropriate beam-forming

network is developed, and there is a need to communicate in a preferred direction(s), different numbers of sub-arrays of the hexagonal configuration could be used to achieve this goal. Figure 4.13 demonstrates this ability through a comparison between different numbers of sub-arrays used at one instance. In addition to the ability to reconfigure the omni-directional pattern into a more directional pattern (no back lobe) at specific azimuth angles, the increase in gain at those azimuth points is observed. Thus, sectoral radiation provides a means for achieving gain higher than that of the omni-directional radiator. The gain resulting from usage of two sub-arrays is more than double the gain of the omni-directional radiator (greater than the gain of the individual sub-array by ~1dB). If moderate increase in gain is desired spread over wider azimuthal portion, three sub-arrays could be used to increase the gain by 2-3 dB. Similarly, Figure 4.14 shows the outcome from using three out of six non-consecutive sub-arrays. While there are portions of the azimuth pattern that have slightly lower gain than the gain of the omni-directional radiator, the rest of the pattern has at least 6 dB of gain with 2 dB higher peaks. The effect of using different number of sub-arrays on the omni-directional coverage and its gain in Figures 4.13 and 4.14 serves to depict numerous preferences offered by ability to exploit sectoral radiation.

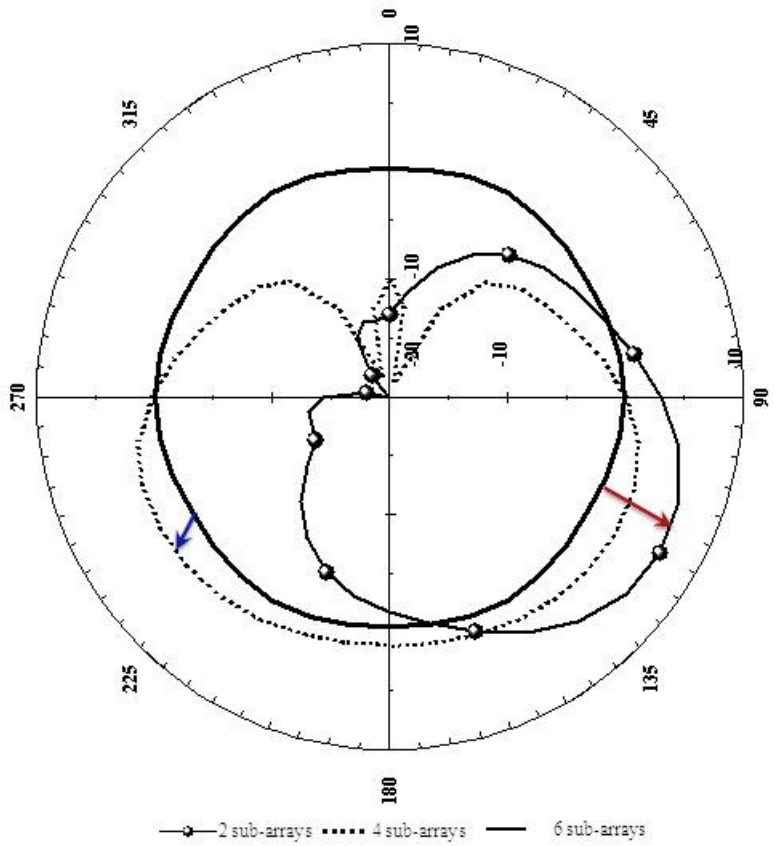

Figure 4.13 Simulation of azimuth plane comparison between 2, 4, and 6 arrays being used. Patterns resulting from two and four sub-arrays are normalized to the pattern of six sub-arrays (arrows shown signify increase in gain resulting from using different number of sub-arrays).

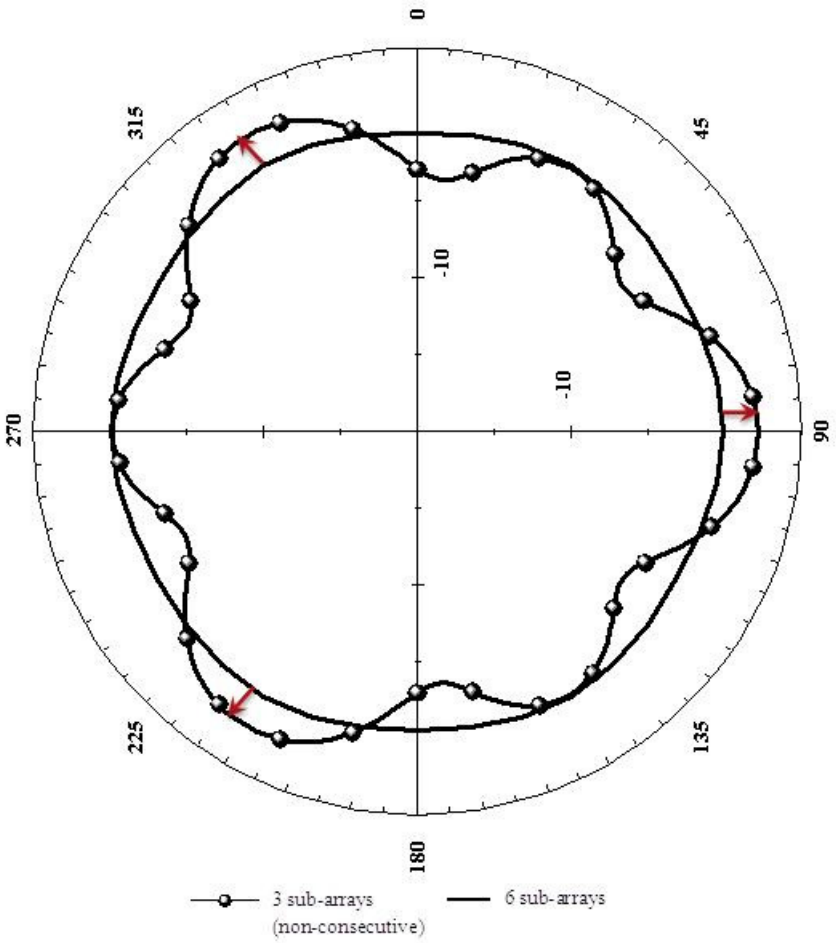

Figure 4.14 Simulation of azimuth plane comparison between pattern resulting from every second sub-array being used with that of the hexagonal configuration. The pattern of three non-consecutive sub-arrays is normalized to the pattern of hexagonal configuration (arrows shown signify increase in gain resulting from using different number of sub-arrays).

4.2.4 Feed Phase-Differential between Individual Sub-Arrays

In an alternative implementation of omni-directional radiator, the coupler in single-fed sub-arrays could be located externally in order to accommodate electronics for phase differentials between each half of the sub-arrays. This is analogous to using the dual-fed sub-array. Altering the phase of the input signal to each pair of elements can be used to reconfigure the azimuth and to some degree the elevation pattern. In the similar way to patterns resulting from two and three sub-arrays that were shown in Figures 4.13

and 4.14, using two sub-arrays, first and fourth, results at specific azimuth angles, in gain higher by ~2 dB compared to the gain resulting from using all six sub-arrays (Figure 4.15 and its 3-D polar plot). The first dual-fed sub-array in Figure 4.15 is fed 180 degrees out of phase with respect to the fourth dual-fed sub-array. In addition, distinct nulls (40 dB deep) in the pattern are created, which is often very desirable if incoming radiation needs to be jammed. The azimuth angle at which nulls occur can be changed to a certain degree if the patterns of the first and the fourth sub-array are tilted i.e. the 180˚ feed phase differential applied to the ends in each sub-array is altered.

Due to the ability to only change the phase between two pairs of elements in dual-fed four-element sub-array, rather than the phase to each individual element [72] as required for wider beam steering, the dual-fed configuration allows +/-25 degrees of vertical beam-steering over 3 dB reduction in directivity. Proper elevation beam steering with reduction of side-lobes would have to be achieved with the implementation of additional components into dual-fed array structures. However, +/-15˚ of vertical beam steering is achievable without suffering in gain (Figure 4.16), if appropriate phase differential is applied to each sub-array and sub-arrays with respect to each other. The phase differential in each sub-array of Figure 4.16 is 90˚, while the neighboring sub-arrays are advanced/lagged by 50˚. Results of Figure 4.16 are of course one feed phase-differential combination and many others, possibly with even greater vertical beam steering, can be used.

In an alternate feed-phase differential applied to dual-fed sub-arrays in the hexagonal configuration, the elevation pattern in Figure 4.16 could be tilted i.e. one side of the elevation pattern is steered up, while the other side of the elevation is steered

down. This could be achieved when, for example, an opposite feed-phase differential is applied to dual-fed sub-arrays in one half of the omni-directional radiator (3 sub-arrays) with respect to the other 3 sub-arrays.

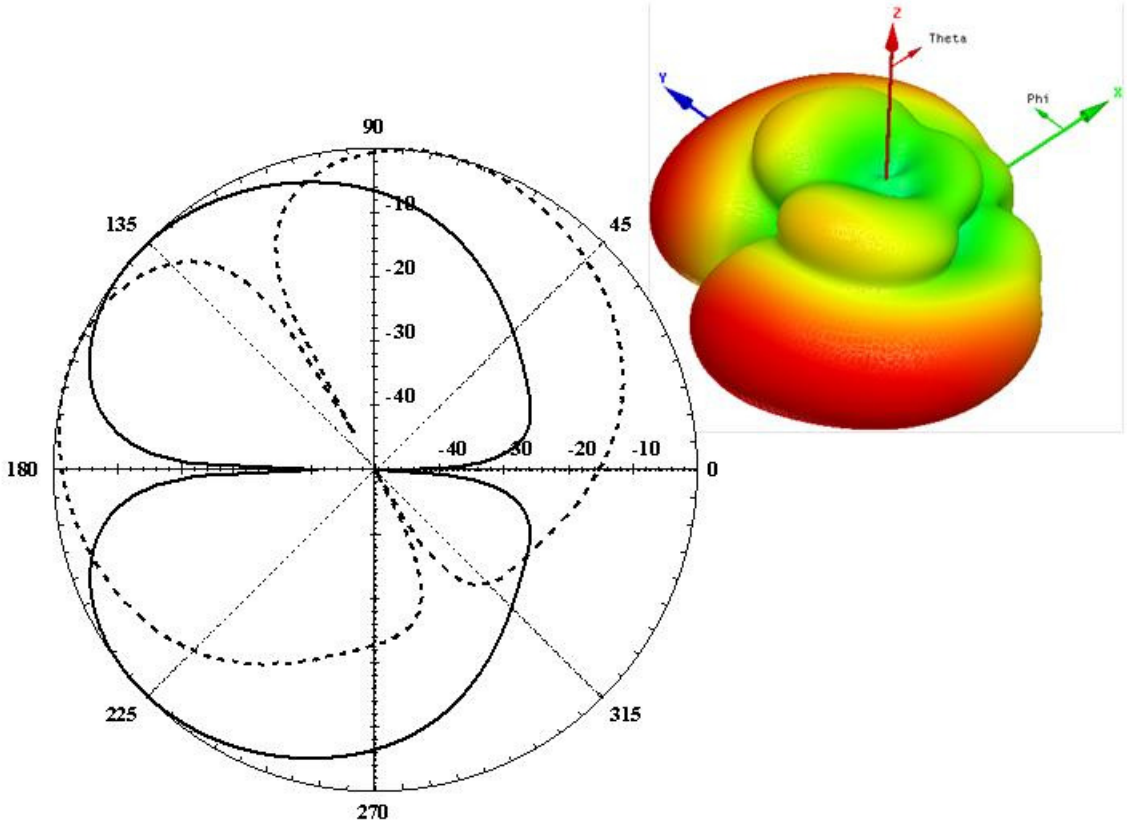

Figure 4.15 Creation of nulls at specific azimuth angles by using first and fourth sub-array fed with 180 degree out-of-phase signals. The phase at each end of the first dual-fed sub-array is 0˚ and 180˚, respectively, while the phase at each end of the fourth dual-fed sub-array is 180˚ and 0˚, respectively. 3-D plot of the resulting pattern (right).

Vertical beam-steering of the single sub-array is most limited by the inability to alter the phase of each antenna element in the sub-array. Nonetheless, a single sub-array feed phase differential of 100˚, Figure 4.17, can be steered in +/-10˚ in elevation without diminishing its gain, while the level of side lobes can be changed with proper adjustment of the amplitudes of the signals going into each end of the dual-fed sub-array.

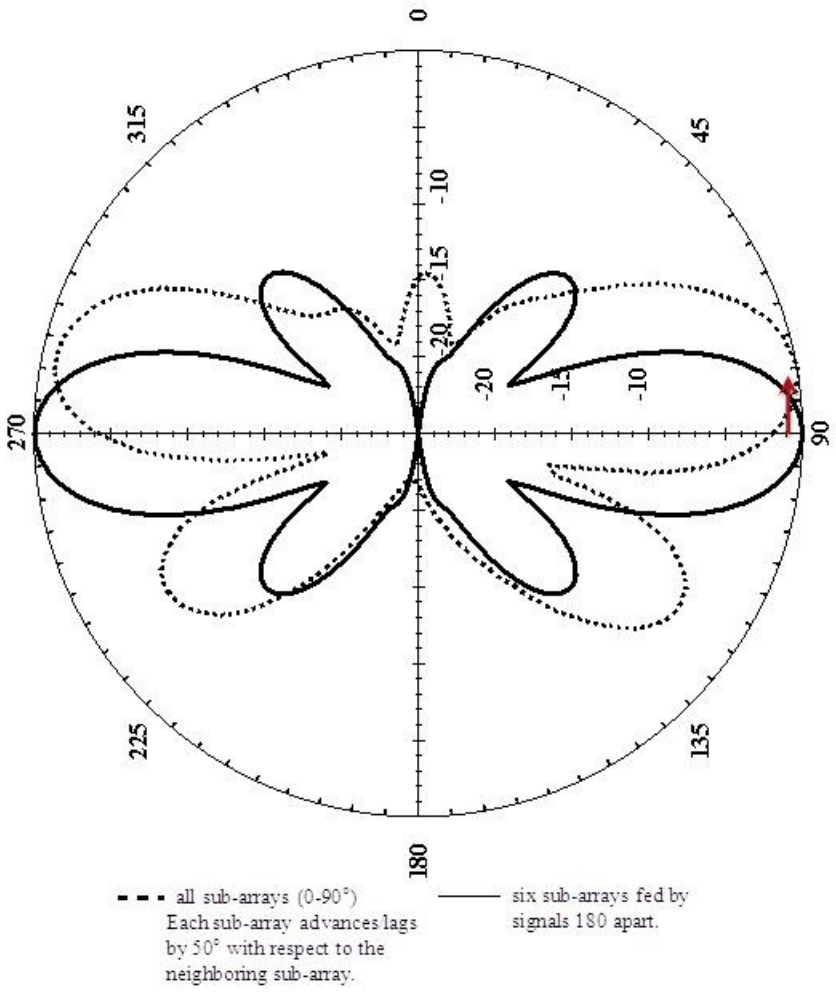

Figure 4.16 Comparison of elevation pattern (φ=0˚) between hexagonal configuration with sub-arrays being fed by different phase differential at the input in addition to each sub-array being advanced/lagged with respect to the neighboring sub-array (the arrow shown signifies tilting of the elevation pattern resulting from the change in feed phase differential).

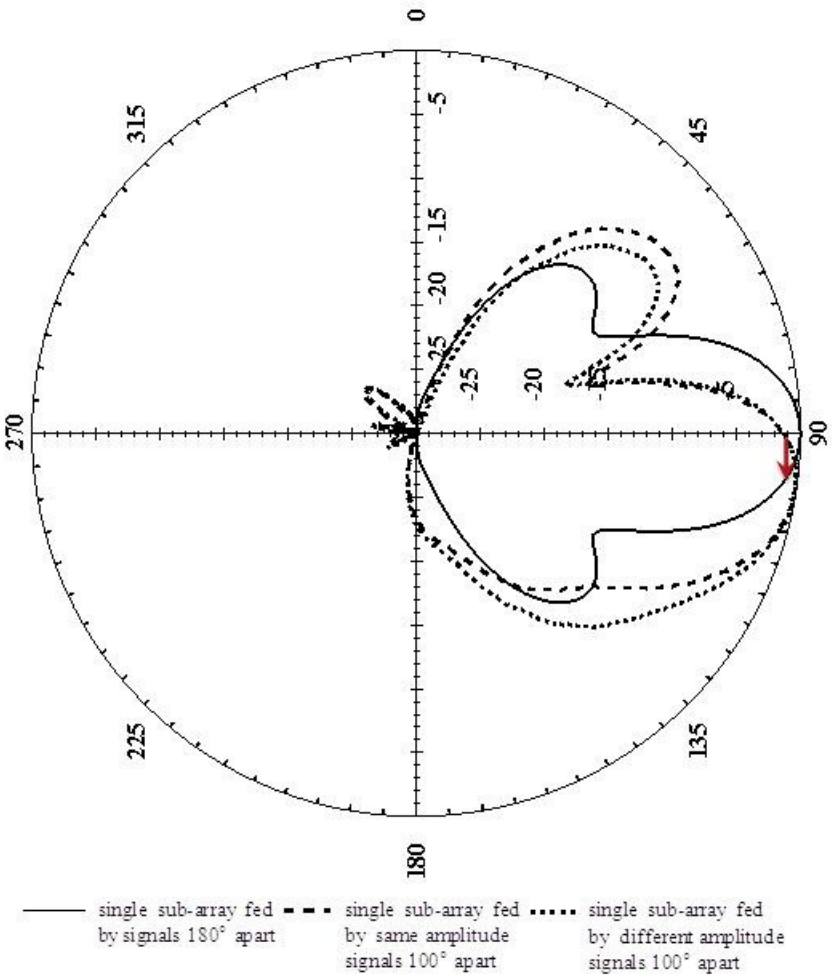

Figure 4.17 Single dual-fed sub-array with different phase/amplitude of the input signals (the arrow shown signifies tilting of the elevation pattern resulting from the change in feed phase differential).

4.2.5 The Array Pattern Analysis

Given the electrical size of the 3D structure, considerable computational resources are needed for simulation. The HFSS simulations of a sub-array and the complete hexagonal structure require 4 and 113 CPU hours, respectively, using AMD Opteron™ 8302 processors. Thus an efficient analysis that enables comparisons of sub-array designs with different geometrical parameters, e.g. substrate width or hexagon diameter, would significantly decrease the design cycle.

In consideration of efficient array design, the analysis of the omni-directional properties of the 3-D hexagonal structure was done utilizing linear array analysis [30]. The analysis was performed on three sub-arrays assuming that the middle (reference) sub-array is linearly displaced forward by *b* (Figure 4.18). These three sub-arrays form one half of a full hexagonal configuration and are centered on each of the three respective faces of a hexagon. In order to calculate the phase delay of the first and the third sub-array with respect to the second (middle) SA, three far-field observation regions were defined: Region I for $0^\circ < \varphi < 60^\circ$; Region II for $60^\circ < \varphi < 120^\circ$; and Region III for $120^\circ < \varphi < 180^\circ$. In Region I the phase lag of sub-array 1 with respect to sub-array 2 is denoted as $d_1(\varphi)$ in (4.1), while sub-array 3 is advanced by $d_3(\varphi)$, shown in (4.2). The phase progression/recession of sub-arrays 1 and 3 with respect to sub-array 2 for observation points in Regions II and III were determined in a similar manner.

$$d_1(\varphi) = -(d \cdot \cos(\varphi) + b \cdot \cos(90 - \varphi) \tag{4.1}$$

$$d_3(\varphi) = d \cdot \cos(\varphi) - b \cdot \cos(90 - \varphi) \tag{4.2}$$

The parameter *b* is equal to $a\sqrt{3}/4$, where *a* is the hexagon face width, while *d* is equal to $3a/4$ (see Figure 4.18).

In order to determine the array pattern for the three-SA configuration, the element pattern in (4.3) was first determined using the equations for a microstrip antenna based on a two-slot model found (Appendix A) in [30] that takes into account the effect of the ground plane and substrate. The element pattern for the reference sub-array (SA 2) is given as $EP_2(phi_2(\varphi))$, where $phi_2(\varphi) = \varphi$. The element patterns for the other two SAs, $EP_1(phi_1(\varphi))$ and $EP_3(phi_3(\varphi))$, were found in a similar manner, but the physical orientation of each element is taken into consideration, i.e. the first element is dependent

on $phi_1(\varphi)= \varphi-60^\circ$ and the third element is dependent on $phi_3(\varphi)= \varphi+60^\circ$, given their orientation around the hexagon. In (4.3) *width* refers to the width of each patch element (equivalent to *Width* in Table 3.1); height denotes the thickness of the antenna substrate (h_A given in Section 3.3), k is the wave number, and ε_r is the relative dielectric constant of the antenna substrate (ε_r=2.2).

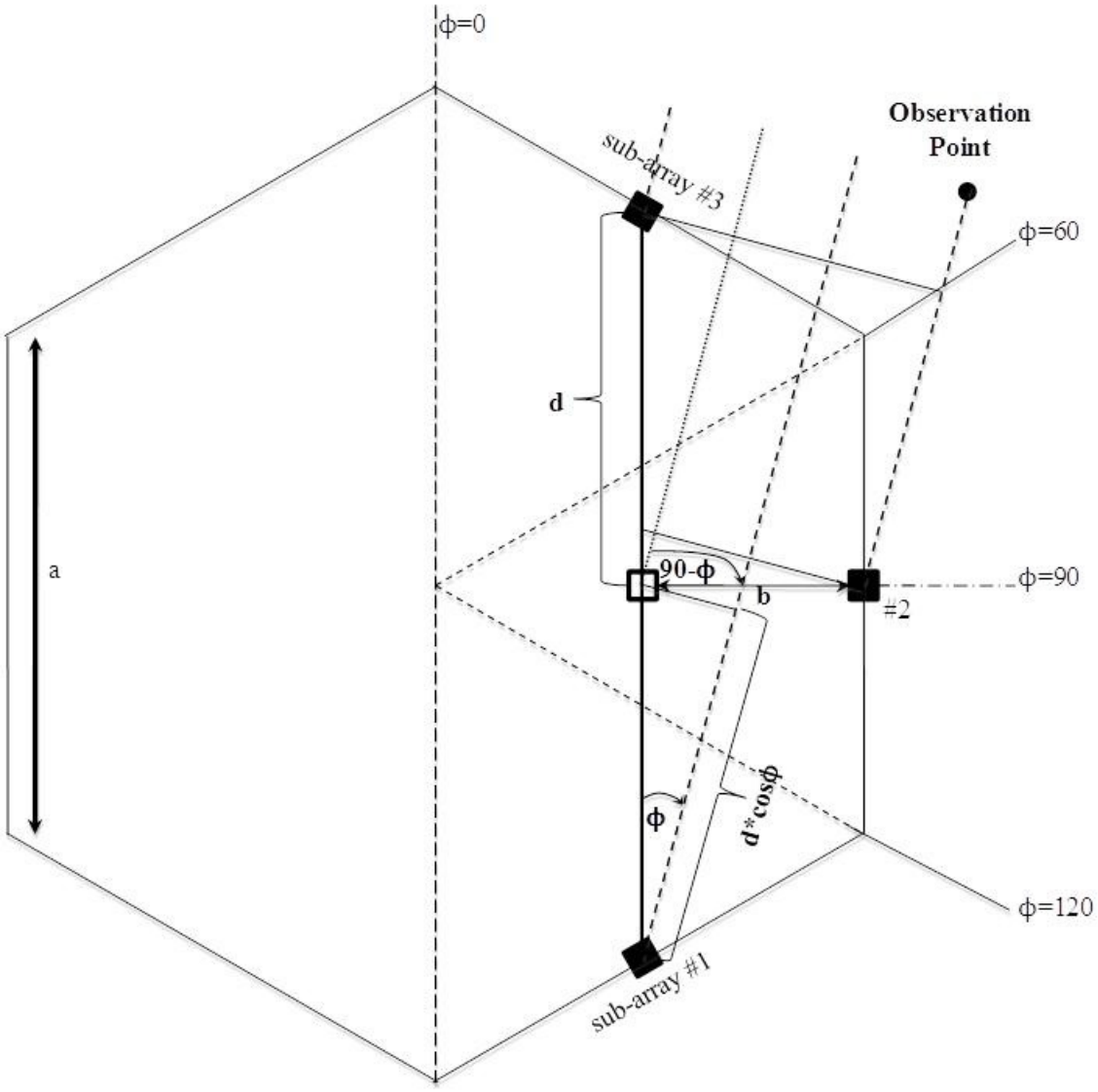

Figure 4.18 Linear array analysis with middle element as the reference element. The case for an observation point in the $60^\circ < \varphi < 120^\circ$ region is shown (top view of the hexagon).

$$EP_2(phi_2(\varphi)) = Fh(phi_2(\varphi)) \cdot F4(phi_2(\varphi)) \tag{4.3}$$

$$Fh(phi_2(\varphi)) = \sin c\left(\frac{k \cdot width \cdot \sin(\varphi - 90)}{2}\right) \cdot \cos(\varphi - 90)$$

and

$$F4(phi_2(\varphi)) = \frac{2 \cdot \cos(\varphi - 90)}{\cos(\varphi - 90) - j \cdot \sqrt{(\varepsilon_r - \sin(\varphi - 90)^2)}} \cdot \frac{1}{\cot\left[k \cdot height \cdot \sqrt{(\varepsilon_r - \sin(\varphi - 90)^2)}\right]} \tag{4.4}$$

The analysis of the omni-directional pattern characteristics of the hexagonal structure could be split into six identical regions, each 60 degrees wide. Within this region of interest only a single sub-array and two neighboring sub-arrays, one on each side, need to be considered. The other three sub-arrays are out-of-sight and do not have a significant contribution to the far-field pattern in this region. In other words, the full 360-degree pattern is fully characterized by juxtaposition of six 60-degree regions of the omni-directional pattern. Thus, to validate the array analysis, the array pattern in (4.5), AP(φ), was compared to the H-plane pattern of the three sub-arrays simulated in HFSS over the 60 degree azimuthal region of the center sub-array. The comparison, given in Figure 4.19, shows at most 0.5 dB difference over the 60 degree region between the pattern predicted by the analysis and the one simulated in HFSS; measurements and HFSS simulations of the full hexagon show that the contribution from the other three sub-arrays reduces the gain variation in φ from +/-1 dB, as shown in Figure 4.19, to +/- 0.5 dB. The impact of increasing the width of each sub-array on the omni-directional pattern of the hexagonal structure is also shown in Figure 4.19; doubling the width of the hexagon results in significant pattern variation across the 60˚ section.

$$AP(\varphi) = a_2 \cdot EP_2(phi_2(\varphi)) + a_1 \cdot EP_1(phi_1(\varphi)) + a_3 \cdot EP_3(phi_3(\varphi)) \tag{4.5}$$

where $a_2 = 1$, $a_1(\varphi) = e^{(j \cdot k \cdot d_1(\varphi))}$ and $a_3(\varphi) = \mathrm{e}^{(j \cdot k \cdot d_3(\varphi))}$.

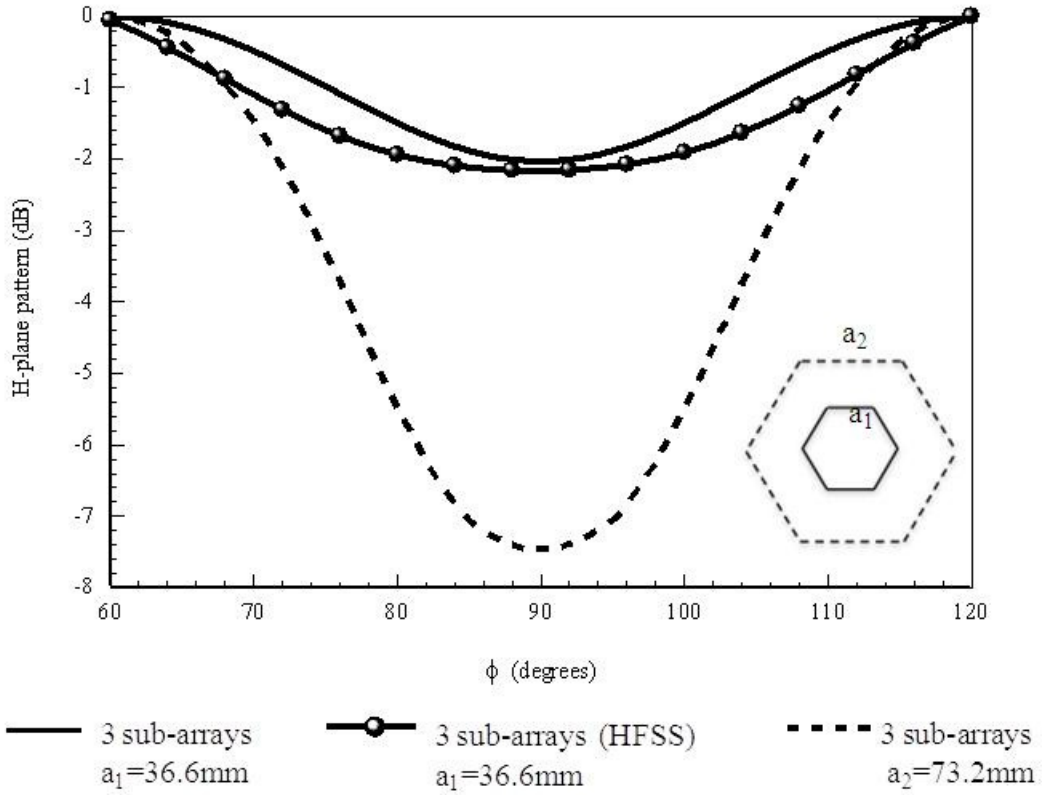

Figure 4.19 H-plane pattern for 3 sub-arrays for 60˚< φ <120˚ given by array analysis for different hexagon widths (a_1 and a_2) and the pattern simulated using HFSS for width a_1.

4.3 Conclusion

This chapter has presented the design and performance of a C-band omni-directional antenna comprised of six sub-arrays arranged in a hexagonal fashion. The elements used in the sub-arrays are slot-coupled microstrip antennas that are fed using microstrip lines on an opposing substrate. The height of the two prototype arrays is 115 mm, and their diameters 90 mm and 72.6 mm, respectively. The gain is ~6 dB with a 3-dB elevation beam width of ~30 degrees. The antenna also possesses good omni-directional coverage with a simulated azimuth gain variation less than +/- 0.5 dB over frequency, and measured variation of less than +/- 0.6 dB; the increase in the measured

gain variation is related to difficulties encountered in the assembly of the prototype design. Two advantages of this design are its constant beam angle over frequency, which is important for frequency-hopping applications, and the potential to add beam control to mitigate jamming in different sectors. It is also a low cost solution since all the components are fabricated using standard printed circuit board techniques. Gain, return loss, and pattern stability over frequency of the fabricated hexagonal structure were measured. In addition, linear array analysis of a semi-hexagonal structure was performed, allowing easier evaluation of similar array designs.

CHAPTER 5:

CIRCULARLY POLARIZED SINGLE-FED Z-SLOT APERTURE-COUPLED ANTENNA AND ARRAYS

5.1 Introduction

The ability of an antenna to communicate can be greatly diminished by environmental factors. Multipath interference is the consequence of various influences of the antenna's surroundings, such as signal reflections off of tall objects that arrive with a delay (out of phase) and degrade the performance of the communications link. Circular polarization is often utilized in an attempt to circumvent signal deterioration caused by multipath interference. In addition, the communication between a linear-polarized antenna and an antenna of opposite linear polarization results in a greatly reduced signal strength. An antenna that employs circular polarization provides the ability to communicate with antennas of either vertical or horizontal polarization, where half of its input power is allocated to each orthogonal component. However, obtaining a wide circular polarization bandwidth in microstrip antennas is a demanding task. The difficulty in achieving wide CP bandwidth is readily seen when considering that microstrip antennas already have inherently narrow impedance bandwidth. Moreover, realizing wide CP bandwidth in microstrip antennas via a single feed, without the use of external components such as couplers, to provide the required CP condition for orthogonal electric field components adds to the difficulty. The work presented in this chapter shows an approach to achieve at least 10% CP bandwidth in single-fed Z-slot aperture-coupled

microstrip antennas, which is almost double the bandwidth in comparison to what has been reported so far [49].

The following sections present the mechanism of operation of a Z-shaped aperture (Figure 5.1) to achieve wide CP bandwidth in single-fed aperture-coupled antennas. The approach obtains 10% impedance bandwidth and axial ratio below 3 dB over the entire C-band range with simulated directivity of 6.5 dB. Utilizing the series feed approach detailed in Chapter 3, two topologies of four-element CP aperture-coupled arrays are developed. Co-polarized and cross-polarized patterns, axial ratio and return loss for both single antenna and four-element arrays are shown.

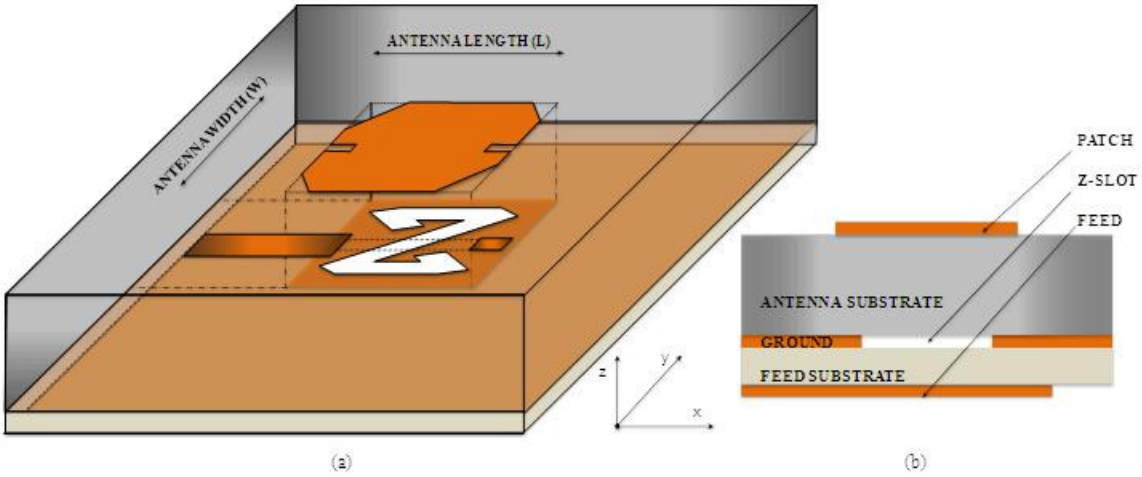

Figure 5.1 (a) Z-slot aperture-coupled microstrip antenna, (b) Cross-section.

5.2 Design of the Circularly Polarized Z-Slot Aperture-Coupled Antenna

A single-fed Z-slot aperture-coupled antenna is presented in Figure 5.1. As explained in Chapter 2, in order to excite circularly polarized waves, two equal amplitude, 90 degrees out of phase electric field components must be present. Among the methods to realize circular polarization in aperture-coupled antennas is an approach that

places a rectangular aperture along one of diagonals of the patch antenna element. However, the CP bandwidth realized with this approach, or similar implementations using a cross of two apertures along each diagonal, is rather narrow [50-51]. The tactic behind using a Z-shaped slot centered below the antenna element (Figure 5.2) can be explained by considering upper and lower halves of the Z-shape separately. In each half, two rectangular apertures, placed along each antenna diagonal, are spaced approximately 90 degrees apart. Both diagonally-oriented rectangular apertures induce electric field components along the width and the length of the antenna. The part of the aperture that runs horizontally in each half and is approximately 90 degrees long, is aimed to provide the required phase lag between electric field components induced by each diagonal aperture. The current runs along the perimeter of the Z-shaped slot and its circulation is enforced by both halves of the symmetric slot. In addition, the length of the Z-slot is approximately 360 degrees and assures that the field produced at each end of the Z shape adds in phase. Thus, the single aperture functions to provide both the equal amplitude electric field components and their required phase difference.

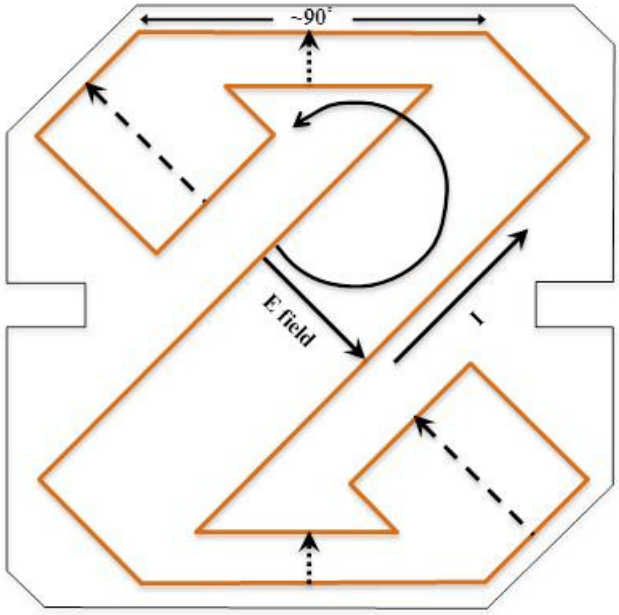

Figure 5.2 Illustration of the Z-slot aperture-coupling approach.

The patch antenna element further supports circular polarization by its perturbation segments located at each of its corners. The Z-slot aperture-coupled antenna presented herein is right-hand circularly polarized. The antenna element is a square measuring ~0.35λ at 5 GHz along each side (guided λ at 5 GH is~43 mm, ε_r=2.2 and h_A=3.17 mm). The slits in the antenna element along its width serve to slightly decrease the resonant frequency by increasing the current path length and are used to adjust the impedance of the antenna element. Detailed characteristics of the antenna element and the Z-slot are provided in Figure 5.3 and Tables 5.1 and 5.2. Proper adjustments of the width and the length of each part of the Z-slot, the antenna element and its perturbation segments, are required in order to optimize the CP bandwidth.

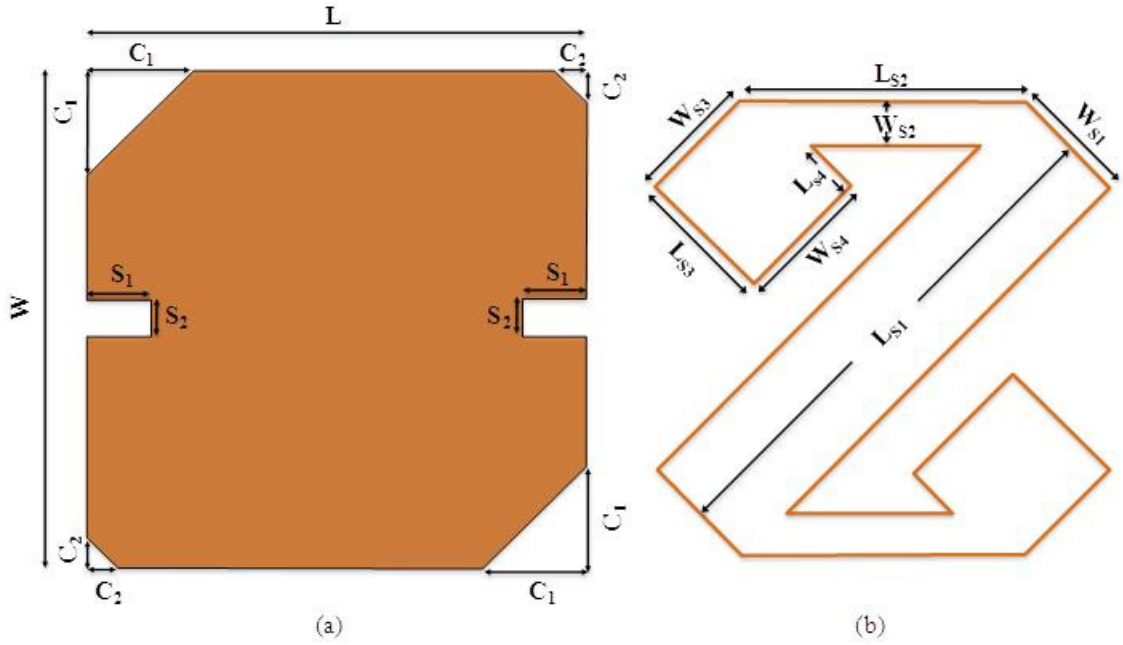

Figure 5.3 Characteristics of (a) the perturbed CP patch microstrip antenna, (b) the coupling Z-slot in the ground.

Table 5.1 Single Z-slot aperture-coupled CP antenna characteristics.

Patch Model (ADS Momentum/HFSS)	Size (mm)
Width (W)	15
Length (L)	15
Cutout 1 (C_1)	3.25
Cutout 2 (C_2)	1
Slit 1 (S_1)	2
Slit 2 (S_2)	1

Patch Model (ADS Schematic)	Value
R	565 Ω
C	0.009 pF
L_1	113.8 nH
L_2	3.84 nH
Tuning stub (T.S.)	1.69 mm

Table 5.2 Z-slot characteristics.

Length	Size (mm)	Width	Size (mm)
L_{S1}	15.3	W_{S1}	4
L_{S2}	8	W_{S2}	1.5
L_{S3}	4	W_{S3}	4.2
L_{S4}	1.68	W_{S4}	4.4

A Z-slot aperture-coupled antenna was designed in HFSS and matched to 50 ohms. Its characteristics, without the input matching network, were subsequently created

in Momentum in order to get a circuit representation of the antenna. The circuit model used to represent the antenna was the same as single element model presented in Chapter 3 (Figure 3.3). The comparison of results between the ADS circuit model and the Momentum representation of the antenna without the input matching network is given in Figure 5.4; it is seen that the S_{11} of the ADS circuit model of the antenna matches well to its Momentum representation within the targeted band of interest from 4.75 GHz to 5.25 GHz with a center frequency at 5 GHz. The value of S_{11} shown in the Figure 5.4 corresponds to an input impedance for the antenna of approximately 25 ohms. In the following sections, the circuit representation of the Z-slot model will be further used to develop four-element CP arrays.

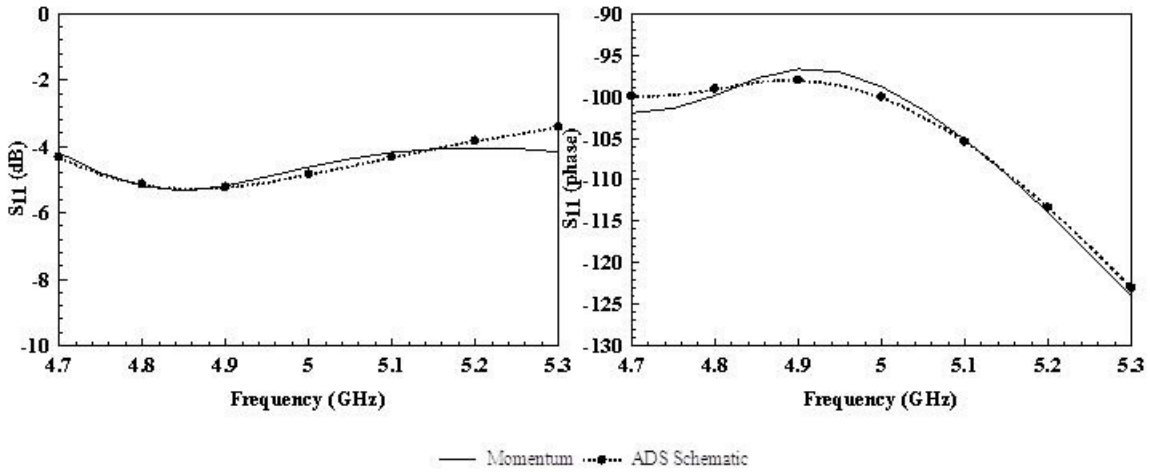

Figure 5.4 Single element Momentum results vs. the equivalent circuit model.

It is important to observe that the feed line beneath the antenna element (Figure 5.5) and part of the Z-slot through which the feed line passes are not orthogonal to each other. The angle between the feed line and the Z-slot influences the amount of coupling and the input impedance of the antenna [23]. This is in accordance to results obtained for the input impedance of 25 ohms. An input matching network was thus designed in HFSS

to match the antenna to the input impedance of 50 ohms (Figure 5.5). The details of the input matching network, substrate width and length are provided in Table 5.3.

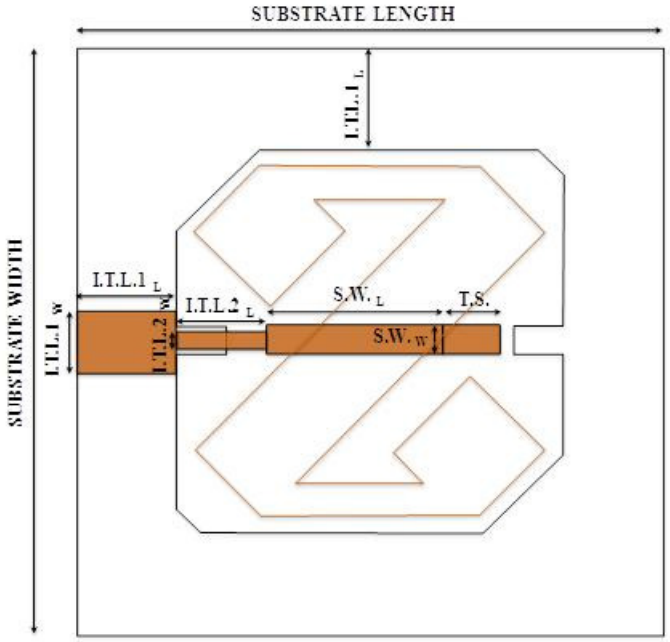

Figure 5.5 Single Z-slot aperture-coupled antenna characteristics.

Table 5.3 Z-slot aperture-coupled patch input matching network characteristics.

Single Patch Input Matching Network	Size (mm)
Substrate length	25
Substrate width	25
Slot feedline length ($S.F._L$)	6.83
Slot feedline width ($S.F._W$)	1
Tuning stub (T.S.)	2.58
Input T.L.1 length ($I.T.L.1_L$)	5
Input T.L.1 width ($I.T.L.1_W$)	3
Input T.L.2 length ($I.T.L.2_L$)	3.5
Input T.L.2 width ($I.T.L.2_W$)	0.6

The drawback of the current antenna architecture utilizing the Z-slot to achieve wide CP bandwidth lies in the size of the Z-slot relative to the patch antenna element. The large length of the slot increases the coupling of the aperture to the antenna, but also

allows for greater back radiation. Figure 5.6 shows this effect as it compares simulated (HFSS) and measured co- and cross-polarized patterns of the Z-slot aperture-coupled antenna at 5 GHz. The back lobe of pattern shown in Figure 5.6 is approximately 8 dB lower than the main lobe. The measured co- and cross- polarized patterns shown in Figure 5.6 agree well for angles close to broadside, and maintain the axial ratio value at 5 GHz for +/- 19 degrees in the E-plane.

The proposed Z-slot aperture-coupled antenna offers a great number of parameters, namely the width and length of sections of the Z-slot, the amount trimmed off of the corners of the antenna, the substrate width and length surrounding the antenna and the feed line running below the patch, that could be used to optimize axial ratio, S_{11} and directivity of the antenna. Simulation results of these antenna parameters so far have suggested that further optimization of the size of the patch antenna element and adequately proportioned Z-slot could, if not alleviate, then greatly reduce back radiation. The simulated directivity of the Z-slot aperture-coupled antenna element was 6.5 dB.

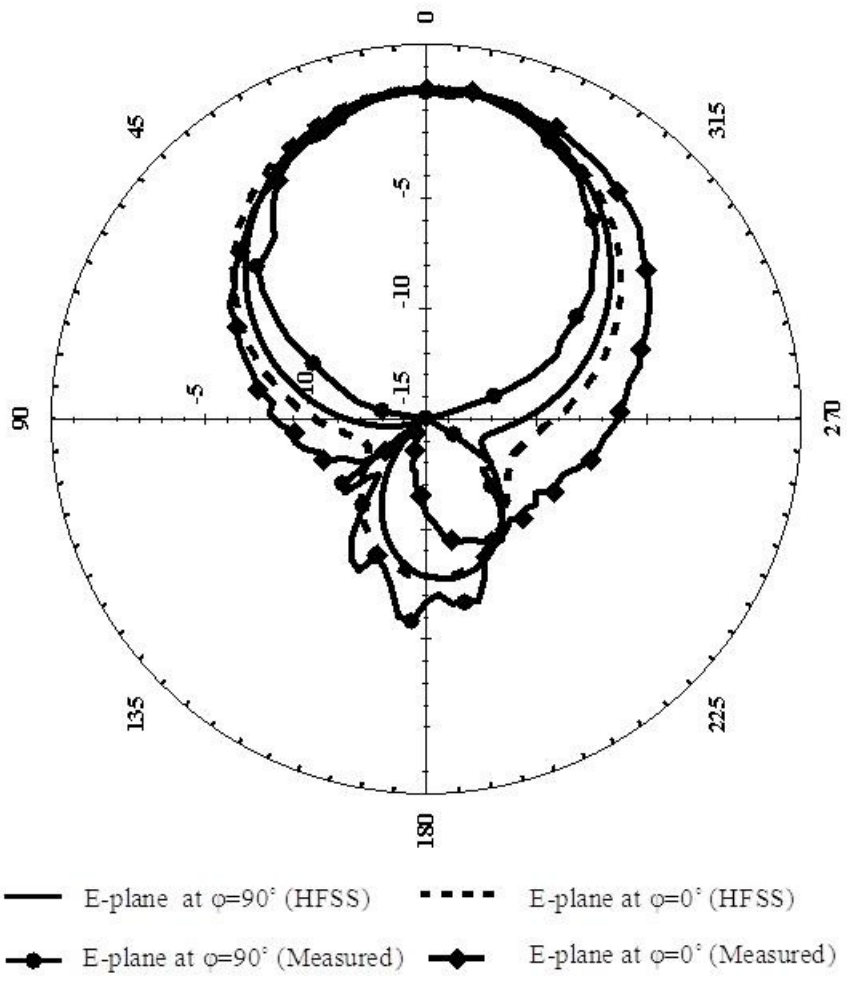

Figure 5.6 Simulated (HFSS) versus measured co- and cross-polarized E-plane patterns of the Z-slot aperture-coupled antenna at 5 GHz.

The Z-slot aperture-coupled antenna has at least 600 MHz of impedance bandwidth. Figure 5.7 shows the comparison between simulated and measured results for S_{11}. In designing the antenna, the aim was to keep the impedance and CP bandwidths as close as possible such that the CP operation could be utilized over the entire operational frequency range of the antenna. Simulated and measured results of the axial ratio are presented in Figure 5.8. The axial ratio was measured by taking the data for the co- and cross- polarized patterns of the Z-slot aperture-coupled antenna with respect to a

reference, linear-polarized antenna positioned at 0 degrees for the co- and 90 degrees for cross- polarized pattern. The simulated results show that the axial ratio better than 3 dB is realized across ~500 MHz, while the measured results show slightly lower bandwidth with values at each end of frequency range of 3.3 dB at 4.7 GHz and 3.4 dB at 5.25 GHz. The frequency shift observed in measured axial ratio can most likely be attributed to manual assembly and alignment the antenna. In addition, the simulated results of S_{11} indicate that its center frequency is at 4.8 GHz, while the axial ratio is centered at 5 GHz.

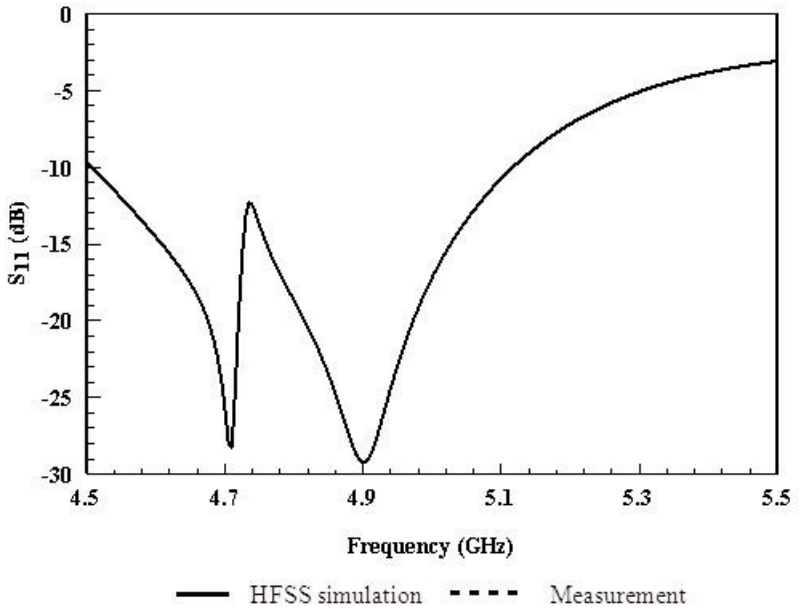

Figure 5.7 S_{11} for the single Z-slot aperture-coupled patch antenna.

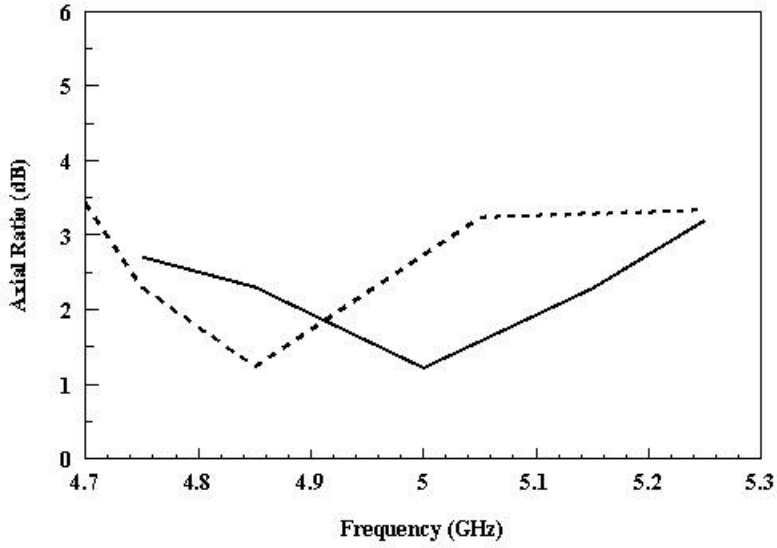

Figure 5.8 Axial ratio over frequency for single patch Z-slot aperture-coupled antenna.

5.3 Four-Element Circularly Polarized Z-Slot Aperture-Coupled Antenna Arrays

Two four-element Z-slot aperture-coupled CP array architectures were developed using a single Z-slot aperture-coupled patch antenna detailed in the previous section. Both topologies employ series-fed approach explained in Chapter 3 in each pair of its elements. In addition, elevation beam stability for these arrays is achieved by feeding the pair of elements via meandered 180-degree Rat-Race coupler developed and described in the following section. Two presented arrays have different element and pair spacing between antenna elements in each pair and two pairs of elements in the array, respectively. Thus, the effect of the overall size of the array on axial ratio, co- and cross-polarized patterns is presented.

5.3.1 Meandered 180-degree Equal Power Split Hybrid Rat-Race Coupler Design

The size of the Z-slot aperture-coupled antenna presented in this chapter is smaller when compared to the single antenna element used to develop N-element linearly polarized arrays described in Chapter 3. Development of four-element CP arrays using a

single Z-slot aperture-coupled antenna element is presented in the following section. As the series feed approach requires that two halves of each array be fed 180 degree out of phase, the size of the Rat-Race coupler used in linearly polarized arrays would constrict the spacing between each pair of antenna elements to a certain value. Moreover, its size does not allow for the pairs to be fed from the center of the array and reduce the unnecessary loss introduced in longer output lines. Meandering of the two output lines was also necessary in order to maintain 180 degree difference at the inputs to each half of the array as it was not symmetric about the center of the array. Therefore, a much smaller, symmetric 180 degree Rat-Race coupler was developed as shown in Figure 5.9 and its detailed characteristics are given in Table 5.4. The topology of the new Rat-Race coupler allows for easy reconfiguration of its width and length to suit the pair spacing that results in optimum directivity and axial ratio of the array. Figure 5.10 shows equal 3 dB split between two output ports (ports 2 and 3 in Figure 5.9) and S_{11} at the input port better than -20 dB from 4.5 to 5.5 GHz.

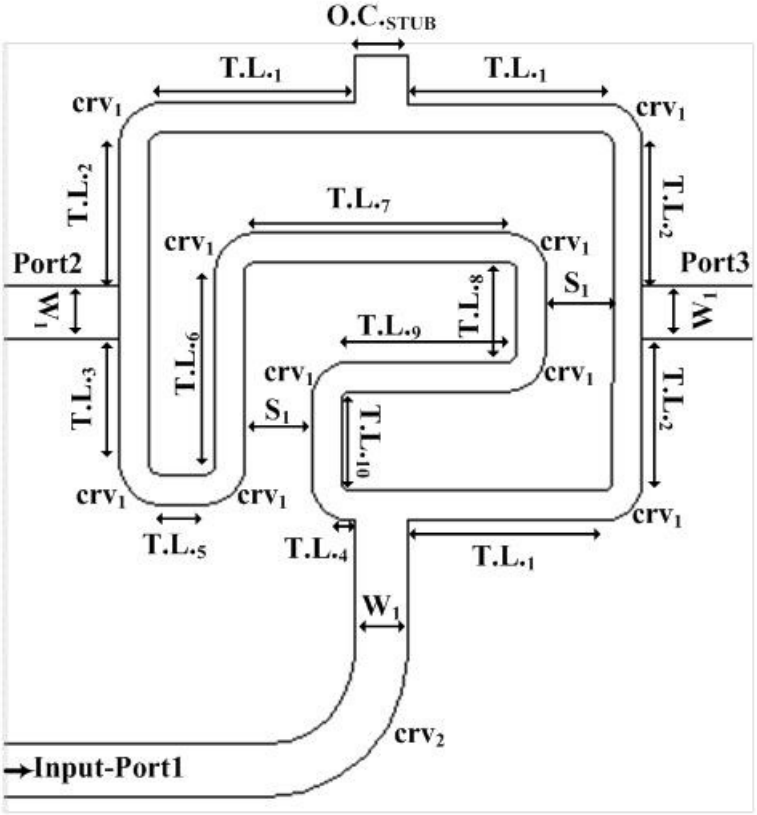

Figure 5.9 Rat-Race coupler in four-element CP sub-arrays.

Table 5.4 Rat-Race coupler characteristics.

	Length (mm)		Length (mm)	Width (mm)
T.L. 1	4.25	T.L. 6	4.17	W
T.L. 2	3.08	T.L. 7	5.48	W
T.L. 3	2.73	T.L.8	1.71	W
T.L.4	0.05	T.L.9	3.38	W
T.L.5	1	T.L.10	1.71	W
W	0.645	O.C.STUB	1.03	W_1
W_1	1.1	S_1	1.455	
	Radius (mm)		Width (mm)	
crv_1	0.55		W	
crv_2	2.5		W_1	

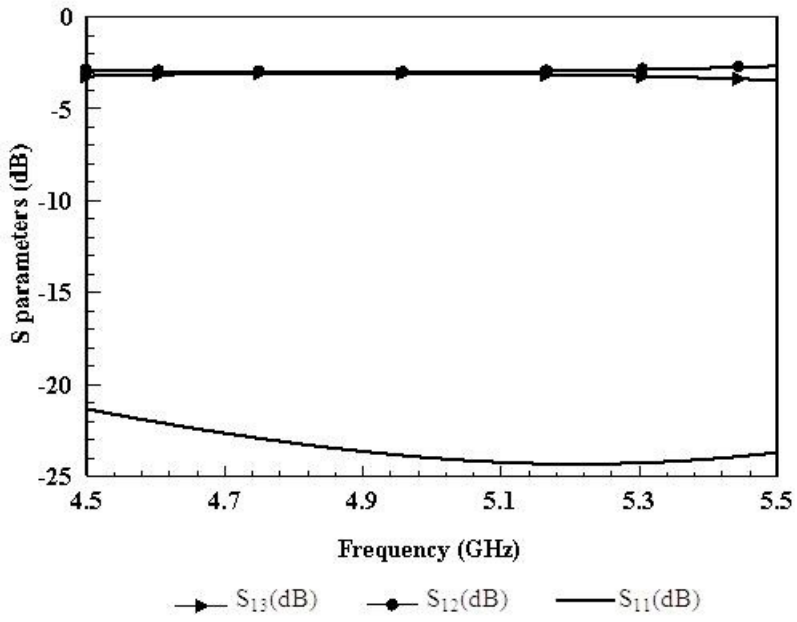

Figure 5.10 Simulated results (Momentum) of the meandered Rat-Race coupler used in four-element CP arrays.

5.3.2 Four-Element Z-Slot Aperture-Coupled Meandered CP Array

A single Z-slot aperture-coupled antenna was used to develop a meandered circular polarized four-element array (Figure 5.11). The four-element array uses a hybrid 180 degree Rat-Race coupler explained in the previous section to maintain its pattern at broadside. The transmission lines in between antenna elements in each pair of the array were meandered to allow easy reconfiguration of this array. The meandered sections allow for adjustment of element spacing for directivity and axial ratio optimization. Characteristics of the array are provided in Table 5.5, while the optimized dimensions of the patch element and the corresponding Z-slot are given in Table 5.6.

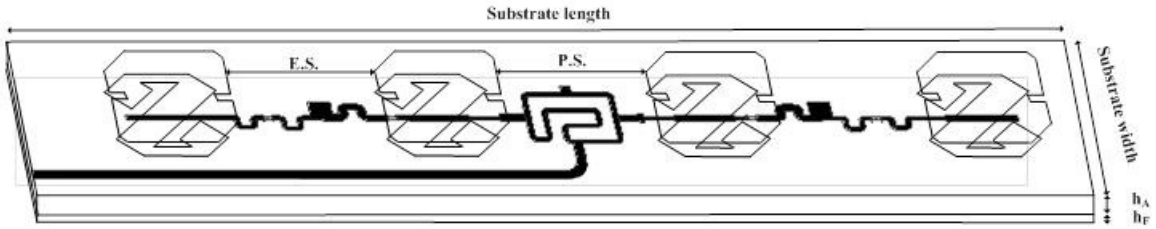

Figure 5.11 Illustration of the four-element CP array.

Table 5.5 Four-element meandered CP array characteristics.

Array Element	Size (mm)
Substrate length	136.5
Substrate width	37.2
Antenna substrate height (h_A)	3.17
Feed substrate height (h_F)	0.51
Element spacing (E.S.)	18.25
Pair spacing (P.S.)	18.5

Table 5.6 Four-element meandered CP array. (a) Details of the antenna element. (b) Z-slot dimensions.

Patch Model (HFSS)	Size (mm)
Width (W)	15.2
Length (L)	15.25
Cutout 1 (C_1)	2.75
Cutout 2 (C_2)	1.1
Slit 1 (S_1)	2
Slit 2 (S_2)	1

Length	Size (mm)	Width	Size (mm)
L_{S1}	4	W_{S1}	15.1
L_{S2}	7.85	W_{S2}	1.5
L_{S3}	3.9	W_{S3}	4.2
L_{S4}	1.58	W_{S4}	4.4

The matching network used in each pair of elements in the meandered four-element array is shown in Figure 5.12, along with the circuit representation of the antenna element and matching network used in ADS. The matching network consists of the meandered section in between two antenna elements and the input matching network that is used to match the impedance of a pair of elements to 50 ohms. The meandered section of the matching network employs a series combination of an inductor, a capacitor, an

open circuited stub and transmission lines in between. Subsequently, the four-element array and the matching network were optimized in HFSS and the details of its dimensions are given in Table 5.7.

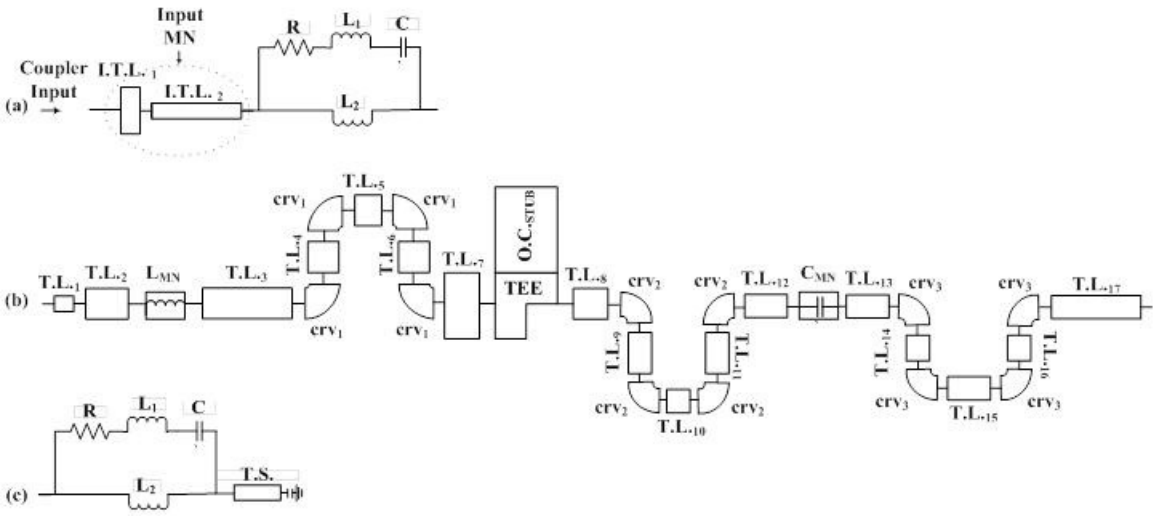

Figure 5.12 Meandered matching network in each half of the four-element CP array. (a) Input matching network and single element model for the middle patch elements. (b) Matching network between two patch elements. (c) Single element model for the patches at each end of the array.

Table 5.7 Characteristics of the matching network for the meandered four element CP array.

	Length (mm)	Width (mm)		Length (mm)	Width (mm)
$I.T.L._1$	0.64	1.43	$I.T.L._2$	3.88	0.6
$T.L._1$	0.44	0.6	$T.L._9$	0.9	0.6
$T.L._2$	0.98	0.67	$T.L._{10}$	1	0.6
$T.L._3$	2.37	1.09	$T.L._{11}$	0.9	0.6
$T.L._4$	0.67	1.09	$T.L._{12}$	0.75	0.6
$T.L._5$	1	1.09	$T.L._{13}$	0.75	0.69
$T.L._6$	0.67	1.09	$T.L._{14}$	0.99	0.69
$T.L._7$	2.11	1.09	$T.L._{15}$	1	0.69
$T.L._8$	1	0.6	$T.L._{16}$	0.99	0.69
			$T.L._{17}$	4.32	0.69
$O.C._{STUB}$			T.S.	1.48	1
	Radius (mm)		Width (mm)		
crv_1	0.62		1.09		
crv_2	0.5		0.6		
crv3	0.5		0.69		

The simulated axial ratio of the meandered four-element CP-array is shown in Figure 5.13. The axial ratio was optimized for operation from 4.75 GHz to 5.25 GHz with the center frequency at 5 GHz. The axial ratio at 4.75 GHz is 4.4 dB, while its value at 5.25 GHz is 4.95 dB. The axial ratio is 2.5 dB at 5 GHz and maintains the value below 3 dB from 4.84 GHz to 5.09 GHz, corresponding to 5% CP bandwidth at 5 GHz.

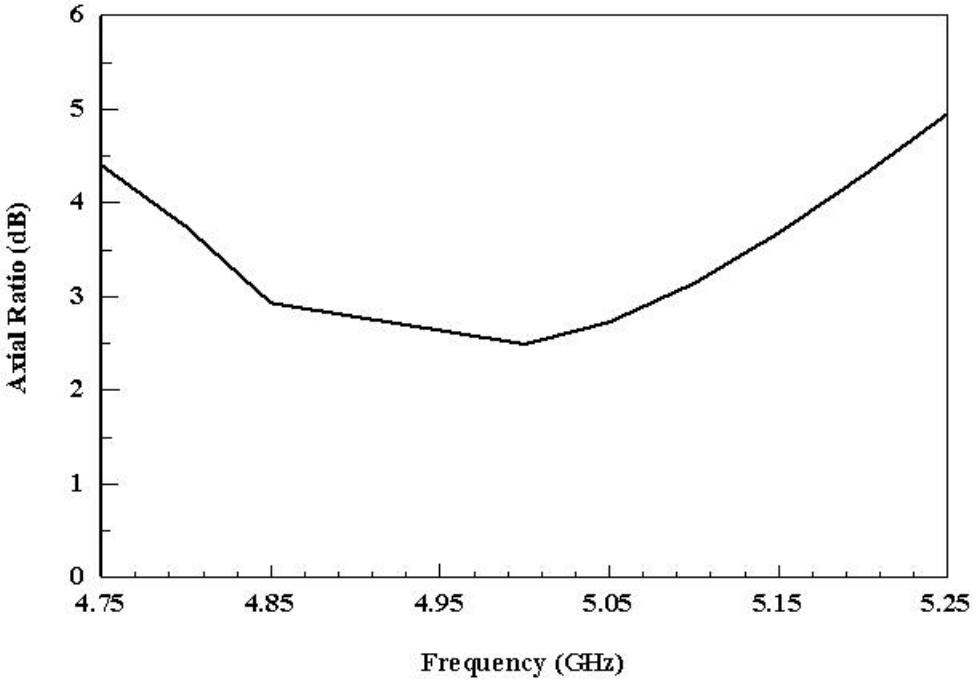

Figure 5.13 Axial ratio over frequency for the four-element CP Z-slot aperture-coupled array.

The S_{11} of the meandered four-element CP array is shown in Figure 5.14. The array has a bandwidth of ~620 MHz, from 4.45 GHz to 5.07 GHz, and its center frequency is somewhat shifted from the center frequency of the circular polarization bandwidth, but it is below 10 dB over the entire CP bandwidth range.

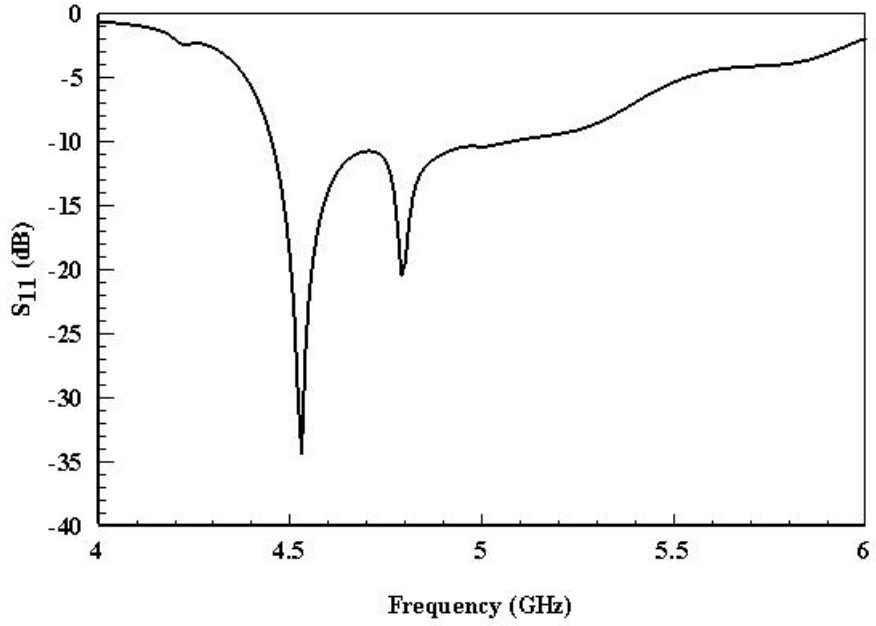

Figure 5.14 S_{11} of the four-element Z-slot aperture-coupled CP array.

The comparison of two orthogonal E-plane patterns, at φ=90˚ and φ=0, is shown in Figure 5.15. It can be seen that both E-plane patterns compare well for angles close to broadside, or +/- 19 degrees. The measured directivity of the meandered four-element CP array is ~12.1 dB. The isolation between right-hand (RHCP) and left-hand (LHCP) circular polarization is shown in view of LHCP circular polarization ratio in Figure 5.16 that represents the difference between gains of these two polarizations. It is shown that LHCP polarization ratio is ~ -17 dB at 5 GHz and is below -11.5 dB from 4.75 GHz to 5.25 GHz.

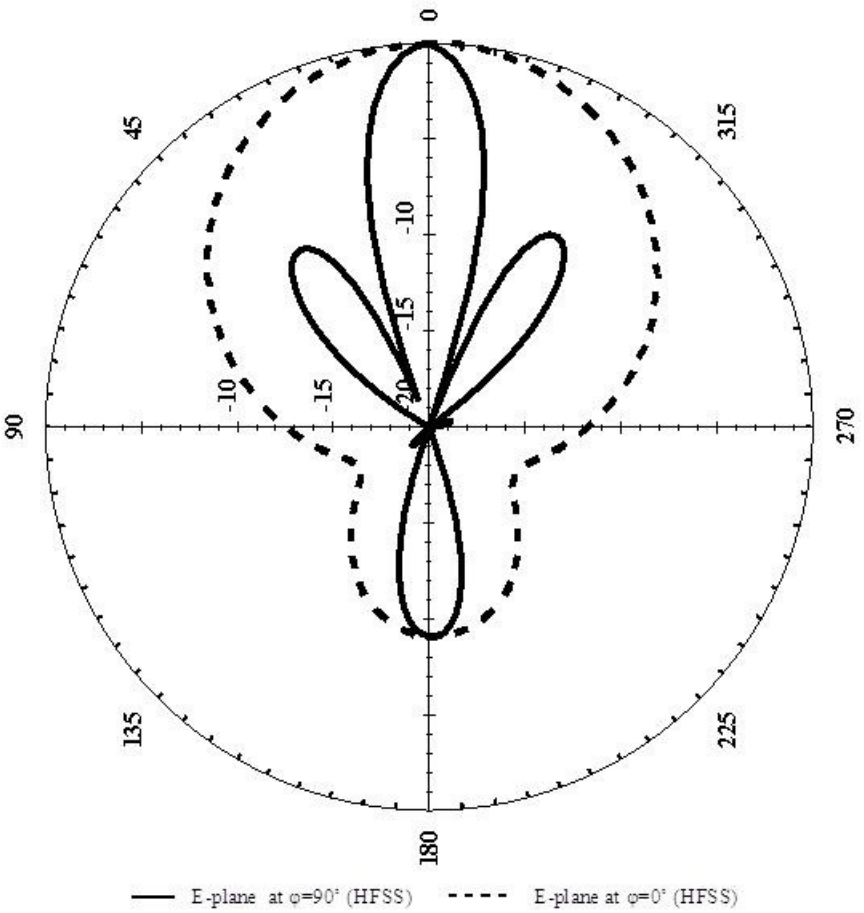

Figure 5.15 Comparison of E-plane patterns at φ=90˚ and φ=0˚ for the four-element Z-slot aperture-coupled CP array.

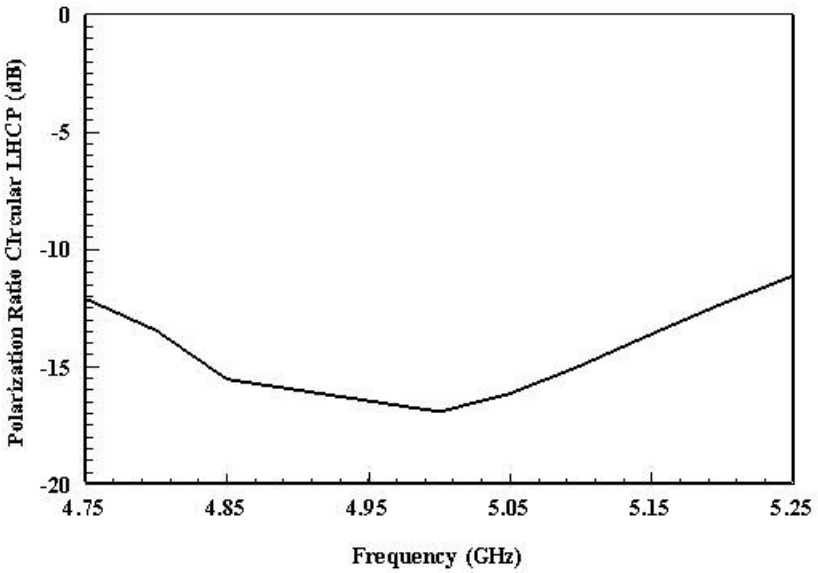

Figure 5.16 Simulated (HFSS) LHCP polarization ratio of the meandered four-element CP array.

5.3.3 Four-Element Z-Slot Aperture-Coupled CP Array

Following the development of the meandered four-element CP array, an alternative architecture of the array was designed (Figure 5.17). In comparison to the meandered array described in the previous section, the matching network in this array was not meandered to examine the effect of increasing the element spacing on directivity and axial ratio. The dimensions of the second generation four-element CP array are given in Tables 5.8 and 5.9 (a) and (b). The matching network used in this topology and its ADS circuit representation are given in Figure 5.18. This array also uses the series-feed approach from Chapter 3, and a single element Z-slot aperture-coupled antenna model. Characteristics of the matching network used in this array are provided in Table 5.10.

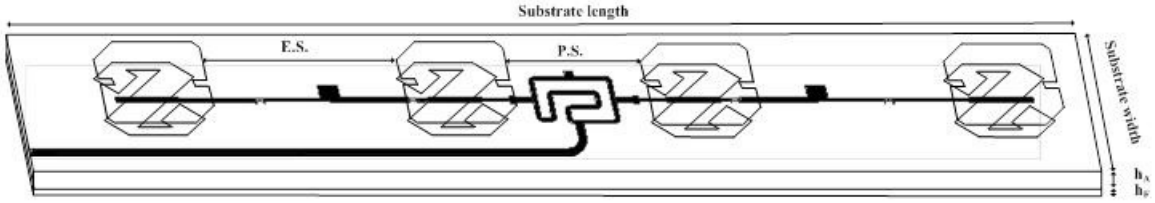

Figure 5.17 Illustration of the four-element CP array.

Table 5.8 Four-element CP array characteristics.

Array Element	Size (mm)
Substrate length	151.9
Substrate width	31.2
Antenna substrate height (h_A)	3.17
Feed substrate height (h_F)	0.51
Element spacing (E.S.)	26.45
Pair spacing (P.S.)	22.5

Table 5.9 (a) Characteristics of the antenna element, (b) Characteristics of the Z-slot in the four-element CP array.

(a)

Patch Model (HFSS)	Size (mm)
Width (W)	15.2
Length (L)	15.25
Cutout 1 (C_1)	2.8
Cutout 2 (C_2)	1.23
Slit 1 (S_1)	2
Slit 2 (S_2)	1

(b)

Length	Size (mm)	Width	Size (mm)
L_{S1}	4	W_{S1}	15
L_{S2}	7.78	W_{S2}	1.5
L_{S3}	3.9	W_{S3}	4.2
L_{S4}	1.58	W_{S4}	4.4

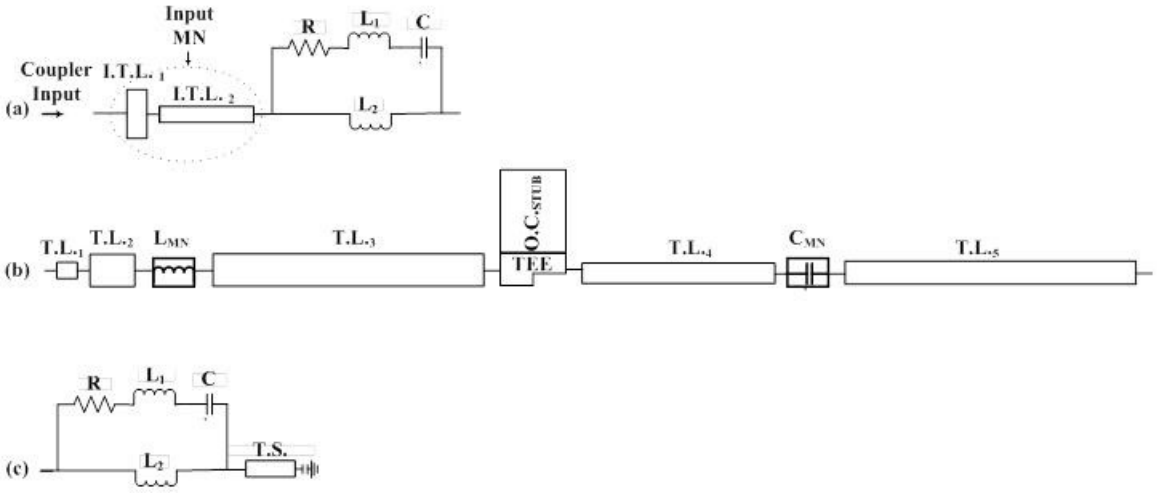

Figure 5.18 Matching network in each half of the four-element CP array. (a) Input matching network and single element model for the middle patch elements. (b) Matching network between two patch elements. (c) Single element model for the patches at each end of the array.

Table 5.10 Characteristics of the matching network for the four-element CP array.

	Length (mm)	Width (mm)
$I.T.L._1$	0.64	1.43
$I.T.L._2$	3.88	0.6
$T.L._1$	0.44	0.6
$T.L._2$	0.98	0.67
$T.L._3$	10.71	1.11
$T.L._4$	7.77	0.6
$T.L._5$	10.51	0.81
$O.C._{STUB}$	2.24	2.72
T.S.	1.48	1

The simulations of the second generation four-element CP array revealed that CP bandwidth is somewhat increased if greater element spacing is allowed. Similar to the meandered four-element CP array, the axial ratio in Figure 5.19 at 4.75 GHz is 5.1 dB, while its value at 5.25 GHz is 4.95 dB. The axial ratio at the center frequency of 5 GHz is however 0.65 dB lower compared to the meandered CP array and it is 1.85 dB. The axial ratio is below 3 dB over 280 MHz, from 4.82 GHz to 5.1 GHz. The S_{11} of this array shown Figure 5.20 is below -10 dB from 4.35 GHz to 4.62 GHz (280 MHz) and from 4.84 GHz to 5.21 GHz (370 MHz), while its value goes up to -9.3 dB for the frequencies between 4.62 GHz and 4.84 GHz. It can be noted that a slight increase in the CP bandwidth and a lower axial ratio at the center frequency of 5 GHz is achieved at the expense of increasing the overall size of the array from (136.5 x 37.2) mm in the meandered architecture, to (151.9 x 31.2) mm in the non-meandered topology of the four-element Z-slot aperture-coupled CP array.

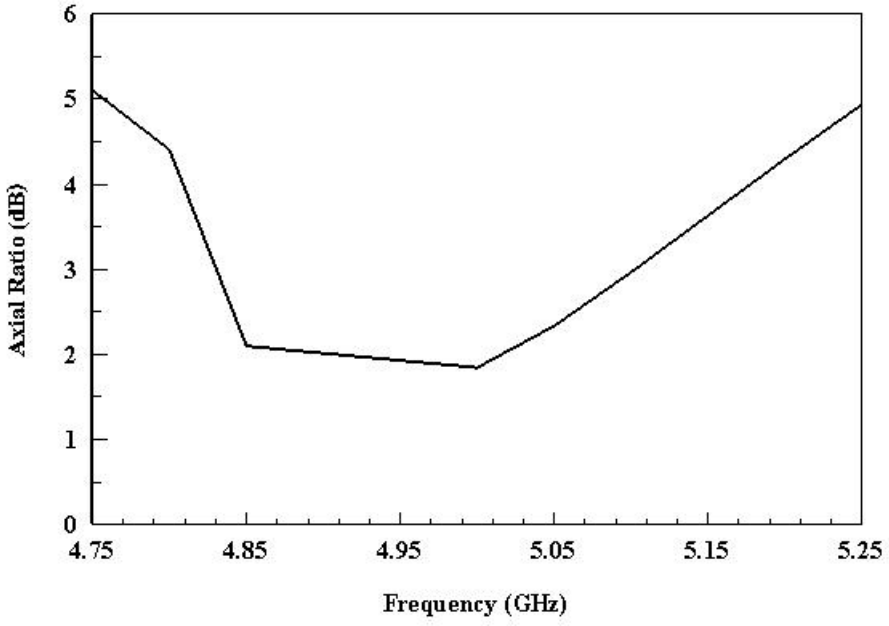

Figure 5.19 Simulated axial ratio over frequency for the four-element Z-slot aperture-coupled array.

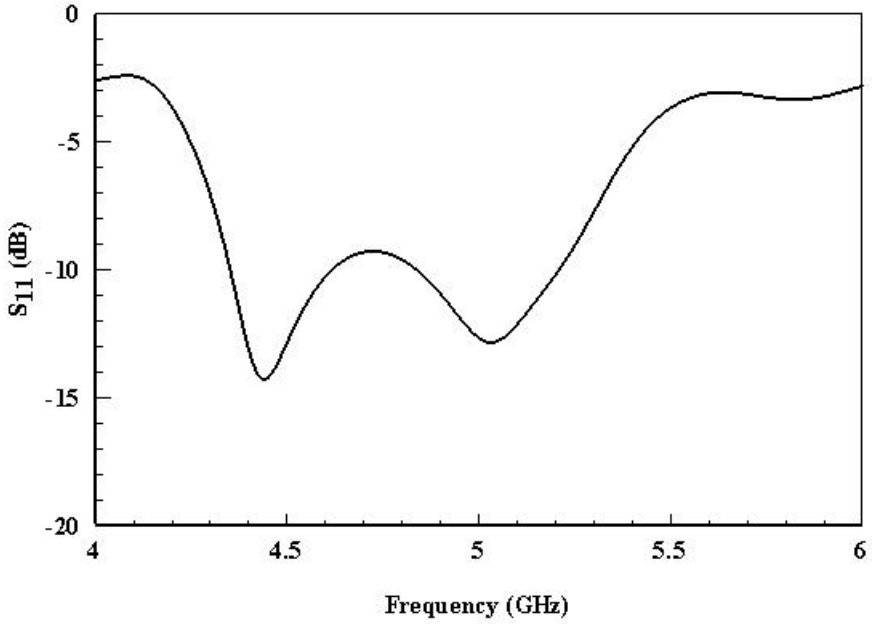

Figure 5.20 Simulated S_{11} of the four-element Z-slot aperture-coupled CP array.

The comparison of two E-plane patterns of the second generation four-element CP array is shown in Figure 5.21. These E-plane patterns also compare well for angles close to broadside (+/- 19 degrees) and the simulated directivity of this architecture is around 12.1 dB. Similar to the axial ratio bandwidth, directivity is also not greatly increased with increased element spacing. However, the optimization of both the meandered and the second generation four-element CP arrays thus far shows promise that the additional adjustment of the antenna elements and the matching network used within these arrays may yield better axial ratio and impedance bandwidth.

The isolation between LHCP and RHCP, shown in Figure 5.22, is ~19.5 dB at 5 GHz and 18.4 dB and 15.4 dB at 3 dB axial ratio bandwidth limits. This result shows 3 dB improvement in isolation at 5 GHz of the four-element CP array compared to the array using meandered matching networks sections presented in the previous section.

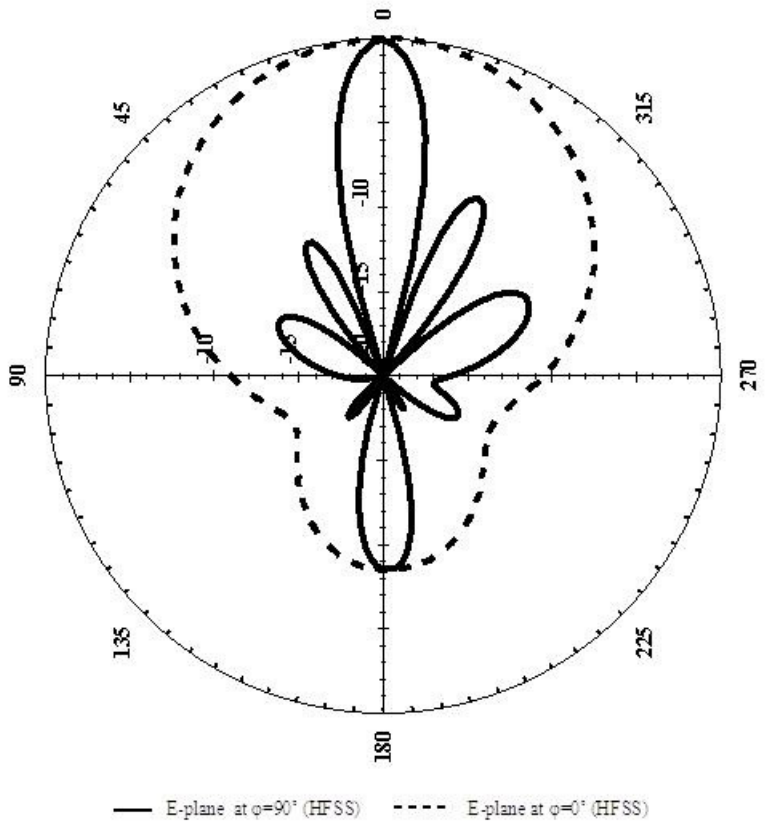

Figure 5.21 Comparison of the simulated (HFSS) E-plane patterns at φ=90˚ and φ=0˚ for the four-element Z-slot aperture-coupled CP array.

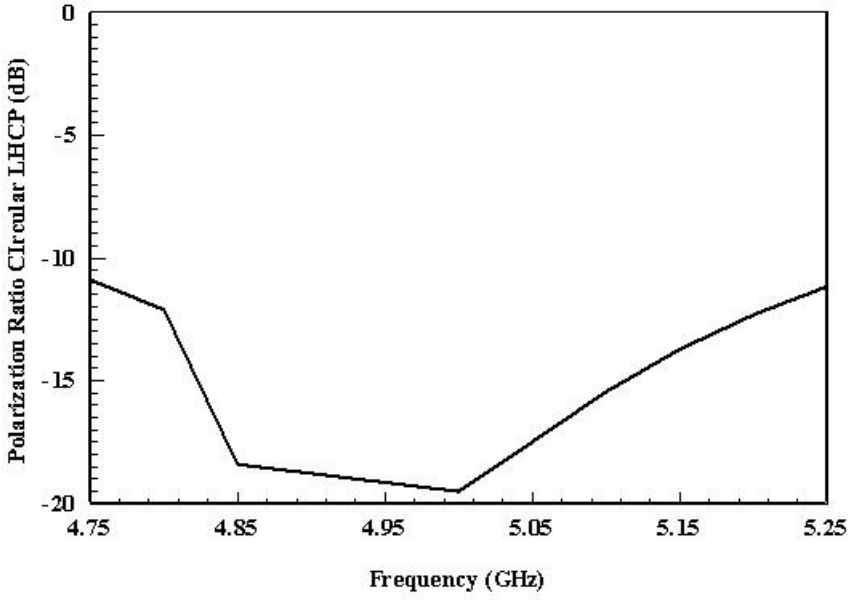

Figure 5.22 Simulated (HFSS) LHCP polarization ratio of the four-element CP array.

5.3.4 Inductor and Capacitor Circuit Representations for Matching Networks of Four-Element CP Arrays

Both matching networks presented in the previous two sections utilize Modelithics capacitor and inductor models. However, there is great difficulty in performing 3-D far-field simulations needed to accurately develop arrays when either lumped capacitor or inductor models are part of their structures. To circumvent this issue, appropriate models were developed for simulation in HFSS. Thus, the goal was to find suitable HFSS representations of Modelithics capacitor and inductor models used in ADS schematics. HFSS allows the use of RLC boundaries, where the required R, L or C value would be applied to a sheet of certain size. These boundaries along with the models developed were used to construct HFSS representations of Modelithics capacitor and inductor models. Figure 5.23 (a) shows representations of Modelithics capacitors and inductors used in designing matching networks in an ADS schematic. The size of the RLC boundary used in HFSS representations matched the size of the actual capacitor or inductor used in Modelithics models. Thus, placing any additional circuit component (apart from capacitor or inductor itself) in the equivalent HFSS representation would change the topology of the array. The pads used in Modelithics models were brought closer together to allow the use and placement of additional components (open-circuited stubs) in the models without changing the overall width of the component. The ADS schematic simulations of the Modelithics models with altered pad spacing were performed and compared to the actual pad spacing to assure that this change does not alter their simulated performance. Subsequently, ADS capacitor and inductor models using ideal L and C components (Figure 2.23 (b)) were developed, where open circuited stubs on each side of capacitor and inductor models occupied the same width gained by

reduction of pad spacing. As a final point, in addition to open circuited stubs in both capacitor and inductor ADS models, ideal L and C components were represented by RLC boundaries in HFSS (5.23 (c)). The HFSS optimized values of L_C, C_C and L_L, and open circuited stub lengths that represent C_{MN} and L_{MN} Modelithics capacitor and inductor models, respectively are given in Table 5.11.

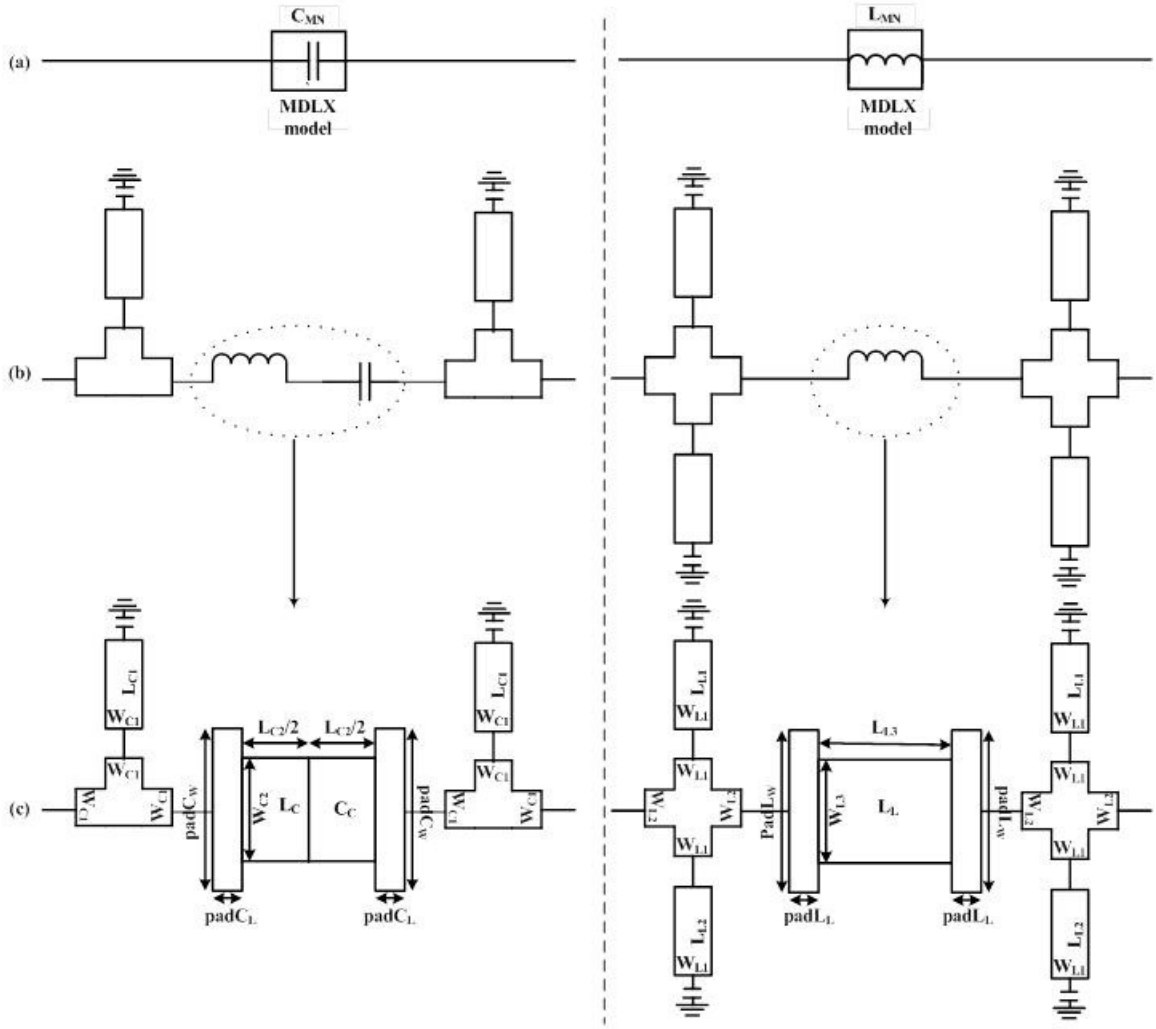

Figure 5.23 Capacitor (left) and inductor (right) models. (a) Representation of Modelithics models for 0.2pF capacitor and 1nH inductor. (b) ADS circuit model of Modelithics capacitor and inductor model. (c) Capacitor and inductor topology used to represent ADS circuit models in HFSS.

Table 5.11 Characteristics of capacitor and inductor HFSS topologies.

Length	Size (mm)	Width	Size (mm)
L_{MN}=1 nH ; C_{MN}=0.2 pF; L_C=0.55 nH ; C_C=0.145 pF; L_L=0.6 nH ;			
L_{C1}	0.7	W_{C1}	0.025
L_{C2}	1.016	W_{C2}	0.508
L_{L1}	0.02	W_{LI}	0.075
L_{L2}	0.02	W_{L2}	0.07
L_{L3}	1.018	W_{L3}	0.508
$padL_L$	0.112	$padL_W$	0.7
$padC_L$	0.064	$padC_W$	0.711

Comparison between the Modelithics (MDLX) capacitor model, ADS circuit model using ideal components and open circuited stubs, and the capacitor HFSS representation is shown in Figure 24. Both S_{11} and the phase of S_{12} between these models compare well.

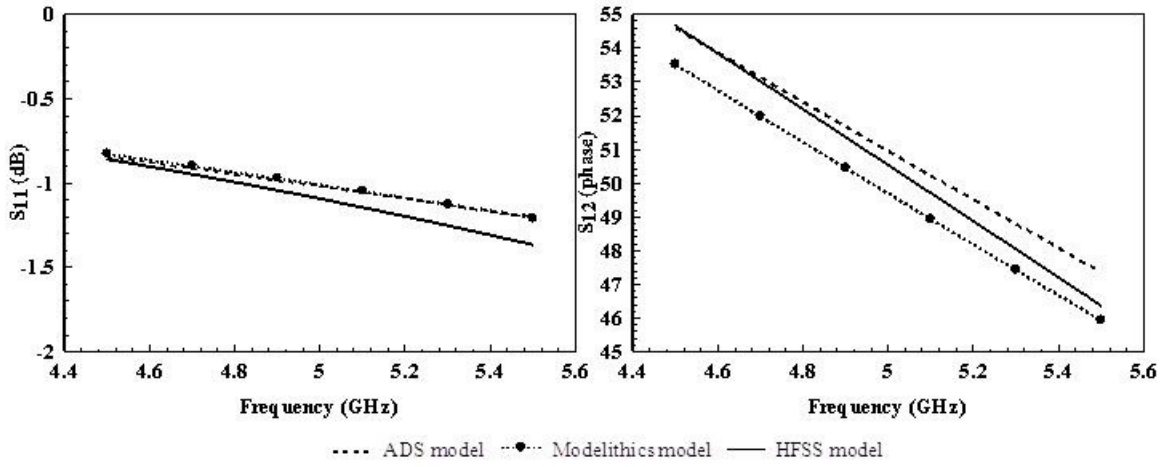

Figure 5.24 S_{11} (dB) and S_{12} (degrees) comparison between MDLX, ADS and HFSS models for capacitor.

Similarly, S_{11} and the phase of S_{12} between the Modelithics inductor model, its ADS circuit model using ideal components and open circuited stubs, and the HFSS representation are shown in Figure 25. The results in Figure 25 shows that developed

HFSS representations can be used to adequately represent Modelithics inductors used in four-element CP arrays.

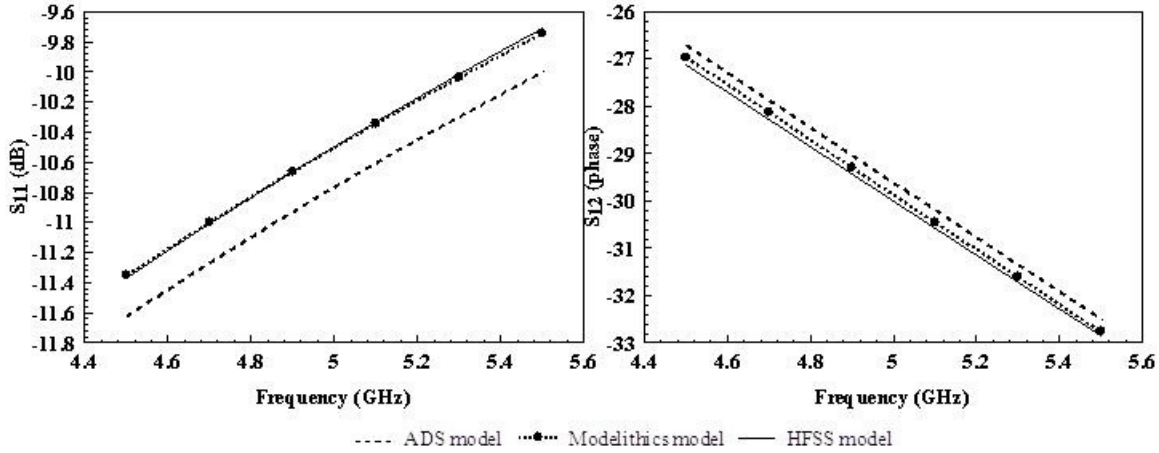

Figure 5.25 S_{11} (dB) and S_{12} (degrees) comparison between MDLX, ADS and HFSS models for inductor.

5.4. Conclusion

The approach to attain wide circular polarization bandwidth using Z-shaped aperture was presented. The measured axial ratio bandwidth of the single Z-slot aperture-coupled antenna was ~10% with simulated directivity of 6.5 dB. Two architectures of series-fed CP four-element arrays employing Z-shaped aperture were also designed using a series-feeding approach described in this work. Their directivities are around 12 dB with +/-10 degree half-power bandwidth. Finally, HFSS circuit representations of inductor and capacitor models that adequately represent components used in the fabrications of the arrays were developed as well.

CHAPTER 6:

SUMMARY AND RECOMMENDATIONS

6.1 Summary

The methodology for designing series-fed N-element arrays suitable for scouting applications, unmanned air vehicles and similar uses was presented in Chapter 3. The series-fed arrangement presented in this work offers the ability to develop N-element array architectures with a small footprint by circumventing the use of a corporate-feed and allows for an easy addition of elements for increased gain. The feeding approach was presented through the development of equivalent circuit models for aperture-coupled single antenna element and array structures. The single- and dual-fed series-fed four-element aperture-coupled array was designed to demonstrate the approach, while its validation was provided through a design of a single-fed six-element aperture-coupled array. In addition, elevation beam pointing stability over frequency in four- and six-element aperture-coupled arrays was achieved with the use of anti-symmetric 180-degree out of phase feed in dual-fed four-element aperture-coupled arrays and via a 180-degree Rat-Race coupler employed within each pair of elements in both single-fed four- and six-element array structures. The single-fed four-element aperture-coupled array presented has 11.5 dB of gain with 15 % 10 dB impedance bandwidth with a center frequency at 5 GHz, while the single-fed six-element aperture-coupled array offers 12.6 dB gain and 16% 10 dB impedance bandwidth centered at 5 GHz.

The six single-fed series-fed four-element aperture-coupled arrays were implemented in the configuration of a hexagonal omni-directional radiator in Chapter 4. The omni-directional antenna presented in this work has the ability to provide sectoral radiation and incorporate a beam forming/power distribution network. Sectoral radiation is demonstrated through the use of fewer than six single-fed aperture-coupled sub-arrays to provide a higher gain directional antenna pattern at the specific angles. Furthermore, additional pattern reconfiguration is shown through the use of different feed phase differentials if dual-fed four-element aperture-coupled arrays were used to assemble the hexagonal omni-directional radiator. A beam forming or power distribution network can be used at the input of each of the six four-element aperture-coupled arrays to accommodate and reconfigure the omni-directional pattern for a specific application need, for example, angle of radiation in azimuth, tilt compensation, gain increase, etc. The presented omni-directional radiator was designed at the center frequency of 5 GHz and has a measured gain of 6 dB with 0.6 dB gain ripple across azimuth. Additionally, the gain at the specific azimuth angle across 15% 10 dB impedance bandwidth varies by only 0.6 dB.

The circular-polarization ability for improving communication link connectivity and multipath interference mitigation is presented in Chapter 5 through the development of the Z-slot aperture-coupled approach for single aperture-coupled antenna and series-fed aperture-coupled arrays. The circular-polarization approach is shown to provide higher circular-polarization bandwidth without the use of external couplers to induce 90-degree phase shift between orthogonal, equal-amplitude field components. The proposed Z-slot aperture-coupled approach was used in developing single RHCP Z-slot aperture-

coupled antenna with ~10% CP and 10 dB impedance bandwidth centered at 5 GHz. Furthermore, the developed approach was demonstrated in two series-fed four-element Z-slot aperture-coupled CP array implementations that achieve 5% and 5.6% CP bandwidth. The meandered Z-slot aperture-coupled CP array with 5% CP bandwidth has ~12% 10 dB impedance bandwidth and a ~17 dB LHCP circular polarization ratio. Similarly, the second series-fed four-element Z-slot aperture-coupled CP array with 5.6% CP bandwidth has ~19.5 LHCP circular polarization ratio. Matching networks employed within two CP array architectures employ open-circuited stubs, transmission lines, and lumped L and C elements. Useful HFSS representations of these lumped elements were developed to enable successful 3-D HFSS simulations of the presented CP arrays.

6.2 Recommendations

Development of a power distribution network for the proposed omni-directional radiator could further validate its ability to provide sectoral radiation. Employing the ability to control the number of four-element aperture-coupled sub-array used to form a directional pattern could be provided by a switching power distribution network at the input of each individual sub-array. In addition, an omni-directional radiator could be assembled with six dual-fed series-fed four-element aperture-coupled array topologies with phase shifters at each end of the six sub-arrays to provide greater elevation steering capability. Lastly, further optimization of single and series-fed four-element Z-slot aperture coupled architectures may yield even greater CP bandwidth with lower back radiation. It would also be of great interest to configure a CP omni-directional radiator using four-element Z-slot aperture-coupled CP arrays and investigate its capabilities in terms of CP bandwidth and sectoral radiation. Reduction or elimination of back radiation

if the CP omni-directional radiator was pursued may be achieved by placing a ground plane in the center of the hexagonal radiator a proper distance away.

REFERENCES

[1] Nagasawa, K.; Matsuzuka, I.; , "Radiation field consideration of biconical horn antenna with different flare angles," *Antennas and Propagation, IEEE Transactions on* , vol.36, no.9, pp.1306-1310, Sep 1988.

[2] Howell J.M., Sharon T. E., "Geodesic Slotted Cylindrical Antenna", U.S. Patent PCT/US99/03434, February 18, 1999.

[3] Konishi, Y.; Ohtsuka, M.; Matsunaga, M.; Katagi, T.; "A linear array antenna using bifilar helical elements for mobile satellite communications," *Antennas and Propagation Society International Symposium, 1994. AP-S. Digest*, vol.2, pp.1020-1023 vol.2, 20-24 Jun 1994.

[4] Peng, S.; Xu, S.; Schwering, F.; "Omni-directional periodic rod antenna," *Antennas and Propagation Society International Symposium, 1986*, vol.24, pp. 697- 700, Jun 1986.

[5] Iskander, M.F.; Zhijun Zhang; Zhengqing Yun; Isom, R.; "Coaxial continuous transverse stub (CTS) array," *Microwave and Wireless Components Letters, IEEE*, vol.11, no.12, pp.489-491, Dec 2001.

[6] Shrivastav, A.K.; Das, A.; Das, S.K.; "Wide band omni directional radiating array for cylindrical body," *Electromagnetic Interference and Compatibility, 2003. INCEMIC 2003. 8th International Conference on*, pp. 359- 360, 18-19 Dec. 2003.

[7] Loffler, D.; Wiesbeckl, W.; Johannisson, B.; "Conformal aperture coupled microstrip phased array on a cylindrical surface," *Antennas and Propagation Society International Symposium, 1999. IEEE*, pp.882-885 vol.2, Aug 1999.

[8] Knott, P.; "Faceted vs. smoothly curved antenna front-end for a conformal array radar demonstrator," *Radar Conference, 2005. EURAD 2005. European*, pp.193-196, 6-7 Oct. 2005.

[9] Matolak, D.W.; Frolik, J.; , "Worse-than-Rayleigh fading: Experimental results and theoretical models," Communications Magazine, IEEE , vol.49, no.4, pp.140-146, April 2011.

[10] Frolik, J.; , "A case for considering hyper-Rayleigh fading channels," Wireless Communications, IEEE Transactions on , vol.6, no.4, pp.1235-1239, April 2007.

[11] Targonski, S.D.; Pozar, D.M.; , "Design of wideband circularly polarized aperture-coupled microstrip antennas," *Antennas and Propagation, IEEE Transactions on* , vol.41, no.2, pp.214-220, Feb 1993.

[12] Aloni, E.; Kastner, R.; , "Analysis of a dual circularly polarized microstrip antenna fed by crossed slots," *Antennas and Propagation, IEEE Transactions on* , vol.42, no.8, pp.1053-1058, Aug 1994.

[13] Tsao, C.H.; Hwang, Y.M.; Kilburg, F.; Dietrich, F.; , "Aperture-coupled patch antennas with wide-bandwidth and dual-polarization capabilities," *Antennas and Propagation Society International Symposium, 1988. AP-S. Digest* , pp.936-939 vol.3, 6-10 Jun 1988.

[14] Aksun, M.I.; Wang, Z.H.; Chuang, S.L.; Lo, Y.T.; , "Circular polarization operation of double-slot fed microstrip antennas," *Antennas and Propagation Society International Symposium, 1989. AP-S. Digest* , pp.640-643 vol.2, 26-30 June 1989.

[15] Adrian, A.; Schaubert, D.H.; , "Dual aperture-coupled microstrip antenna for dual or circular polarisation," *Electronics Letters* , vol.23, no.23, pp.1226-1228, November 5 1987.

[16] Edimo, M.; Sharaiha, A.; Terret, C.; , "Optimised feeding of dual polarised broadband aperture-coupled printed antenna," *Electronics Letters* , vol.28, no.19, pp.1785-1787, 10 Sept. 1992.

[17] Pozar, D.M.; , "Microstrip antenna aperture-coupled to a microstripline," Electronics Letters , vol.21, no.2, pp.49-50, January 17 1985.

[18] Ittipiboon, A.; Oostlander, R.; Antar, Y.M.M.; Cuhaci, M.; , "A modal expansion method of analysis and measurement on aperture-coupled microstrip antenna," *Antennas and Propagation, IEEE Transactions on* , vol.39, no.11, pp.1567-1574, Nov 1991.

[19] Pozar, D.; , "A reciprocity method of analysis for printed slot and slot-coupled microstrip antennas," *Antennas and Propagation, IEEE Transactions on* , vol.34, no.12, pp. 1439- 1446, Dec 1986.

[20] Sullivan, P.; Schaubert, D.; , "Analysis of an aperture coupled microstrip antenna," *Antennas and Propagation, IEEE Transactions on* , vol.34, no.8, pp. 977- 984, Aug 1986.

[21] Himdi, M.; Daniel, J.P.; Terret, C.; , "Analysis of aperture-coupled microstrip antenna using cavity method," *Electronics Letters* , vol.25, no.6, pp.391-392, 6 March 1989.

[22] Xian Hua Yang; Shafai, L.; , "Characteristics of aperture coupled microstrip antennas with various radiating patches and coupling apertures," *Antennas and Propagation, IEEE Transactions on* , vol.43, no.1, pp.72-78, Jan 1995.

[23] Bhattacharyya, A.K.; Antar, Y.M.M.; Ittipiboon, A.; , "Full wave analysis of an aperture-coupled patch antenna," *Electronics Letters* , vol.27, no.2, pp.153-155, 17 Jan. 1991.

[24] Das, B.; Joshi, K.; , "Impedance of a radiating slot in the ground plane of a microstripline," *Antennas and Propagation, IEEE Transactions on* , vol.30, no.5, pp. 922- 926, Sep 1982.

[25] Himdi, M.; Daniel, J.P.; Terret, C.; , "Transmission line analysis of aperture-coupled microstrip antenna," *Electronics Letters* , vol.25, no.18, pp.1229-1230, 31 Aug. 1989.

[26] Balanis, C.A. . *Antenna theory: Analysis and Design*. John Wiley & Sons, Inc., 2005.

[27] Balanis, C. A. . *Advanced Engineering Electromagnetics*. John Wiley & Sons, Inc., 1989.

[28] Bethe H.A. , "Theory of Diffraction by Small Holes" *Physical Review*, vol. 66, no. 7-8, pp. 163-182, 1944.

[29] Pozar, D.M.; , "Microstrip antennas," Proceedings of the IEEE , vol.80, no.1, pp.79-91, Jan 1992.

[30] Garg, R., Bhartia, P., Bahl, I., Ittipiboon, A. . *Microstrip Antenna Design Handbook*. Norwood, MA: Artech House, 2001.

[31] Pozar, D.; , "Considerations for millimeter wave printed antennas," *Antennas and Propagation, IEEE Transactions on* , vol.31, no.5, pp. 740- 747, Sep 1983.

[32] Harrington, R.F.. *Time-Harmonic Electromagnetic Fields*. McGraw-Hill, Inc., 1961.

[33] Katehi, P.; Alexopoulos, N.; , "On the effect of substrate thickness and permittivity on printed circuit dipole properties," *Antennas and Propagation, IEEE Transactions on* , vol.31, no.1, pp. 34- 39, Jan 1983.

[34] Pozar, D.M.; , "Rigorous closed-form expressions for the surface wave loss of printed antennas," *Electronics Letters* , vol.26, no.13, pp.954-956, 21 June 1990.

[35] Nauwelaers, B.; Van De Capelle, A.; , "Surface wave losses of rectangular microstrip antennas," *Electronics Letters* , vol.25, no.11, pp.696-697, 25 May 1989.

[36] Collier, R.J.; White, P.D.; , "Surface Waves in Microstrip Circuits," *Microwave Conference, 1976. 6th European* , pp.632-636, 14-17 Sept. 1976.

[37] Kittenplon, H.; , "Surface-wave effect in a wideband aperture-coupled stacked microstrip antenna array," *Electronics Letters* , vol.32, no.9, pp.792-793, 25 Apr 1996.

[38] Croq, F.; Papiernik, A.; , "Large bandwidth aperture-coupled microstrip antenna," *Electronics Letters* , vol.26, no.16, pp.1293-1294, 2 Aug. 1990.

[39] Croq, F.; Pozar, D.M.; , "Millimeter-wave design of wide-band aperture-coupled stacked microstrip antennas," *Antennas and Propagation, IEEE Transactions on* , vol.39, no.12, pp.1770-1776, Dec 1991.

[40] Targonski, S.D.; Waterhouse, R.B.; , "An aperture coupled stacked patch antenna with 50% bandwidth," *Antennas and Propagation Society International Symposium, 1996. AP-S. Digest* , vol.1, pp.18-21, 21-26 Jul 1996.

[41] Richards, W.; Lo, Y.; , "An improved theory for microstrip antennas and applications," *Antennas and Propagation Society International Symposium, 1979* , vol.17, pp. 113- 116, Jun 1979.

[42] Haneishi M.; Yoshida S.; , "A design method of circularly polarized rectangular microstrip antenna by one-point feed" *Electronics and Communications in Japan (Part I: Communications)*, vol. 64, no. 4, pp. 46-54, April 1981.

[43] Sharma, P.; Gupta, K.; , "Analysis and optimized design of single feed circularly polarized microstrip antennas," *Antennas and Propagation, IEEE Transactions on* , vol.31, no.6, pp. 949- 955, Nov 1983.

[44] Richards, W.; Lo, Y.; , "Design and theory of circularly polarized microstrip antennas," *Antennas and Propagation Society International Symposium, 1979* , vol.17, pp. 117- 120, Jun 1979.

[45] Aksun, M.I.; Chuang, S.-L.; Lo, Y.T.; , "On slot-coupled microstrip antennas and their applications to CP operation-theory and experiment," *Antennas and Propagation, IEEE Transactions on* , vol.38, no.8, pp.1224-1230, Aug 1990.

[46] Lo, Y.T.; Richards, W.F.; , "Perturbation approach to design of circularly polarised microstrip antennas," *Electronics Letters* , vol.17, no.11, pp.383-385, May 28 1981.

[47] Lo, Y.T.; Engst, B.; Lee, R.Q.; , "Simple design formulas for circularly polarised microstrip antennas," *Microwaves, Antennas and Propagation, IEE Proceedings H* , vol.135, no.3, pp. 213- 215, Jun 1988.

[48] Aksun, M.I.; Chuang, S.L.; Lo, Y.T.; , "Theory and experiment of electromagnetically excited microstrip antennas for circular polarization operation," *Antennas and Propagation Society International Symposium, 1989. AP-S. Digest* , vol., no., pp.1142-1145 vol.2, 26-30 June 1989.

[49] Hyungrak Kim; Byoung Moo Lee; Young Joong Yoon; , "A single-feeding circularly polarized microstrip antenna with the effect of hybrid feeding," *Antennas and Wireless Propagation Letters, IEEE* , vol.2, no.1, pp.74-77, 2003.

[50] Vlasits, T.; Korolkiewicz, E.; Sambell, A.; Robinson, B.; , "Performance of a cross-aperture coupled single feed circularly polarised patch antenna," *Electronics Letters* , vol.32, no.7, pp.612-613, 28 Mar 1996.

[51] Chih-Yu Huang; Jian-Yi Wu; Kin-Lu Wong; , "Slot-coupled microstrip antenna for broadband circular polarisation ," *Electronics Letters* , vol.34, no.9, pp.835-836, 30 Apr 1998.

[52] Stark, A.; Jacob, A.F.; , "A single-feed star-slot-coupled patch antenna with circular polarization," *German Microwave Conference, 2010*, pp.70-73, 15-17 March 2010.

[53] Pozar, D.; Schaubert, D.; , "Scan blindness in infinite phased arrays of printed dipoles," *Antennas and Propagation, IEEE Transactions on* , vol.32, no.6, pp. 602-610, Jun 1984.

[54] Mailloux, R.J.; , "Antenna array architecture," *Proceedings of the IEEE* , vol.80, no.1, pp.163-172, Jan 1992.

[55] Pan, S.-G.; Wolff, I.; , "Computation of mutual coupling between slot-coupled microstrip patches in a finite array," *Antennas and Propagation, IEEE Transactions on* , vol.40, no.9, pp.1047-1053, Sep 1992.

[56] Keller, M.G.; Roscoe, D.; Antar, Y.M.M.; Ittipiboon, A.; , "Active millimetre-wave aperture-coupled microstrip patch antenna array," *Electronics Letters* , vol.31, no.1, pp.2-4, 5 Jan 1995.

[57] Hertl, Ivo; Strycek, Michal; , "Different feeding mechanisms for aperture coupled patch arrays," *Antennas and Propagation (EuCAP), 2010 Proceedings of the Fourth European Conference on*, pp.1-3, 12-16 April 2010.

[58] Methfessel, S.; Schmidt, L.-P.; , "Design and measurement of a wideband aperture-coupled and polarization-agile stacked-patch antenna-array for monopulse radar applications," *Antennas and Propagation, 2009. EuCAP 2009. 3rd European Conference on*, pp.1350-1353, 23-27 March 2009.

[59] Pozar, D.; , "Directivity of omnidirectional antennas," *Antennas and Propagation Magazine, IEEE* , vol.35, no.5, pp.50-51, Oct. 1993.

[60] McDonald, N.; , "Approximate relationship between directivity and beamwidth for broadside collinear arrays," *Antennas and Propagation, IEEE Transactions on* , vol.26, no.2, pp. 340- 341, Mar 1978.

[61] Johnson, R. C. ; Jasik, H.; . *Antenna Engineering Handbook*. McGraw-Hill, Inc., 1961.

[62] Ashkenazy, J.; Shtrikman, S.; Treves, D.; , "Conformal microstrip arrays on cylinders," *Microwaves, Antennas and Propagation, IEE Proceedings H* , vol.135, no.2, pp. 132- 134, Apr 1988.

[63] James, J.R.; Hall, P.S.; .*Handbook of Microstrip Antennas*. Peter Peregrinus Ltd., London, UK 1989, vol 2. .

[64] Vallecchi, Andrea; Gentili, Guido Biffi; , "Dual-polarized cylindrically conformal microstrip patch antennas and arrays," *Antennas and Propagation (EuCAP), 2010 Proceedings of the Fourth European Conference on*, pp.1-3, 12-16 April 2010.

[65] Hall, R.C.; Wu, D.I.; , "Modeling and design of circularly-polarized cylindrical wraparound microstrip antennas," *Antennas and Propagation Society International Symposium, 1996. AP-S. Digest* , vol.1, pp.672-675 vol.1, 21-26 Jul 1996.

[66] Wu, D.L.; , "Omnidirectional circularly-polarized conformal microstrip array for telemetry applications," *Antennas and Propagation Society International Symposium,* 1995. *AP-S. Digest* , vol.2, pp.998-1001 vol.2, 18-23 Jun 1995.

[67] Pozar, D.M.; , "Analysis of an infinite phased array of aperture coupled microstrip patches," *Antennas and Propagation, IEEE Transactions on* , vol.37, no.4, pp.418-425, Apr 1989.

[68] Hall, P.S.; Hall, C.M.; "Coplanar corporate feed effects in microstrip patch array design," *Microwaves, Antennas and Propagation, IEE Proceedings H*, vol.135, no.3, pp. 180- 186, Jun 1988.

[69] © [2008] IEEE. Reprinted, with permission, from [Zivanovic, B., McKnight, J. Weller, T., Costas, C., A dual-feed series microstrip patch array, *Antennas and Propagation Society International Symposium, 2008. AP-S 2008. IEEE*, July/2008].

[70] © [2009] IEEE. Reprinted, with permission, from [Zivanovic, B. Weller, T., Costas, C., Omni-directional array using a cylindrical configuration of slot-coupled microstrip antennas, *Microwave Conference, 2009. EuMC 2009. European*, and Oct. /2009].

[71] © [2012] IEEE. Reprinted, with permission, from [Zivanovic, B. Weller, T., Costas, C., Series-Fed Microstrip Antenna Arrays and Their Application to Omni-Directional Antennas, Antennas and Propagation, IEEE Transactions on, Oct./2012].

[72] Munson, R.; , "Conformal microstrip antennas and microstrip phased arrays," Antennas and Propagation, IEEE Transactions on , vol.22, no.1, pp. 74- 78, Jan 1974.

APPENDICES

Appendix A: Closed-Form Expressions for the Radiation Patterns of a Microstrip Antenna Based on a Two-Slot Model

The radiation pattern of the microstrip antenna can be expressed from an array of two apertures with width W and height h (corresponding to the width of the microstrip antenna and the thickness of the substrate, respectively). If the electric field across the aperture is given as $E_z=-V_0/h$ with $E_y=0$ ($\vec{M} = \vec{E} \times \hat{n}$), the z-component of the magnetic current is zero, while the y-component of the magnetic current is zero everywhere except for $-W/2 \le y \le W/2$ and $-h/2 \le z \le h/2$, where it is equal to V_0/h [30]. The far-zone vector potential at (y',z')of a rectangular magnetic sheet (Figure A.1) with length h and width W in (A.1) [30] can be used to compute far-field components of a microstrip antenna.

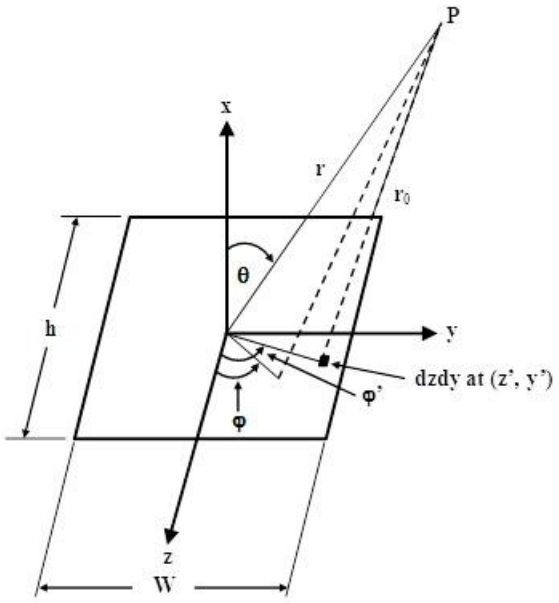

Figure A.1 Magnetic current sheet [30]. Reproduced by permission from Ramesh Garg, Prakash Bhartia, Inder Bahl, Apisak Ittipiboon, *Microstrip Antenna Design Handbook*, Norwood, MA: Artech House, Inc., 2001. © 2001 by Artech House, Inc.

Appendix A (continued)

$$\begin{aligned}\overline{F} &= \frac{\varepsilon_0 e^{-jk_0 r}}{4\pi r}\int_{-h/2}^{h/2}\int_{-W/2}^{W/2}\overline{M}(z',y')e^{[jk_0(z'\sin\theta\cos\phi+y'\sin\theta\sin\phi)]}dz'\,dy' \\ &= \frac{\varepsilon_0 e^{-jk_0 r}}{4\pi r}\int_{-h/2}^{h/2}\int_{-W/2}^{W/2}\left(M_z(z',y')\hat{z}+M_y(z',y')\hat{y}\right)e^{[jk_0(z'\sin\theta\cos\phi+y'\sin\theta\sin\phi)]}dz'\,dy' \\ &= F_z + F_y \quad \text{and} \quad F_x = 0\end{aligned} \tag{A.1}$$

The far-field components of the E-field, taking into account only magnetic currents (on the aperture) (A.2) [30], are written in spherical coordinates as (A.3) [30] and (A.4) [30].

$$\overline{E} = -\eta_0 \hat{r}\times\overline{H} = -\eta_0\left(\hat{\phi}H_\theta + \hat{\theta}H_\phi\right) = j\omega\eta_0\left(\hat{\phi}F_\theta + \hat{\theta}F_\phi\right) \tag{A.2}$$

$$E_\theta = j\omega\eta_0\left(F_z\sin\phi - F_y\cos\phi\right) \tag{A.3}$$

and

$$E_\phi = j\omega\eta_0\left(F_z\cos\theta\cos\phi + F_y\cos\theta\sin\phi\right) \tag{A.4}$$

For the radiating apertures of the microstrip antenna, the y-component of the far-zone vector potential defined in (A.1) can be written as (A.5) [30] to determine θ and φ far E-field components using (A.3) and (A.4).

$$F_y = \frac{\varepsilon_0 V_0 W e^{-jk_0 r}}{4\pi r}\frac{\sin\left(k_0 h\sin\theta\cos\phi/2\right)}{k_0 h\sin\theta\cos\phi/2}\frac{\sin\left(k_0 W\sin\theta\sin\phi/2\right)}{k_0 W\sin\theta\sin\phi/2} \tag{A.5}$$

The far-zone E-field components of a single aperture, radiating in free space ($h \ll \lambda_0$), are then given by (A.6) [30] and (A.7) [30].

$$E_\theta = -\frac{jk_0 V_0 W e^{-jk_0 r}}{4\pi r}\frac{\sin\left(k_0 h\sin\theta\cos\phi/2\right)}{k_0 h\sin\theta\cos\phi/2}\frac{\sin\left(k_0 W\sin\theta\sin\phi/2\right)}{k_0 W\sin\theta\sin\phi/2}\cos\phi \tag{A.6}$$

$$E_\phi = \frac{jk_0 V_0 W e^{-jk_0 r}}{4\pi r}\frac{\sin\left(k_0 h\sin\theta\cos\phi/2\right)}{k_0 h\sin\theta\cos\phi/2}\frac{\sin\left(k_0 W\sin\theta\sin\phi/2\right)}{k_0 W\sin\theta\sin\phi/2}\cos\theta\sin\phi \tag{A.7}$$

Appendix A (continued)

Radiation patterns of the microstrip antenna (E-plane(φ=0˚) and H-plane(φ=90˚)) result from multiplying radiation pattern of a single aperture ((A.6) and (A.7))with an array factor in (A.8) [30].

$$AF = 2\cos k_0 L \sin\theta \cos\phi / 2 \tag{A.8}$$

Finally, reciprocity theorem is utilized on two infinitesimal dipoles to take into account the effect of the ground plane and substrate (ε_r) on the radiation pattern of the microstrip antenna. Accordingly, one of the dipoles is placed on the surface of the substrate, while the second dipole is placed far away from the first dipole in free-space. The reciprocity theorem results in expressions (A.9) [30] for the E-plane pattern and the one in (A.10) [30] for the H-plane pattern. The final E-plane radiation pattern is then the product of (A.6), (A.8) and (A.9) for φ=0˚. Similarly, the final H-plane radiation pattern is the product of (A.7), (A.8) and (A.10) evaluated at φ=90˚.

$$F_3(\theta) = \frac{2\cos\theta\sqrt{\varepsilon_r - \sin^2\theta}}{\sqrt{\varepsilon_r - \sin^2\theta} - j\varepsilon_r \cos\theta \cot\left(k_0 h\sqrt{\varepsilon_r - \sin^2\theta}\right)} \tag{A.9}$$

$$F_4(\theta) = \frac{2\cos\theta}{\cos\theta - j\sqrt{\varepsilon_r - \sin^2\theta}\cot\left(k_0 h\sqrt{\varepsilon_r - \sin^2\theta}\right)} \tag{A.10}$$

Appendix B: Conditions for Circular Polarization and Single-Fed Circularly Polarized Microstrip Antennas

In order to view how circular polarization is achieved in single-fed aperture-coupled antennas, the conditions for circular polarizations are briefly examined. Herein, circular polarization is presented as a special case of elliptical polarization shown in Figure B.1, where the instantaneous electric field vector (z=0, at all times) of the antenna is given by (B.1) [27], and the locus of the amplitude of the electric field vector is the one in (B.4) [27].

$$\begin{aligned} E(x,y,z;t) &= \hat{a}_x E_x + \hat{a}_y E_y = \mathrm{Re}\left[\hat{a}_x E_x^{+} e^{j(\omega t-\beta z)} + \hat{a}_y E_y^{+} e^{j(\omega t-\beta z)}\right] \\ &= \hat{a}_x E_{x_0}^{+} \cos(\omega t - \beta z + \varphi_x) + \hat{a}_y E_{y_0}^{+} \cos(\omega t - \beta z + \varphi_y) \end{aligned} \tag{B.1}$$

when $$E_{x_0}^{+} = (E_R + E_L) \tag{B.2}$$

and $$E_{y_0}^{+} = (E_R - E_L) \tag{B.3}$$

$$E = \sqrt{E_x + E_y} \tag{B.4}$$

(B.5) [27] represents the tilt of the ellipse with respect to x-axis (τ) in Figure B.1, where $0° \le \tau \le 180°$.

$$\tau = \frac{\pi}{2} - \frac{1}{2}\tan^{-1}\left[\frac{2E_{x_0}^{+}E_{y_0}^{+}}{\left(E_{x_0}^{+}\right)^2 - \left(E_{y_0}^{+}\right)^2}\cos(\Delta\varphi)\right] \tag{B.5}$$

Appendix B (continued)

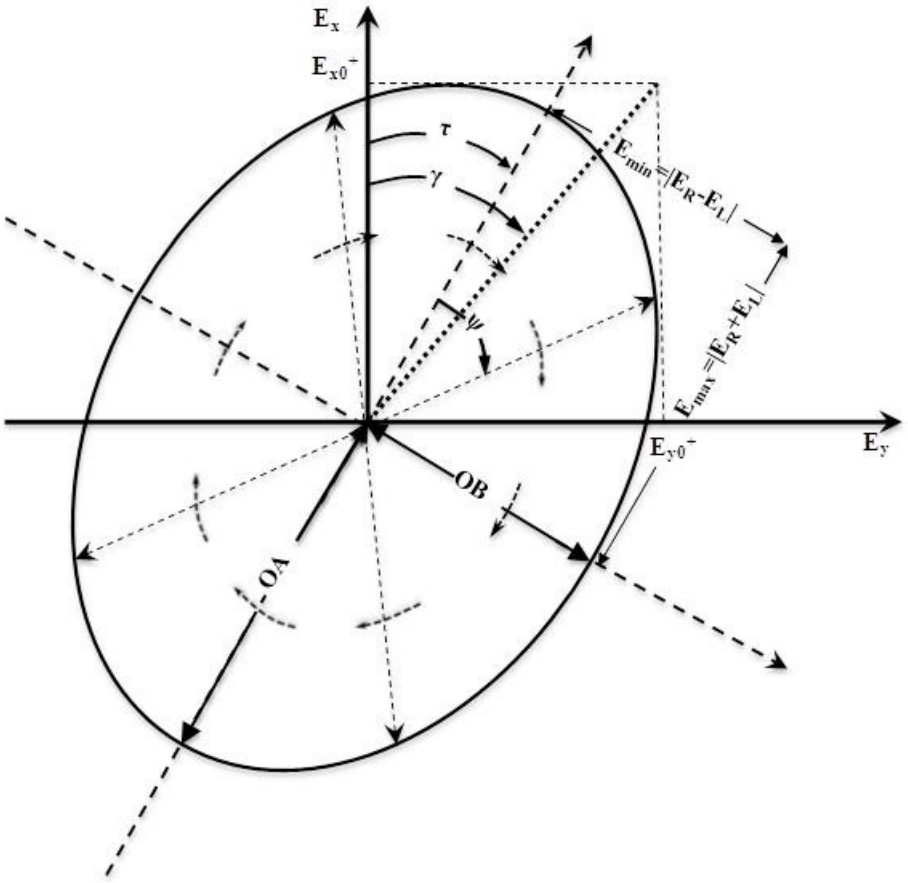

Figure B.1 Illustration of the trace of the locus of an electric field for elliptical polarization in time at the particular location [27]. Reprinted with permission from John Wiley & Sons, Inc..

Circular polarization is presented by Figure B.1 when major and minor axes of the ellipse (OA and OB) overlap with axes of the main coordinate system. In particular, circular polarization is realized when τ is $n\pi/2$ (n=0,1,2….), the maximum magnitudes of x and y components of the electric field vector (E_{x0}^{+},E_{y0}^{+}) are the same, and their time-phase difference (φ_y- φ_x) is odd multiples of $\pi/2$ ((B.6) [26]).

$$E_{x_0}^{+} = E_{y_0}^{+} = \begin{cases} E_R \\ E_L \end{cases} \quad \text{and} \quad \Delta\varphi = \varphi_y - \varphi_x = \begin{cases} -\left(\frac{1}{2}+2n\right)\pi & RHCP \quad (cw) \\ +\left(\frac{1}{2}+2n\right)\pi & LHCP \quad (ccw) \end{cases} \tag{B.6}$$

where n is 0,1,2… and the tilt of the locus of the amplitude of the electric field vector with respect to x-axis is given by ψ in (B.7) [27].

$$\psi = \tan^{-1}\left[\frac{E_y}{E_x}\right] \tag{B.7}$$

In the case of circular polarization (CP), the axial ratio as given by (B.8) [27], is a ratio of E_{x0}^{+} and E_{y0}^{+}, and it equals unity when the conditions in (B.6) are met.

$$AR = \begin{cases} -\dfrac{OA}{OB} & \text{RHCP} \\ +\dfrac{OA}{OB} & \text{LHCP} \end{cases} \qquad 1\ (\text{CP}) \le |\text{AR}| \le \infty\ (\text{LP}) \tag{B.8}$$

for $$OA = \left[\frac{1}{2}\left\{\left(E_{x_0}^{+}\right)^2 + \left(E_{y_0}^{+}\right)^2 + \left[\left(E_{x_0}^{+}\right)^4 + \left(E_{y_0}^{+}\right)^4 + 2\left(E_{x_0}^{+}\right)^2\left(E_{y_0}^{+}\right)^2\cos(2\Delta\varphi)\right]^{\frac{1}{2}}\right\}\right]^{\frac{1}{2}} \tag{B.9}$$

and $$OB = \left[\frac{1}{2}\left\{\left(E_{x_0}^{+}\right)^2 + \left(E_{y_0}^{+}\right)^2 - \left[\left(E_{x_0}^{+}\right)^4 + \left(E_{y_0}^{+}\right)^4 + 2\left(E_{x_0}^{+}\right)^2\left(E_{y_0}^{+}\right)^2\cos(2\Delta\varphi)\right]^{\frac{1}{2}}\right\}\right]^{\frac{1}{2}} \tag{B.10}$$

In order to generate circular polarization with a single feed in microstrip antennas, two equal amplitude orthogonal degenerate modes (the same cut-off frequency) must be excited on a (nearly) square microstrip antenna. For probe-fed antennas, placement of the feed (Figure B.2) at the appropriate location (x',y') will excite these two modes, each with slightly different resonant frequency. One mode will have resonant a frequency that is higher by the same amount that the frequency of the other mode is lower. The electric field in the antenna cavity for these two dominant modes (TM01 and TM10) of the microstrip antenna can be expressed as (B.11) from [47]. Feeding the antenna at either position 1 or position 3 in Figure B.2 (a) produces only one mode. However, resulting

field if the antenna in Figure B.2 (a) is fed along the diagonal, or with feed locations shown in Figure B.2 (b), is either the sum (feed location 2) or difference (feed location 4) of the two modes. Circular polarization can also be achieved by capacitively loading the patch in Figure B.2 (c).

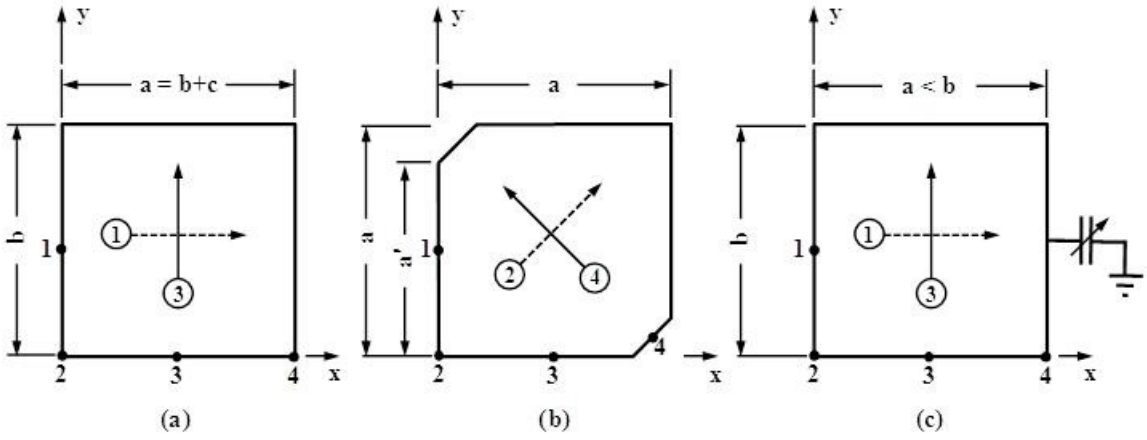

Figure B.2 Feed locations for circularly polarized nearly square microstrip patch antennas [41] © [1979] IEEE.

The fields of the nearly square microstrip antenna with dimensions a and b (a-b«a) in Figure B.2 near resonant frequency with wavenumber k' (k10<k'<k01) are proportional to 1/(k-k10) or 1/(k-k01) and thus can be written as in (B.11) [47].

$$E_x \propto \frac{\cos(\pi x'/a)}{k - k_{10}}; \quad E_y \propto \frac{\cos(\pi y'/b)}{k - k_{01}} \tag{B.11}$$

for

$$k_{10} = \frac{\pi}{b}; \quad k_{01} = \frac{\pi}{a}; \quad k = k_0 \varepsilon_r \left(1 - \frac{j}{2Q}\right) = k' - jk'' \tag{B.12}$$

where k in (B.12) is found in [41] k_0 is the wavenumber for free space, and k_{01} and k_{10} are wavenumbers for TM_{01} and TM_{10} mode respectively and can be considered to have the same effective loss tangent (δ_{eff}=1/Q) [41].

Appendix B (continued)

In addition to exciting both equal amplitude orthogonal modes, the condition for quadrature phase difference between the modes (B.13) [41,47] (+j denotes LHCP, -j denotes RHCP) is satisfied by finding the feed location (x',y') such that the phasors (k-k_{10}) and (k-k_{01}) are orthogonal. From Figure B.3, k' is found at the point where the value on the circle whose diameter is given as (k_{01}-k_{10}) is the same as the point on the line with k"/k'=1/2Q slope.

$$\frac{E_y}{E_x} \approx A\frac{k^2 - {k_{10}}^2}{k^2 - {k_{01}}^2} \approx A\frac{k - k_{10}}{k - k_{01}} = \pm j \qquad \text{where} \quad A = \frac{\cos(\pi y'/b)}{\cos(\pi x'/a)} \tag{B.13}$$

Utilizing similarities in two right triangles of Figure B.3, (B.14) [47] and (B.15) [47] can be deduced to find two possibilities for the resonant frequency (k') as given in (B.16) [47].

$$\frac{k' - k_{10}}{|k - k_{10}|} = \frac{|k''|}{|k - k_{01}|} \tag{B.14}$$

$$\frac{k_{01} - k'}{|k - k_{01}|} = \frac{|k''|}{|k - k_{10}|} \tag{B.15}$$

$$k' = \begin{cases} \dfrac{k_{10}}{1 + \dfrac{1}{2QA}} \\ \dfrac{k_{01}}{1 + \dfrac{A}{2Q}} \end{cases} \tag{B.16}$$

When the antenna is fed at either feed location 2 or 4 in Figure B.2, the solution in (B.17) [47] is obtained by substituting 1 for *A*, defined in (B.13). Figure B.4 illustrates the narrow nature of CPBW resulting from single feed induced circular polarization in microstrip antennas.

$$A^2 + \frac{2Qc}{b} + 1 + \frac{c}{b} = 0 \tag{B.17}$$

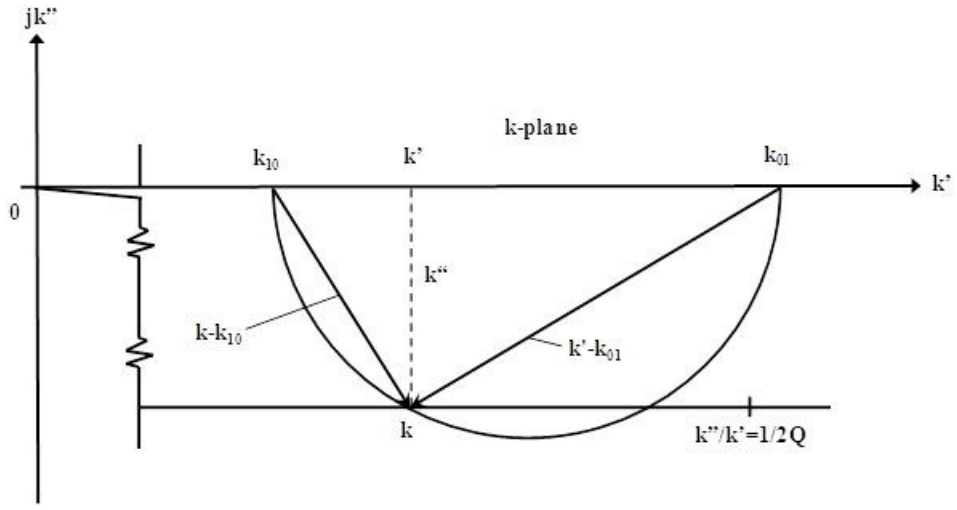

Figure B.3 Illustration of k', k_{10} and k_{01} [47] © [1988] IEEE.

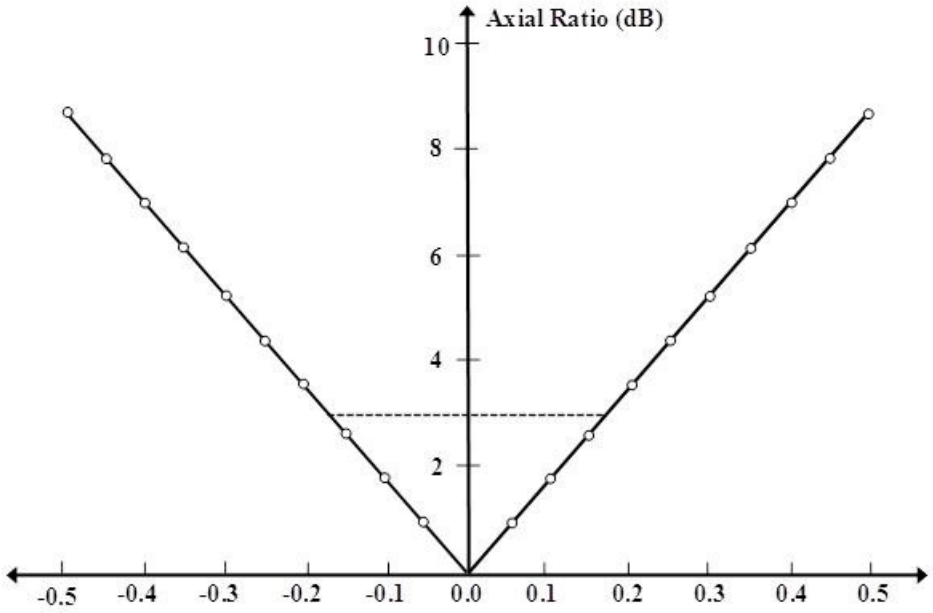

Figure B.4 Axial ratio vs. normalized frequency [44] © [1979] IEEE.

Appendix C: Pattern Parameters for Uniform Amplitude Broadside Arrays

Referring to the definition of the array factor given by (2.15), the major pattern parameters for uniform amplitude broadside arrays used in this work and the conditions under which they occur are given in Table C.1 [24]. The most important pattern parameters are those illustrated in Figure C.1.

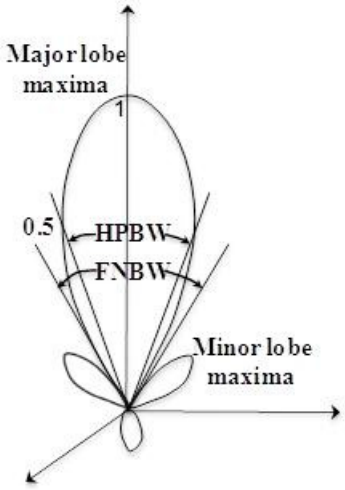

Figure C.1 Illustration of major and minor lobe, HPBW and FNBW.

Appendix C (continued)

Table C.1 Major pattern parameters for uniform linear broadside array.

	CONDITION	ANGLE (Uniform Linear Arrays)	ANGLE (Broadside Linear Arrays)
NULL	$\frac{\psi}{2}=\frac{1}{2}(kd\cos\theta+\beta)\Big\vert_{\theta=\theta_m}=\pm n\pi$	$\frac{\psi}{2}=\frac{1}{2}(kd\cos\theta+\beta)\Big\vert_{\theta=\theta_m}=\pm m\pi$	$\theta_n=\cos^{-1}\left(\pm\frac{n}{N}\frac{\lambda}{d}\right)$ when $n=1,2,3\ldots\neq N,2N,3N\ldots$
FNBW			$\Theta_n=\left[\frac{\pi}{2}-\cos^{-1}\left(\frac{\lambda}{Nd}\right)\right]$
MAXIMA	$\frac{\psi}{2}=\frac{1}{2}(kd\cos\theta+\beta)\Big\vert_{\theta=\theta_m}=\pm m\pi$	$\theta_m=\cos^{-1}\left[\frac{\lambda}{2\pi d}(-\beta\pm 2m\pi)\right]$ for $m=1,2,3\ldots$	$\theta_m=\cos^{-1}\left(\pm\frac{m\lambda}{d}\right)$ for $m=1,2,3\ldots$
3 dB point	$\frac{N}{2}\psi=\frac{N}{2}(kd\cos\theta+\beta)\Big\vert_{\theta=\theta_h}=\pm 1.391$	$\theta_h=\cos^{-1}\left[\frac{\lambda}{2\pi d}\left(-\beta\pm\frac{2.782}{N}\right)\right]$	$\theta_h=\cos^{-1}\left(\pm\frac{1.391\lambda}{\pi Nd}\right)$ for $\pi d/\lambda<<1$
HPBW			$\Theta_h=2\left[\frac{\pi}{2}-\cos^{-1}\left(\frac{1.391\lambda}{\pi Nd}\right)\right]$ when $\pi d/\lambda<<1$
1ST MINOR LOBE BEAWIDTH	$\frac{N}{2}\psi=\frac{N}{2}(kd\cos\theta+\beta)\Big\vert_{\theta=\theta_s}=\pm\frac{3\pi}{2}$	$\theta_s=\cos^{-1}\left[\frac{\lambda}{2\pi d}\left(-\beta\pm\frac{3\pi}{N}\right)\right]$	$\theta_s=\cos^{-1}\left[\pm\frac{\lambda}{1d}\left(\frac{2s+1}{N}\right)\right]$ for $s=1,2,3\ldots;\ \pi d/\lambda<<1$
1ST MINOR LOBE MAXIMA			$\Theta_s=2\left[\frac{\pi}{2}-\cos^{-1}\left(\frac{3\lambda}{2dN}\right)\right]$ when $\pi d/\lambda<<1$
DIRECTIVITY			$D_0=2N\left(\frac{d}{\lambda}\right)=2\left(1+\frac{L}{d}\right)\left(\frac{d}{\lambda}\right)\approx 2\frac{L}{\lambda}$ when $Nd/\lambda\to\infty, L>>d$

Appendix D: Figure Reprint Permissions

Following are IEEE "thesis/dissertation reuse" guidelines that refer to permission to use Figure 1.1, Figure 1.2, Figure 1.3, Figure 2.5, Figure 2.6, Figure 2.7, Figure 2.8, Figure 2.11, Figure 2.12, Figure 2.14, Figure B.2, Figure B.3 and Figure B.4 in the body of this manuscript.

The IEEE does not require individuals working on a thesis to obtain a formal reuse license, however, you may print out this statement to be used as a permission grant:
Requirements to be followed when using any portion (e.g., figure, graph, table, or textual material) of an IEEE copyrighted paper in a thesis:

1) In the case of textual material (e.g., using short quotes or referring to the work within these papers) users must give full credit to the original source (author, paper, publication) followed by the IEEE copyright line © 2011 IEEE.
2) In the case of illustrations or tabular material, we require that the copyright line © [Year of original publication] IEEE appear prominently with each reprinted figure and/or table.
3) If a substantial portion of the original paper is to be used, and if you are not the senior author, also obtain the senior author's approval.

Requirements to be followed when using an entire IEEE copyrighted paper in a thesis:

1) The following IEEE copyright/ credit notice should be placed prominently in the references: © [year of original publication] IEEE. Reprinted, with permission, from [author names, paper title, IEEE publication title, and month/year of publication]
   2) Only the accepted version of an IEEE copyrighted paper can be used when posting the paper or your thesis on-line.
   3) In placing the thesis on the author's university website, please display the following message in a prominent place on the website: In reference to IEEE copyrighted material which is used with permission in this thesis, the IEEE does not endorse any of [university/educational entity's name goes here]'s products or services. Internal or personal use of this material is permitted. If interested in reprinting/republishing IEEE copyrighted material for advertising or promotional purposes or for creating new collective works for resale or redistribution, please go to http://www.ieee.org/publications_standards/publications/rights/rights_link.html to learn how to obtain a License from RightsLink.

Appendix D (continued)

Following is the permission from John Wiley & Sons, Inc. to reprint Figure 2.9 and Figure 1.10.

JOHN WILEY AND SONS LICENSE TERMS AND CONDITIONS

Nov 20, 2012

This is a License Agreement between Bojana Zivanovic ("You") and John Wiley and Sons ("John Wiley and Sons") provided by Copyright Clearance Center ("CCC"). The license consists of your order details, the terms and conditions provided by John Wiley and Sons, and the payment terms and conditions.

All payments must be made in full to CCC. For payment instructions, please see information listed at the bottom of this form.

License Number	3033281288181
License date	Nov 20, 2012
Licensed content publisher	John Wiley and Sons
Licensed content publication	Wiley Books
Book title	Antenna Theory: Analysis and Design, 3rd Edition
Licensed content author	Constantine A. Balanis (Arizona State Univ.)
Licensed content date	Apr 1, 2005
Type of use	Dissertation/Thesis
Requestor type	University/Academic
Format	Electronic
Portion	Figure/table
Number of figures/tables	2
Number of extracts	
Original Wiley figure/table number(s)	chapter 6, figures 5 and 16 (Figure 6.5 and Figure 6.15)
Will you be translating?	No
Order reference number	
Total	0.00 USD
Terms and Conditions	

TERMS AND CONDITIONS

This copyrighted material is owned by or exclusively licensed to John Wiley & Sons, Inc. or one of its group companies (each a "Wiley Company") or a society for whom a Wiley Company has exclusive publishing rights in relation to a particular journal (collectively WILEY"). By clicking "accept" in connection with completing this licensing transaction, you agree that the following terms and conditions apply to this transaction (along with the billing and payment terms and conditions established by the Copyright Clearance Center Inc., ("CCC's Billing and Payment terms

Appendix D (continued)

Following is the permission from Artech House Publishers, Inc. to use Figure A.1 in this dissertation.

From: **Walsh, Mark** <MWalsh@artechhouse.com>
Date: Wed, Nov 28, 2012 at 2:56 PM
Subject: RE: requesting permission to use a figure from the book with ISBN# 0-89006-513-6
To: "Bojana [Boyana] Zivanovic" <bovana.zivanovic@gmail.com>

Dear Bojana,

Thank you for your inquiry regarding permission to reproduce copyrighted material in your dissertation. You may consider this notification the formal assent of Artech House to use the figure for the purpose cited.

Good luck with your dissertation!

Best regards,

Mark Walsh
Senior Editor
Artech House Publishers, Inc.

From: Bojana [Boyana] Zivanovic [mailto:bovana.zivanovic@gmail.com]
Sent: Wednesday, November 28, 2012 2:53 PM
To: Walsh, Mark
Subject: Fwd: requesting permission to use a figure from the book with ISBN# 0-89006-513-6

Mr. Walsh,

below is the email I sent requesting the permission. Thank you so much for your help regarding this matter.

Best regards,
Bojana

---------- Forwarded message ----------
From: **Bojana [Boyana] Zivanovic** <bovana.zivanovic@gmail.com>
Date: Wed, Nov 21, 2012 at 2:25 PM
Subject: requesting permission to use a figure from the book with ISBN# 0-89006-513-6
To: sronan@artechhouse.com

Ms. Ronan,

I am writing to you to request permission to use a figure in Appendix A of my dissertation from the book with ISBN# 0-89006-513-6 , "Microstrip Antenna Design Handbook" by Ramesh Garg, Prakash Bhartia, Inder Bahl and Apisak Ittipiboon. The title of my dissertation is "Series-Fed Aperture-Coupled Microstrip Antennas and Arrays", Electrical Engineering Dept., University of South Florida. The figure I would like to receive a permission to use is Figure 1.16 (b) Rectangular magnetic current sheet on page 34. I would appreciate if you could let me know what I need to do to obtain this permission.

Best regards,
Bojana Zivanovic

Appendix D (continued)

Following is the permission from John Wiley & Sons, Inc. to use Figure B.1 in this dissertation.

Campbell, Brenton - Hoboken

From: Goldweber, Paulette - Hoboken on behalf of Permissions - US
Sent: Monday, November 26, 2012 10:07 AM
To: Campbell, Brenton - Hoboken
Subject: FW: requesting permission to use two figures from the book with ISBN# 0-471-62194-3

Categories: Permissions

Hi Brent – over to you.

Thanks!

From: Bojana [Boyana] Zivanovic [mailto:boyana.zivanovic@gmail.com]
Sent: Wednesday, November 21, 2012 2:38 PM
To: Permissions - US
Subject: requesting permission to use two figures from the book with ISBN# 0-471-62194-3

To Whom It May Concern:

I am writing to you to request permission to use information from two figures from the book with ISBN# 0-471-62194-3, "Advanced Engineering Electromagnetics" by Constantine A. Balanis in a figure in Appendix B of my dissertation. The title of my dissertation is "Series-Fed Aperture-Coupled Microstrip Antennas and Arrays", Electrical Engineering Dept., University of South Florida. The figures I would like to receive a permission to use are Figure 4.17 Right- and left-hand elliptical polarizations with major axis along the x axis. (a) Right-hand (clockwise) when ER>EL. (b) Left-hand (counterclockwise) when ER<EL. on page 165 and Figure 4.19 Rotation of a plane electromagnetic wave and its tilted ellipse at z=0 as a function of time on page 167. I would appreciate if you could let me know what I need to do to obtain this permission.

Best regards,
Bojana Zivanovic

PERMISSION GRANTED
BY: [redacted]
Global Rights Dept., John Wiley & Sons, Inc.

NOTE: No rights are granted to use content that appears in the work with credit to another source

ABOUT THE AUTHOR

Bojana Zivanovic received the B.S. degree in Physics in 2003 from St. John Fisher College in Rochester, NY and received the M.S. degree in Electrical Engineering with concentration in Microelectronics in 2005 from the University of South Florida. During her Master studies, she conducted research in nanotechnology and material science. Her research interests focus on electromagnetic analysis, design and network model development of planar antenna arrays, and phased array technology. She is a member of IEEE Antennas and Propagation Society, Society of Women Engineers and IEEE Microwave Theory and Techniques Society. Bojana was born in Belgrade, Serbia.